PHYSIK DEPARTMENT

Protein-based nanoparticles with thermoswitchable particle size

Dissertation von

Bettina Kracke

TECHNISCHE UNIVERSITÄT MÜNCHEN

TECHNISCHE UNIVERSITÄT MÜNCHEN

Physik Department
Lehrstuhl für Biophysik E22
und
Zentralinstitut für Medizintechnik

Protein-based nanoparticles with thermoswitchable particle size

Bettina Kracke

Vollständiger Abdruck der von der Fakultät für Physik der Technischen Universität München zur Erlangung des akademischen Grades eines

Doktors der Naturwissenschaften (Dr. rer. nat.)

genehmigten Dissertation.

Vorsitzender: Prof. Dr. Ulrich Gerland

Prüfer der Dissertation:

1. Prof. Dr. Thorsten Hugel
2. Prof. Dr. Christine Papadakis

Die Dissertation wurde am 13.09.2016 bei der Technischen Universität München eingereicht und durch die Fakultät für Physik am 12.10.2016 angenommen.

Contents

Abstract

The development of new nanomaterial has become a rapidly growing research field. Material that can be switched by a change in environmental conditions is particularly interesting, since it can give control over a system's characteristics and add functionality to it. Stimuli-responsive polymers are such a promising polymer group.

Presented here is an approach towards the design of a nanoparticle system that is based on stimuli-responsive polymers. The nanoparticle's building blocks are fusion proteins, composed of a homotrimeric headgroup and three chains of elastin-like polypeptides (ELPs). The latter belong to the group of stimuli-responsive polymers that show an inverse temperature transition. As was shown before, the fusion proteins reversibly form particles upon an increase in temperature, due to their amphiphilic constitution above their specific transition temperature T_t.

It was the aim of this work to prevent the particle disassembly below T_t via the establishment of covalent cross-links. Most specifically, the method of cross-link was designed to enable a particle swelling upon the inverse temperature transition. Poly(ethylene glycol (PEG)-linkers of defined size, carrying maleinimide functionalities at either end, were applied for a reaction with the cysteine side groups in the ELP chain. Each monomer peptide chain contained one cysteine in order to provide a specific cross-link location.

The establishment of covalent stabilization in the interior of the particles rendered the system stable both above and below T_t and enabled a temperature-triggered swelling and collapsing of the particle. The particle size distribution was characterized via dynamic light scattering, fluorescence correlation spectroscopy, atomic force microscopy and transmission electron microscopy. The change in diameter was defined to around 30 % from mean values of the particle distribution from dynamic light scattering measurements. This corresponded to a volume change of around 64 %. The work concludes with a theoretical view on potential loading capacities and first loading tests. Fluorescently labeled dextrans were loaded into nanoparticles carrying themselves a fluorescence label. First colocalization studies via confocal fluorescence microscopy proved the loading capability of these particles.

The newly developed nanoparticles may find application in the biomedical field: Such a carrier system loaded with molecules, may release these in a controlled manner upon a temperature stimulus.

Zusammenfassung

Die Entwicklung neuer Nanomaterialien hat sich zu einem stark wachsenden Forschungsfeld entwickelt. Materialien, die durch eine Änderung von Umgebungs-Parametern geschaltet werden können, sind besonders interessant, da diese eine Kontrolle über die Systemeigenschaften ermöglichen können und einem System Funktionalität zuweisen können. Stimulus-responsive Polymere sind eine solche vielversprechende Polymergruppe.

In dieser Arbeit wird die Entwicklung eines schaltbaren Nanopartikelsystems vorgestellt, welches auf Stimulus-responsiven Polymeren basiert. Die Baueinheiten der Nanopartikel sind Fusionsproteine, die aus einer homotrimeren Kopfgruppe und drei Ketten Elastin-artiger Polypeptide (ELPs) bestehen. Letztere gehören zur Gruppe stimulus-responsiver Polymere, welche einen inversen Temperaturübergang aufweisen. Wie bereits gezeigt wurde, können sich die Fusionsproteine durch eine Temperaturerhöhung reversibel zu Partikeln zusammenlagern, was durch deren amphiphile Konstitution oberhalb ihrer spezifischen Sprungtemperatur T_t ermöglicht wird.

Diese Arbeit hatte zum Ziel, durch kovalente Cross-links das Zerfallen der Partikel unterhalb T_t zu verhindern. Der Cross-link sollte ein Quellen der Partikel als Reaktion auf den inversen Temperaturübergang ermöglichen. Es wurden PEG-Linker mit bis-Maleinimid-Funktionalität verwendet, um die Polymere über Cystein-Seitengruppen innerhalb der ELP-Kette kovalent zu verbinden. Jede Peptidkette wies ein Cystein auf, um die Ortsspezifität des Cross-links zu gewährleisten.

Durch den Cross-link erhielten die Partikel Stabilität sowohl oberhalb als auch unterhalb T_t. Dies ermöglichte ein Temperatur-gesteuertes Quellen und Kollabieren der Partikel. Die Größenverteilung der Nanopartikel wurde mittels Dynamischer Lichtstreuung, Fluoreszenzkorrelations-spektroskopie, Rasterkraftmikroskopie und Transmissionselektronenmikroskopie charakterisiert. Messungen mittels dynamischer Lichtstreuung ergaben eine Durchmesseränderung von etwa 30 %, bezogen auf die Mittelwerte der Partikelverteilung. Dies entsprach einer Volumenänderung von etwa 64 %. Die Arbeit schließt mit einer theoretischen Betrachtung der potenziellen Ladekapazität und erster experimenteller Nachweise zur Beladung der Partikel. Die Partikel wurden mit einem Fluoreszenzlabel markiert und mit Fluoreszenz-markierten Dextranen beladen. Erste Kolokalisierungs-Experimente mittels konfokaler Fluoreszenzmikroskopie belegten die Möglichkeit zur Beladung der Partikel.

Die neu entwickelten Nanopartikel könnten Anwendung in der Biomedizin finden: Ein solches, mit Molekülen beladenes, Carrier-System könnte diese Moleküle durch einen Temperatur-Stimulus in kontrollierter Weise freisetzen.

1. Introduction

1.1. Nanoparticles

1.1.1. Nanoparticles in drug delivery

Macromolecular structures for drug delivery have become a focus area of biomedical research over the last decades. The motivation lies in the manifold advantages of polymeric drug carriers over the administration of free drugs, which were already specified in an early work [1]. Benefits include a lowered toxicity compared to the administration of free drugs and the capability of targeting the active components to a certain tissue or cell type [1]. Furthermore, the encapsulation of drug agents into nanoparticles may increase the possible drug concentration at the site of action [2, 3].

Current research on carrier development aims at the design of particles on the nanoscale with defined architecture and self-assembling properties. Naturally occurring macromolecular assemblies with self-assembling properties, such as found in viruses, are properties that can be beneficial when incorporated in macrostructures in general and drug carrier systems in particular. Diverse building blocks with different characteristics may be combined, leading to a macromolecular carrier with the desired properties. The area of nanoparticle research is vast, including micellar carriers [2] which can be protein-based [3] or of synthetic origin, the latter known as polymeric micelles [4, 5] or. Furthermore, there are lipid-based carriers [6], virus-inspired nanocapsules [7, 8] and viral capsid-containing particles [9, 10], belonging to the class of protein cages [3]. But not only the range of material is versatile. Their potential applications can traverse various application fields where very prominent ones are for example drug delivery and diagnostics. For both applications, particles can be modified by coupling a specific detection system to the surface, thus exploiting the particle *surface* characteristics. In a different approach, the particle *interior* can be utilized as a compartmentalized reaction environment. It represents a shielded microenvironment which can be used for chemical reactions [11].

Nanoparticle design should combine the following important aspects in one particle system: A good loading capacity [3], the possibility for further modification [3], a long *in vivo* circulation time [12], a good release profile [3], biocompatibility and stability [2]. The optimization and combination of these aspects should result in a drug carrier system with maximized delivery efficiency [13]. One of the big challenges in drug carrier development is to achieve a high drug loading capacity of the polymeric carrier. This is especially challenging for hydrophobic drugs as loading molecules [2, 14, 15]. Furthermore, particle circulation times are influenced by particle characteristics such as particle size, shape and surface charge [13]. The stability of a macromolecular carrier system at physiological conditions dictates its applicability whereby it should remain stable before reaching its site of action. Naturally, the carrier should not provoke immunogenic effects when administered *in vivo* [16]. After drug release, the carrier should subsequently be degraded into non-toxic biodegradable products [2, 3].

Particle size is a critical parameter not only influencing transportation to the site of action and final clearance from the body, but also the efficiency of cellular uptake [13]. This was shown to be greatly increased for particles of diameters around 100 nm when compared to particles with

diameters between 1 and 100 µm [17]. Preferred sizes for drug carriers lie in the submicron range and current research focuses on nanoparticles with 10-100 nm diameter [18]. A reason for this lies in the enhanced uptake of these particles, which has been reported to be caused by ligand shortage effects. This terming describes the effect that particle uptake is limited by the availability of membrane-bound receptors of the target cell, which is dictated by receptor diffusion and redistribution after nanoparticle binding. The effect is more pronounced for larger particles and might end in localized ligand shortage and thus reduced nanoparticle internalization events [13]. Several studies reported on a superior uptake of particles with 50 nm diameter when compared to other sizes [19, 20 21]. It has to be considered that the optimum size is dependent on particle characteristics as well as the type of cell line [13] and type of tumor [22, 23]. Additionally, larger particles are more prone to be extruded via the lymphatic system while particles below 50 nm can distribute in extracellular spaces [3], whereas particles smaller than 10 nm diameter are more prone to renal clearance [18].
Higher molecular weight (MW) constructs, i.e. nanoparticles or polymer-conjugated drugs in general, feature the option of *passive drug targeting* to tumors due to the enhanced permeability and retention (EPR) effect [24]. The EPR effect is characterized by diffusion and accumulation of high MW constructs into the hyperpermeable vasculature with poor lymphatic drainage [24, 25]. Exploiting this effect can decrease the systemic toxicity of drugs [26]. Comparatively, a second possibility is the use of *active drug targeting* by the fusion of recognition functionalities to the administered drug such as peptide ligands or antibodies that can be recognized by specific receptors, reviewed elsewhere [2, 3]. In fact, the idea of coupling a drug to a targeting moiety is very old, originally proposed by Ehrlich at the beginning of the 20th century, which can be found reviewed in [27]. Nanoparticles covered with such functionalities can feature an increased receptor avidity due to their multivalency which can increase uptake [28].

1.1.2. Responsive carrier systems: Adding functionality to nanoparticles

A relatively new approach in particle design is to render the particle system responsive to environmental conditions [2]. This can be achieved by the incorporation of stimulus-responsive polymers, giving the nanoparticle switchable characteristics. Stimulus-responsive polymers can show chemical or physical responses when environmental conditions are changed. This can be a change in temperature [29, 30], in chemical conditions (such as pH or redox-environment) [31], irradiation with light or the application of a magnetic field [32]. Such involvement of molecular switches into nanocarriers leave large room for creative inventions. For a comprehensive overview over this research area it is referred to literature [33, 34, 35].

The cross-linking of a nanoparticle system with responsive characteristics does not only lead to an increased stability but might also give control over the release rate of the incorporated agents [36]. Particularly interesting is to render a nanoparticle system responsive to parameters of physiological relevance [37] such as the altered pH of tumor microenvironments [38]. A second specific aim is to achieve a controlled release of the drug, implying regulated doses of the active components. A system that responds to a certain trigger in form of swelling or collapsing might perform such a regulated release [33]. A challenge thereby is the tuning of the particle's interior to facilitate the extrusion of incorporated drugs, also those with high hydrophobicity.

As the presented work deals with the design of thermo-responsive nanocarriers, the focus is on temperature effects. Several approaches in designing thermoresponsive particles with synthetic polymers have been reviewed [34]. A prominent material for the design of thermo-switchable materials is poly(*N*-isopropylacrylamide) (PNIPAm). Polymeric carriers based on these building blocks have been studied in terms of switchable drug carrier systems and the temperature-triggered extrusion of hydrophobic molecules has been shown [39, 40, 41]. However, toxicity and biodegradability can impede their applicability in drug administration [42]. Comparatively, the employment of protein-based polymers as building blocks involves high biocompatibility. Elastin-like polypeptides (ELPs) present such a polymer group which can be designed to respond to external stimuli in a distinct manner, as will be outlined in chapter 1.2. ELPs represent the starting material for the thermally switchable nanoparticles developed in this work.

1.2. Elastin-like polypeptides (ELPs)

1.2.1. Elastin sequence: The basis for the ELP primary structure

Elastin represents one of the main structural components of the extracellular matrix [43, 44, 45]. It makes up a large fraction of the overall protein content in tissues such as lung, ligaments and vascular walls where the elastin content has been defined to approximately 30% in lung [46] and 50% in arteries [45]. To a smaller extent it is also present in skin tissue where it makes up 2-4 % of the dry weight [45]. Its function is to give elasticity to the tissue, facilitating the frequent cycles of stretching and contraction [45, 43, 44, 47]. The elastin structure depends on the tissue where it is integrated [48]. Interestingly, there exists an extraordinary high similarity in sequence composition throughout different species [49]. The elastin fiber is coated with a microfibrillar glycoprotein coating [50] and owns a significant durability with a reported half-life of approximately 40 years [51]. The precursor protein of fibrous elastin is tropoelastin which has a MW of approximately 72 kilo Daltons (kDa). Elastin is formed through covalent cross-links of tropoelastin where the lysine side chains serve as cross-linking points [52, 53, 54]. A characteristic is its primary sequence, which is composed of repeating elements of a tetrapeptide valine-proline-glycine-glycine (VPGG), a pentapeptide valine-proline-glycine-valine-glycine (VPGVG) and a hexapeptide alanine-proline-glycine-valine-glycine-valine-alanine (APGVGV) [55].

1.2.2. General characteristics of ELPs

As ELPs are based on the principal sequence motif of elastin, one characteristic of these polypeptides is their elasticity, which is very similar to that of elastin. The spontaneous elastic recoil of such a stretched molecule is driven by an entropic process [56]. ELPs are genetically engineered proteins that are derived from elastin as they are based on the pentapeptide repeat. The repeats will be termed GVGVP throughout this work if not noted otherwise. The sequence can also be written as $(G\alpha G\beta P)_n$ where the positions α and β depict substitutable positions that can be occupied by any amino acid of choice [57]. This makes the polymer a highly diverse construct that can be tuned to the desired properties by means of genetic engineering. However, it has to be considered that secondary and tertiary structures should be conserved throughout substitution, which is generally the case when the glycine and proline residues are not substituted [57]. Studies showed that the insertion of proline in position α is excluded [58] because of its important role in structure formation [59] and that a construct based on the repeat GVGAP did show different thermal properties [60].

The formation of the pentapeptide nomenclature will briefly be explained. ELP synthesis originally involved the permutations VPGVG and GVGVP. Early studies on ELP secondary structure were carried out with the VPGVG permutation, with a hydrogen bond between the valine[1] C-O and the valine[4] NH group. As it was later observed that the constructs based on the permutation GVGVP with proline at the carboxy-terminus led to larger yields of high MW constructs in peptide synthesis, it became the favored construct [61]. Later developments with recombinant DNA technology facilitated the production of GVGVP with appropriate restriction sites where long sequences based on the two repeats respectively are basically equivalent [62].

ELPs represent a particularly interesting building block for the design of stimuli-responsive systems. Practical advantages of ELPs imply the straightforward genetic engineering giving control over the exact sequence composition [63]. Synthesis of ELP-containing material can be controlled at a molecular or macromolecular scale. Exemplarily, the controlled synthesis of ELP-fibrils was reported [64] where the fibril diameter could be controlled by a variation of experimental conditions. Protein expression can be followed by a quick purification protocol, known as inverse transition cycling (ITC), that generally gives high protein yields [63, 65, 66]. This property has also led to the development of ELPs as a means for the purification of recombinant proteins [65, 67]. Most notably, ELPs have shown good biocompatibility in first *in vitro* and *in vivo* tests [68, 69, 70] and a good stability [57, 69].

One of their most important characteristics is their thermoresponsive behavior: Heating an ELP solution can lead to the formation of a protein-rich phase. This phase can form a dense coacervate upon settling [57]. It has served as cross-link material in early studies on elastomeric matrices [57]. Enzymatic degradation assays tested the biodegradability of ELP sequences in a diblock copolymer conformation. The studies proved decomposition of ELPs by elastase at low [71, 72] and high [72] temperature that means in their solvated and coacervated state respectively. This points at their promising applicability as biopharmaceuticals [72].

1.2.3. Applications of elastin and ELPs

Elastin-based materials exhibit a great potential for biomedicine including tissue-engineering and drug delivery which has been reviewed in [48, 71]. Besides their biocompatibility [68, 69, 70], elastin-based proteins show remarkable characteristics such as elasticity and self-assembling behavior [73]. The material was suggested to be applied in form of an extracellular matrix without cells or as purified elastin preparation [48]. As being based on elastin, which is a key structural protein of the native vasculature [45, 46] , the idea of its potential use in vascular applications seemed self-evident (reviewed in [74]). Potential application fields of ELPs include the design of vascular grafts [75, 76], non-thrombogenic coatings [77, 78] and soft-tissue repair [79, 80, 81].

Elastomeric matrices of ELPs had been produced by the application of γ-radiation to a highly concentrated solution of ELPs above a specific phase transition temperature. The matrices have been tested in various studies in terms of their biomedical applicability [68]. Cell culture experiments were carried out to test cell attachment to these matrices [82, 83, 84]. In some studies, matrices were modified with the cell adhesion sequence GRGDSP containing the peptide segment RGD, which had been discovered as key element for cell attachment [85, 86]. Cells were added to the modified matrices and found to adhere and proliferate [82, 83]. Conversely, matrices without the cell adhesion sequences have been analyzed in terms of postoperative adhesion prevention in clinical studies, where only a minor degree of adhesion was observed [84]. There have been similar reports in more recent studies [87, 88]. Other studies that analyzed injectable thermoresponsive drug depots based on ELPs, proved a sustained release from these gels where first-order release rates have been observed [89].

Concomitantly with the exploding research area on the development of new biomaterials around the turn of the millennium [90, 91, 92], ELP-research was extended to responsive material design. This included stimuli-responsive surfaces [93, 94] and molecular switches such as temperature-

dependent protein pores [95]. In the area of particle research, various groups focused on the development of ELP-based particle structures on the micro- and nanoscale where the object was to design a system with controllable self-assembly characteristics. The group of Chilkoti (Duke University) reported on various designs focusing on thermoresponsive particle formation which were tested for cancer treatment [96] and more specifically for their applicability in hyperthermia treatment [97, 98, 99] or their effects of multivalence [100, 101, 102]. Allover, their studies on drug-conjugated ELPs revealed decreased toxicity effects while showing improved efficacy, reviewed in [103]. The approach of temperature-induced ELP particle formation on the nano- and microscale was exploited by various other groups. Most studies employed a block polymer structure as principal building with sections of varying hydrophobicities [100, 104, 105, 106, 107, 108, 109] while other designs reported on ELP fusion proteins [37, 110]. A comprehensive analysis established a library of diverse ELP block polymers to predict the onset of nanoparticle formation [111]. In most cases particle formation was triggered by temperature and salt-induced assembly was recently reported [112]. ELP-based particles were shown to feature a good loading capacity and controlled drug release was shown for several ELP-based particles [113, 114, 115, 116]. These examples hint at the great potential of ELPs for applications in drug carrier design. However, all these constructs were created to show a reversible assembly and as such they were stable only above a distinct temperature or showed prolonged stability due to hysteresis behavior in the heating-cooling cycle. Thus, although these systems featured a possible control over assembly characteristics, their assembly was reversible.

Other studies employed cross-linking methods to achieve stability of ELP-based particles. Chemical cross-link with glutaraldehyde [117] yielded microspheres that showed a burst release of loaded molecules that was caused by an increase in temperature with induced pore formation of cross-linked ELP spheres. Physical cross-linking was carried out with γ-radiation, yielding particles with mean sizes in the 150-440 nm range [118] or resulting in particles with sizes around 50-100 nm and 50-200 nm, depending on the chosen construct [119 I]. However, the method of cross-linking via radiation may lead to backbone damages of the polymer and lacks chemoselectivity [120]. A different approach achieved the formation of stable nanoparticles by tuning their transition temperature for particle formation below body temperature [121, 122] and further stabilization via of disulfide-mediated cross-links [122].

In the course of ELP research, ELP fusion peptides were investigated where the fusion of an ELP sequence to a α-helical coiled coil motif brought the ELP chains in close proximity [123]. In a succeeding study, three ELP sequences were fused to a homotrimeric self-assembly domain derived from the bacteriophage T4 [37]. The current view on thermoresponsive behavior of ELPs states intermolecular association as essential for ELP aggregation [124] (compare section 2.1.3). The construct designed by Ghoorchian et al. [37] facilitated local proximity of three ELP chains, potentially supporting the temperature-induced aggregation of these polymers. The latter study demonstrated that the special design containing the "foldon" domain facilitated the assembly

[1] In the first example, the cross-link was achieved via a "droplet method" where ELP drops of several µl were transferred to hot deionized water to induce coacervation, followed by γ-irradiation. Particles with diameters > 100 nm were reported. Particles measured via DLS at high temperature and particles via TEM imaging after sample preparation at low temperature showed similar size distributions. The second study visualized radiation-induced cross-linked nanoparticles at room temperature.

into nanoparticles upon a distinct temperature stimulus [37]. As characteristic for ELPs, their responsiveness to salt and surfactant (further treated in part 2.1.4) was proven and particle sizes were tunable with changes in salt concentration.

1.3. Presentation of the developed nanoparticle system

1.3.1. Aim of the project

The aforementioned system from Ghoorchian et al. [37] presents the basic starting point of this work: Nanoparticles are formed via the reversible assembly of trimeric ELP-foldon fusion proteins, triggered by a defined temperature stimulus. It was the aim of the project to design a trimeric ELP construct that likewise assembles into nanoparticles and – in contrast to the preceding particle system – does not disassemble below a certain temperature. Instead, the particle system should show a temperature-induced size change, enabled via a covalent stabilization of the particle in its interior. The introduction of covalent cross-links, located in the outer third of the particle interior, hindered the disassembly of the particles below a certain temperature. In addition, the stabilization facilitated a temperature-triggered swelling of the particle upon the inverse temperature transition. The motivation for this design was the assumption that a temperature-induced size change could involve a triggered release of loaded agents. The size transition is illustrated in Figure 1.

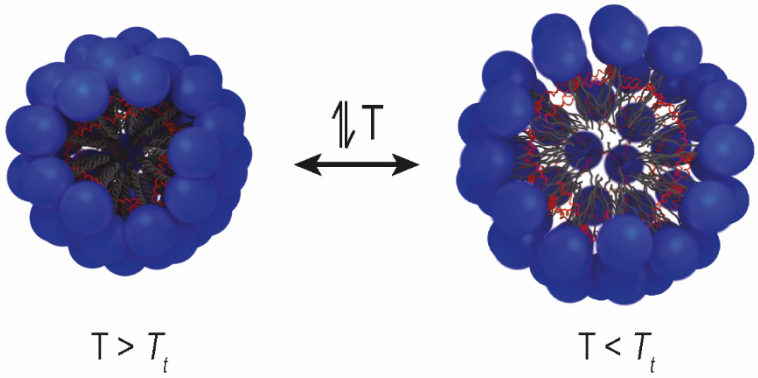

Figure 1: Illustration of the temperature-induced volume change of nanoparticles based on ELP fusion proteins developed in this work. Covalent linkages in the particle interior (in red) prohibit particle disassembly below a certain temperature (denoted as transition temperature T_t). This facilitates a temperature-induced particle swelling. The latter is a product of the thermo-responsive polypeptide unfolding below a specific temperature. Illustration is not to scale. Reprinted with permission from B. Kracke et al., 2015, Macromolecules 48, 5868-5877, Copyright © 2015 American Chemical Society [125].

The work at hand reports on the design, cross-link and characterization of responsive particles on the nanoscale which showed temperature-induced particle size changes. A well-known maleinimide cross-link method was applied, which was adapted to the special solution conditions needed for the stimuli-responsive polymers, responsive to their solution conditions. For the case presented, this implied a basic pH and low salt concentration. The use of a cysteine-directed cross-linking protocol enabled control over cross-linking site: One single cysteine was located in each ELP sequence (while being absent in the headgroup domain). The particle solution was characterized with view to its temperature-dependent size distribution and its loading capacity was estimated both theoretically and experimentally.

The nanoparticles presented combine different important aspects of nanoparticle design: They show a diameter below the critical cutoff value of 100 nm with a narrow size distribution. A site-directed chemical cross-link method enabled site-specific stabilization, which rendered the particles stable over a broad temperature range. As being based on ELPs, the particles showed a stimulus-responsiveness with a thermo-induced particle size change.

1.3.2. Composition of the nanoparticle building blocks

The nanoparticle of interest is formed via the temperature-triggered assembly of ELP fusion proteins that are composed of three hydrophobic chains and a hydrophilic headgroup [37]. Figure 2 depicts the principal composition of the fusion construct, with the ELP sequence as hydrophobic domain (in blue) in its folded conformation above a specific temperature. The presentation is for illustration purposes only and does not include the reported backbone dihedral angles for the β-spiral [126]. The sulfhydryl (-SH) groups highlighted are the points for cross-linking. The foldon headgroup as hydrophilic domain (in grey) is shown in the zoom image in backbone representation, based on data from solution NMR (PDB accession code 1RFO). The foldon is composed of three chains, presented here in brown, gold and grey. The location of the lysines at position 16 and the leucines at the carboxy-terminus are highlighted in green and red respectively. The hydrophobic and hydrophilic building block will be described in the following.

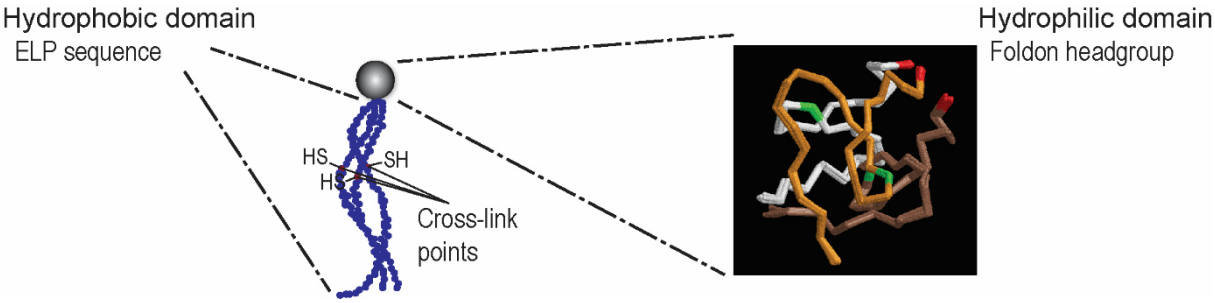

Figure 2: Illustration of the ELP fusion protein in the folded conformation above a specific temperature. Highlighted are the sulfhydryl (-SH) groups as functional groups for cross-linking. The presentation of the secondary structure is for illustration purposes only and not including the reported backbone dihedral angles for the β-spiral from Venkatachalam and Urry [126]. The enlargement shows the foldon domain, based on data from solution NMR, PDB accession code 1RFO [127]. The illustration was prepared with Rasmol and shows the protein backbone with the individual monomer chains a, b and c colored in brown, gold and grey respectively. The leucine at position 27 at the carboxy terminus is presented in red and the lysine at position 16 is colored in green. Illustration is not to scale.

The hydrophobic building block is based on an ELP sequence where one monomeric sequence includes a single cysteine residue. The cysteine is located in the X-position of one GXGVP repeat. Since there is no cysteine in the hydrophilic headgroup, these represent the only thiol functionalities of the construct. The ELP sequence is as follows:

$$MGH\text{-}(GVGVP)_{36}\text{-}(GCGVP)\text{-}(GVGVP)_{21}\text{-}GV$$

The trimeric construct consists of three ELP strands with 58 pentapeptides, which gives, with the residual coupling links, a total length of 295 amino acids for the monomeric ELP sequence and 885 amino acids in total for the ELP sequence in the trimer.

The foldon domain is a homotrimeric self-assembly domain, derived from the trimeric protein fibritin from the bacteriophage T4 [128]. In its natural occurrence, fibritin forms the collar structures ("whiskers") of the phage [129] which are involved in phage assembly [130] and its response to adverse environmental conditions [131]. Fibritin is connected to the phage tail directly adjacent to the head [132] and features a triple-stranded coiled coil conformation [128]. Fibritin trimerization was shown to occur at up to 2 % SDS at room temperature (RT) [133].

The foldon with 30 amino acid residues (residues 457-486 of fibritin) is located at the C-terminal end of fibritin. Its role corresponds to a foldon domain which has been defined as "controlling kinetic aspect of folding" [134]. The foldon in fibritin functions as a folding nucleus domain [133, 135] where it is responsible for the correct folding and spontaneous assembly [128, 133, 135, 136]. The self-assembly of the foldon has been shown to exhibit very fast folding kinetics [127]. The foldon domain has been employed as artificial trimerization domain in other constructs including collagen-like fibers [137, 138, 139], engineered protein fibers [140] and viral proteins [141, 142, 143, 144]. In all cases, stabilization of the construct was achieved when the foldon was fused to the C-terminal end of the construct. In a study where the foldon was fused as N-terminal domain, correct folding was hindered [140]. Recombinant collagen-like fusion proteins containing the foldon domain showed improved thermostability [137, 139].

The foldon diameter was reported to have a diameter of approximately 20 Å [140] while crystallography studies on fibritin revealed a distance of 25 Å between the trimers, which was rated an adequate outer diameter for a triple coiled coil [145]. The sequence composed of 27 amino acids has been used in fusion constructs where it has proven to promote trimerization [137]. The primary sequence is given below.

^{1}GYIPE-^{6}APRDG-^{11}QAYVR-^{16}KDGEW-^{21}VLLST-^{26}FL

The monomers feature a β-hairpin structure which is capped by a short hydrophobic part at the N-terminal and C-terminal end [146, 127]. The monomers trimerize via association of the β-hairpin structures [127] which leads to a β-propeller-like structure of the trimeric foldon [128]. The turn of the hairpin constitutes a charged region with the amino acids arginine, lysine, aspartic acid and glutamic acid [146]. The foldon is stabilized via strong inter-subunit salt bridges between Glu461 (E) and Arg471 (R) [128, 127] that break down at low pH [146]. The hydrophobic interior of the domain is essential for trimerization [128] and further stabilization is achieved through intermolecular backbone hydrogen bonds [128, 127]. The foldon has a net negative charge at neutral pH [37] and is stable up to 75 °C [137].

The Protparam tool (ExPASy, Bioinformatics Resource Portal) gives a theoretical isoelectric point (pI) of 4 of the foldon domain. The foldon group features several amino acids that contribute to its overall charge. The charged amino acids of a monomeric foldon sequence at pH 8 are listed in the following, including the respective typical pK_a [II] values [147] in parentheses.

Negative charges: 1x Carboxy-terminus (3.1), 2x D (4.1), 2x E (4.1)

Positive charges: 2x R (12.5), 1x K (10.8)

Thus, there are 15 negative and 9 positive charges in the foldon domain, resulting in a net negative charge at a pH 8 (which is the pH of the solution into which the nanoparticles were transferred after cross-link). In this work, the foldon domain is fused to the C-terminal end of the hydrophobic ELP chain and serves as hydrophilic headgroup. With its net negative charge, it facilitates the assembly into spherical aggregates instead of the formation of larger assemblies upon ELP coacervation.

[II] Values correspond to pK_a defined for the free amino acids and thus do not include environmental effects.

2. Theoretical Background

2.1. Thermoresponsiveness of ELPs

Thermoresponsive polymers can be either of synthetic origin, such as PNIPAm [148], or of biological origin such as ELPs [57]. These polymers show property changes in form of a phase transition when the solution is heated above a distinct temperature. They feature a lower critical solution temperature (LCST) behavior where the polymers are dissolved in solution below a certain temperature and heating above this temperature causes the polymers to phase-separate [149]. This process, termed phase transition, is characterized by a separation of the solution into two separate proportions of high and low protein concentration [57]. Depending on the original protein concentration, the extrusion of water from the protein solution can be visible during the transition [150]. When the solution is subsequently incubated above the characteristic temperature and the protein-dense phase is allowed to settle, a dense protein-rich coacervate forms. This is known as coacervation [150, 151]. The process represents a temperature-triggered aggregation process of polypeptide molecules in water, which is completely reversible [152]. The molecular basis for this observation will be given in the next paragraph, followed by a more detailed characterization of the thermoresponsive behavior of ELPs.

2.1.1. Hydrophobic hydration

Insights into hydrophobic interactions of molecules in aqueous environment are based on studies that involved the analysis of hydrophobic molecules in water. Experiments by Edsall showed a high molal heat capacity upon the dissolution of hydrophobic molecules in water [153] while Butler ascribed the low solubility of hydrophobic molecules in water to an entropic effect [154]. The connection of these observations to differences in water structure was proposed by Frank and Evans [155] where they described the rigid water structure around hydrophobic molecules as “icebergs”. The influence of hydrophobic hydration on protein folding and the formation of hydrophobic bonds in a protein was brought up in Kauzmann’s review in 1959 [156]. In studies on alkane gas hydrates, water of hydrophobic hydration was shown to feature a pentagonal arrangement [157, 158]. Such a pentagonal arrangement of water molecules was also observed in the crystal structure of a hydrophobic protein [159]. It was referred to as clathrate water [159, 157, 57, 160] where the strong interactions between the water molecules imply a rigid conformation of low entropy [150].

Hydrophobic parts tend to minimize their contact to water which is generally known as the hydrophobic effect. It is assumed to arise from the increased free energy of the water molecules when associating with themselves rather than from a favorable free energy of the hydrophobic parts [160]. When a system of adequate constitution experiences the supply of energy in the form of heat, the hydrophobic parts assemble [161], thereby minimizing the contacts between hydrophobic parts and water. The transition of a molecule in random configuration to a secondary structure is facilitated by a net increase in total entropy of the system [162]. The process of increasing order upon heating would seem to contradict the second law of thermodynamics which defines that the entropy of a closed system must increase with increasing

temperature [73, 163]. In accordance with this, the loss of entropy during hydrophobic assembly is compensated by the transition of the ordered clathrate water structure into bulk water of higher entropy [156, 155].

Protein stability is thought to be generally accomplished through hydrogen bonding and the hydrophobic effect [156, 164]. The latter includes the effect of hydration with its entropic contribution mentioned above and the Van der Waals (VdW) interactions of the solute molecules which is an enthalpic effect [165]. The hydrophobic effect was denoted as an important factor in protein folding or assembly processes yielding macromolecular structures, such as in micellization [166], which will be treated in 2.2.

2.1.2. The inverse temperature transition (ITT)

Already in the 1880s, first studies on biological elastic fibers were carried out by Roy [167] where the peculiar characteristic of tissue contraction upon the supply of heat was observed, which was stated as "exceptions to the general rule that heat causes expansion" [167, 168]. It was around 100 years later that the molecular basis for this behavior was explored and connected to the ITT [168]. Most of the theory about this mechanism concerning ELPs was established in the pioneering works of Urry and coworkers [57, 73].

ELPs belong to a group of molecules that feature a lower critical solution temperature (LCST): They are unstructured below a certain temperature and show a temperature-triggered phase transition, where they experience an increase in order when heat is applied [59]. The thermo-responsiveness of ELPs is based on the above mentioned tendency of hydrophobic molecules to minimize their contact to water through the process of hydrophobic association, thereby decreasing the extent of hydrophobic hydration [151]. The phase transition of ELPs was termed an ITT and has been defined by Urry et al. [169] as follows: "Inverse temperature transitions as exhibited by polypeptides and proteins are folding and aggregational transitions in which hydrophobic side chains of amino acids go from an aqueous milieu where each hydrophobic moiety is surrounded by waters of hydrophobic hydration to an environment where hydrophobic side chains are in direct contact with polypeptide." While one component (the polymer) undergoes a loss in entropy during the ITT, the driving force is the net positive change in entropy of the complete system [152, 73], facilitated by a change in entropy of the surrounding water molecules [150, 152]. Thus, if a protein features an appropriate composition, a raise in temperature can evoke the formation of order [170, 59].

In contrast to the exothermic reaction of dissolving hydrophobic molecules in water, the ITT with its destruction of hydrophobic hydration water represents an endothermic reaction where heat is needed to destabilize hydrophobic hydration [57, 150]. The transition is characterized by an increase in enthalpy and entropy [150] where the endothermic part is approximately three times larger than the exothermic part of the reaction [171]. The exothermic part was ascribed to the VdW cohesive interactions between the associating ELP chains [171]. The endothermic heat ΔH necessary to drive the transition was reported to be around 1-3 kcal/mol, defined for different pentamers [150]. Its value increases with hydrophobicity, which was explained by the quantity of water molecules of hydrophobic hydration that has to be destructured during the transition [150, 152, 172].

The phase transition of ELPs is a reversible process of self-assembly [57, 173, 168]. It is marked by two steps: First, the cloud point marks a sudden increase of scattered light which is caused by the formation of multiple scattering centers resulting from aggregation [62, 168]. When the solution is incubated at high temperature, a dense viscoelastic state forms, which is about 63 % water and 37 % protein [168, 174]. Upon prolonged storage above 80 °C, the coacervate has been shown to expel more water, leading to a final concentration of only 32 % water [174]. Comparatively, a cross-linked ELP matrix can consist of 90 % (w/v) water when swollen [175, 176, 177].

2.1.3. Structure formation upon the ITT

Works by Urry and coworkers shaped the current view of ELP secondary structure where it was defined as a β-spiral [126], substantiated by various analyses which will be briefly noted in the following. There is some controversy about the assumed structure: Works by the group of Daggett on molecular dynamics defined the β-spiral as an unstable structure [178, 179] while Gross and coworkers noted that the peptide might fold into a β-sheet [180]. Since the model by Urry is most widely accepted, the focus here will be on this view.

It was concluded that the ITT of ELPs is characterized by the optimization of hydrophobic contacts at high temperature [151]. By this, the individual pentameric repeats of the ELP sequence have been shown to adopt a specific dynamic conformation [168]. X-ray diffraction experiments were carried out on a special ELP construct, the cyclopentadecapeptide *cyclo*(VPGVG)$_3$ [181]. These studies revealed the formation of stacks above a certain temperature.

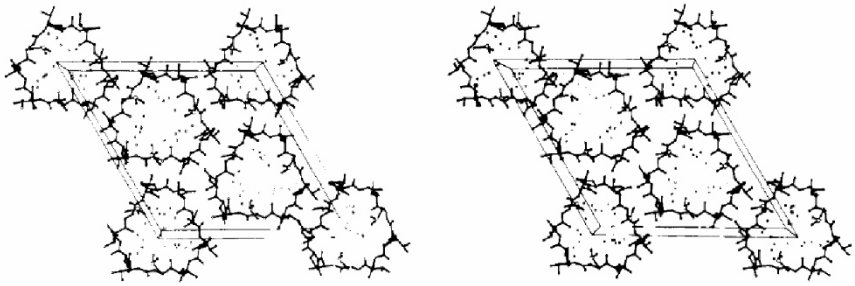

Figure 3: Stereoview of crystal packing of *cyclo*(VPGVG)$_3$, with incorporated water molecules. Reprinted with permission from Cook et al, 1980, J. Am. Chem. Soc. 102, 5502-5505, Copyright © 1980 American Chemical Society [181].

The stacks with an approximate spacing of 10 Å formed hydrophilic channels filled with water. Hydrophobic side chains were shown to protrude outwards and facilitate intermolecular interactions which is shown in Figure 3. NMR measurements [182, 183] and X-ray crystallography studies [181] lead to the proposed structure of a β-turn. The turn is formed between the proline and the glycine in the repeating sequence and was thus termed a Pro^2-Gly^3 β-turn [184, 126]. Cyclic forms were compared to linear constructs [185] and a model of a β-spiral was established [126]. Structure formation of ELPs upon heat was analyzed by various NMR measurements [151, 183, 186, 187] where the formation of a specific helical structure was observed. The helical structure had been termed a β-spiral [III] structure [188] wherein the repeating elements were following a β-turn motif [189]. They were shown to facilitate interactions between the individual segments [168].

[III] The terming spiral instead of helix resulted from the uncertainty about the presence of hydrogen bonding between the polypentapeptide repeats at that research stage.

Stabilization of the β-turn was shown to be established via side chain interactions between the Val^1 and Pro^2 [151, 190] and by hydrogen bonds between the Val^1-CO and the Val^4-NH [190]. Figure 4 a) shows the spiral wherein the turns function as spacers between the helical segments [126]. It was proposed that the β-spiral was a helical structure with inter-turn hydrophobic contacts [191]. The proposed most-ordered-state spiral structure from NMR studies has 2.8 Å pentamers per turn with a 3.2 Å translation per repeat along the axis [187].

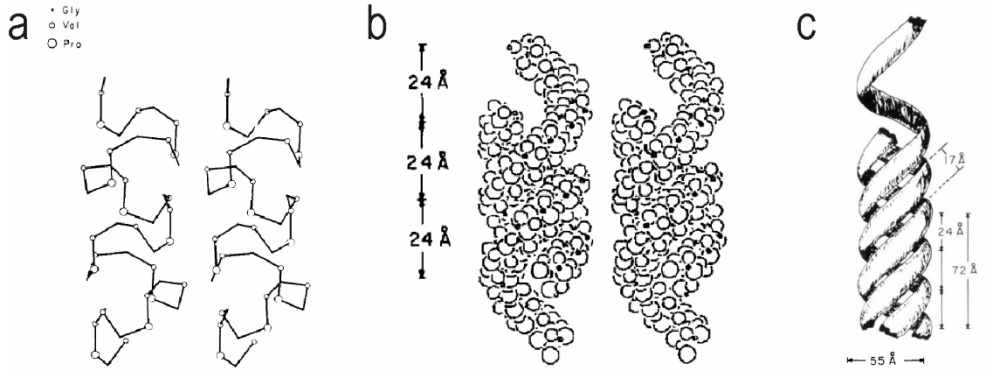

Figure 4: Secondary structure determined for ELP constructs. **(a)** Right-handed helix of an ELP chain. Reprinted with permission from Venkatachalam and Urry, 1981, Macromolecules 14, 1225-1229, Copyright © 1981 American Chemical Society [126]. **(b + c)** Illustrations of a fragment of a twisted filament, resulting from the association of β-spirals. Reprinted with permission from Urry, 1983, Ultrastructural Pathology 4, 227-251, Copyright © 1983 Taylor & Francis [192].

Apart from the large fraction of water in the bulk solution, there is also water associated with the ELP secondary structure, similar to the water associated in the cyclic constructs. It is present in the β-spiral and associated with the VGV repeats in the β-turn segment [73, 168]. The intraspiral and extraspiral water can exchange [126]. The secondary structure formation during the ITT was shown to be followed by the association of the helices into threefold twisted filaments [184, 192]. A fragment of a twisted filament is shown in Figure 4 b) and c). Already early studies suggested the formation of such structures due to the presence of hydrophobic side groups pointing out of the spiral structure [126]. The model of fibril formation involves initial polymer overlap [193] and association into three β-spirals into filaments [62]. ELP filaments visualized by TEM [194] were shown to be similar to those found in natural fibrous elastin [195, 196, 197] with the diameter of an ELP β-spiral being similar to elastin filaments [196, 197].

The current view on the ELP association upon the phase transition is shown in Figure 5, as was proposed by Yamaoka and coworkers [124]. The aggregation mechanism therein is thought to be facilitated by the local proximity of individual ELP chains. Structural changes upon heating are thought to facilitate the intermolecular association via hydrophobic groups, pointing outwards of a spiral. The two processes of structure formation and association are assumed to be interactive processes, where a first association further promotes structure formation [124].

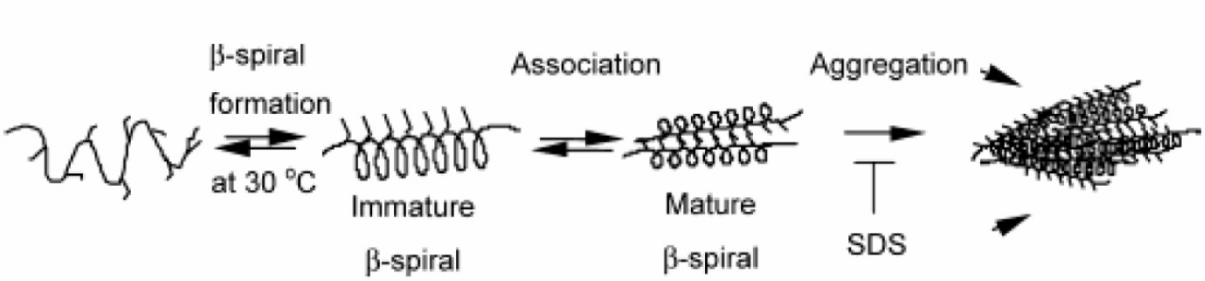

Figure 5: Assembly of β-spirals. Proposed mechanism for the ELP phase transition. The addition of detergents such as sodium dodecyl sulfate (SDS) at a specific concentration can prohibit the aggregation. Reprinted with permission from Yamaoka et al., 2003, Biomacromolecules 4, 1680-1685, Copyright © 2003 American Chemical Society [124].

This proposed mechanism is similar to elastogenesis, where hydrophobic interactions between strands were stated to be involved in the initiation of elastogenesis [198, 199]. Succeeding works proved this requirement also for ELPs, where the intermolecular contacts were shown to form between Val^4 in $P^1V^2G^3V^4G^5$ [187]. The influence of the valine positions on coacervation was explored, which proved structure formation also for repeating sequences of different length, involving repeats of $(VPG)_n$ and $(PGVG)_n$. However, no turbidity formation was observed, which hinted at a considerable impact of a defined valine spacing for self-association [190].

2.1.4. The transition temperature T_t

In first studies on the ITT behavior of ELPs, solutions were heated and turbidity formation was observed whereby a dependence on amino acid hydrophobicity was stated [150, 152, 169]. Turbidity profiles showed the degree of turbidity measured at 300 nm plotted as a function of temperature [169]. The half-maximum of turbidity was defined as the transition temperature T_t [169]. The thermodynamic properties of the phase transition can be described by the introduction of the change in Gibbs free energy (also referred to as free enthalpy) ΔG [57]. The description of ΔG in connection with the enthalpic term ΔH, the entropic term ΔS and the temperature T can be found in common scientific textbooks [147]:

$$\Delta G = \Delta H - T\Delta S \tag{2.1}$$

At the equilibrium phase transition, the chemical potential is the same for the dissociated molecules in solution and the associated molecules [200]. Therefore, the difference in Gibbs free energy ΔG at the phase transition is zero, which gives the definition of T_t at which the phase transition occurs [200]:

$$T_t = \frac{\Delta H_t}{\Delta S_t} \tag{2.2}$$

The subscript t denotes that the terms for temperature, enthalpic and entropic contributions are regarded at the phase transition [57]. A marked shift of the transition to lower temperatures was observed with an increase in hydrophobicity and in concentration [49 IV].

[IV] In that study, the constructs were produced via chemical peptide synthesis leading to ELP sequences with an n > 100.

Urry and coworkers analyzed the dependence of the T_t on the hydrophobicity of amino acids in a systematic study [169] where the constructs followed the principle sequence motif poly(f_v(VPGVG)f_x(VPGXG)) with f_v and f_x as the mole fractions of the respective pentapeptide with $f_v + f_x = 1$. Turbidity profiles were taken for different constructs of poly(0.8(VPGVG)0.2(VPGXG)). The T_t was observed to be shifted to lower temperatures when the hydrophobicity of the substituted amino acid was increased. The data set was expanded by turbidity measurements with different mole fractions of the pentapeptide with X being substituted by various amino acids. The results obtained by that study are shown in Figure 6. The T_t was defined for the mole fraction $f_x = 1$ by extrapolation of the fitted line [169]. Noteworthy is the large increase in T_t with the introduction of charges as with aspartic acid or glutamic acid, labeled Asp(COO^-) and Glu(COO^-) respectively in the graph. This can be explained by the disruptive effect of charged species on the pentagonal arrangement of hydrophobic hydration and the formation of their own hydration water arrangement [175, 176]. The introduction of charges decreases the entropic contribution during the transition. To obtain a dominating value of the entropic term, the temperature has to be increased and the Gibbs energy is the driving force for the ITT [175, 176].

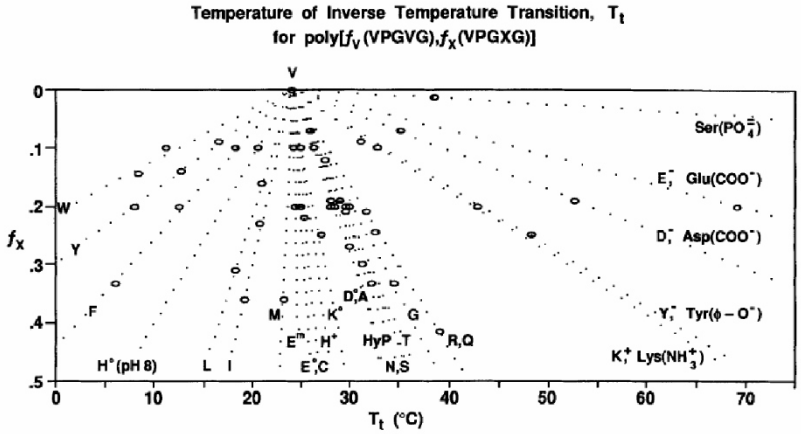

Figure 6: Definition of the transition temperature T_t for different ELP sequences of poly(f_v(VPGVG)f_x(VPGXG)) with X as substitutable amino acid position. The polymers were characterized in terms of their turbidity profiles at 300nm upon heating. The graph illustrates the dependence of T_t on the mole fraction f_x with different amino acids in the guest residue X. Reprinted with permission from Urry et al, 1992, Biopolymers 32, 1243-1250, Copyright © 1992 John Wiley and Sons [169].

In a new approach of Meyer and Chilkoti [201], a formula for the T_t prediction of ELP constructs at varying concentration and composition was introduced. They remarked that former works [169] employed ELP constructs with relatively large MW > 50 kDa and high protein concentration (>40 mg/mL) and that precise control over chain length was not guaranteed at that time [201]. In a different study by the group of Rodríguez-Cabello [58], the T_t was stated not only to be dependent on the mean polarity but also on the exact sequence composition. In this study, different ELP constructs containing varying fractions of alanine- and glutamic acid-containing pentamers with different arrangements of the building blocks were used. The T_t versus the molar fraction of the alanine-containing pentamer showed no linear behavior. It was concluded that a prediction of T_t is only feasible for homopolymers of a regular sequence and is not applicable for ELP block copolymers with a subdivision in large sections with different hydrophobicities.

The T_t can be influenced by salt concentration [175, 176, 202, 203] and various studies were carried out to decipher its molecular basis. Primary fundamental studies on the temperature decreasing

effect of NaCl on T_t was explained by its influence on peptide hydration instead of a direct binding to the peptide sequence [202, 203]. The destabilizing effect of charges on the pentagonal water arrangement would result in less energy required for triggering the assembly process, lowering T_t [175, 176]. A later study proposed that salt might provoke a higher difference in polarity between the solvent and the dissolved molecules, which would cause a more ordered structure around hydrophobic molecules [204]. Furthermore, salt effects in general have been categorized by the Hofmeister series, summarized in [205]. It was differentiated between salting-in and salting-out ions which favor the formation of coil-like structures or the formation of collapsed states respectively [206]. The influence of salt on the temperature behavior of ELPs has been analyzed in terms of the Hofmeister series by the groups of Chilkoti and Cremer [207]. It was differentiated between kosmotropic salting-out ions, which were reported to polarize and thus destabilize associated water structures, while chaotropic salting-in ions were reported to directly bind to the amide groups in the ELP backbone.

As the dependence of T_t on the introduction of charges in the peptide sequence was illustrated, the T_t can also be altered by chemical modifications such as phosphorylation [208]. Aside from the effect of protein composition in terms of hydrophobicity [169], it has been proposed that different amino acids might also influence the transition behavior by their differences in conformational preferences [209]. Additionally, it was shown that the T_t depends on molecular architecture [37, 210] . Besides this, multiple other factors have been discovered to shift T_t such as ELP concentration and MW [174, 201] or pressure [211]. By modifying one of these factors, the folding transition can be driven isothermally [57, 169].

2.1.5. Energy transductions

As was discussed in detail before, protein folding of thermoresponsive proteins can be induced by the supply of heat. Comparatively, protein folding in warm blooded organisms has to be promoted by other ways [175, 176]. It implies a drop of the T_t below physiologic temperature which can, for example, be achieved by the increase in concentration of a certain substance, thereby changing the Gibbs energy and shifting the reaction in one direction [175, 176]. The decrease of T_t by the supply of Gibbs free energy by other ways was termed the ΔT_t mechanism [175, 176]. Gibbs energy conversions have been analyzed in the pioneering works of Urry, reviewed in [59, 175, 176]. These energy conversions can include changes in temperature, mechanical force, pressure [211, 212], electromagnetic radiation [213] and the concentration or oxidative state of specific substances, which can alter the chemical [202, 214, 215, 216, 217] or electrochemical potential [218].

The T_t mechanism on cross-linked ELP matrices has led to interesting observations by Urry and coworkers in the late 80s [214, 215, 219]. An elastomeric matrix was generated by cross-linking a protein-dense phase above its T_t via γ-radiation from a ^{60}Co source [V] where the final absorbed dose was 20 Mrad [49]. Heating the elastomeric matrix above T_t led to its contraction via the folding transition. It was reported that weights, with 1000 times the weight of the dry matrix, were lifted [214]. The process was termed a thermomechanical energy transduction [220].

[V] They employed a radiation of 8000 Roentgen/min such that a final absorbed radiation dose of 20 Mrad (with 1 rad = 0.01 Gy) was achieved.

It was further observed that, in analogy to the properties of non-cross-linked material, a modification of the sequence in terms of hydrophobicity, changed the T_t [73]. When the ELP construct was modified by the introduction of carboxyl groups, the matrix showed a stretch-induced pK_a increase of carboxyl entities, corresponding to an increase in free energy [57, 214, 215, 217]. The T_t was shifted depending on pH whereby charges increased the T_t and the cross-linked matrix showed a proton-driven transition with positive cooperativity. The process was termed mechanochemical transduction [214, 215]. The general molecular basis underlying the elastomeric force of the matrix was assigned to be the competition for hydration where the hydration of polar molecules occurs at the expense of hydrophobic hydration as the water structure surrounding charges is incompatible with hydrophobic hydration [59].

The potential use of the ΔT_t mechanism in responsive drug delivery has been discussed in earlier reviews [175, 176]. A regulated drug release was assumed for the contraction and swelling cycle of a cross-linked ELP matrix. The idea was expanded to the potential applicability of a chemomechanical transduction mechanism where the introduction of carboxyl charges into the matrix could induce matrix swelling at physiologic pH. An optimized drug delivery system would be designed in such a way that its property changes (such as matrix swelling) would be triggered by the altered biochemical conditions in a pathological milieu, thus rendering it specific for diseased textures [175, 176].

2.2. Self-assembly to micelles

This paragraph will treat some basic concepts of self-assembly and is based on literature of C. Tanford [221, 160] (pages 60-78), J. N. Israelachvili [222, 223, 166] (pages 503-576), and M. Takeo [224] (pages 164-172).

Molecular self-assembly was described by Whitesides and coworkers [225] as "spontaneous association of molecules under equilibrium conditions into stable, structurally well-defined aggregates joined by noncovalent bonds". As already mentioned in chapter 2.1.1, micelle formation can be described as a form of the hydrophobic effect with its driving force being the positive change in water entropy [160]. The process of self-assembly is governed by the interplay of diverse factors, to which belong contributions of the interaction free energy of the involved molecules, the entropic contributions and geometrical aspects [222]. One theoretical approach on self-aggregation is the equilibrium model of self-assembly by Tanford [221, 160]. The model implies the Gibbs equilibrium condition where the chemical potential of all involved molecules is the same [222]:

$$\mu_N^0 + \frac{k_B T}{N} \ln \frac{X_N}{N} = const. \qquad \text{with } N = 1, 2, 3, \ldots \qquad (2.3)$$

With the mole fraction X_N of molecules in micelles with the aggregation number N, the Boltzmann's constant k_B, the temperature T and the free energy μ_N^0 (or the standard chemical potential) per molecule in the micelle (or the free energy μ_1^0 of the trimer free in solution). The chemical potential includes the free energy of molecular motions of the molecule and the free energy deriving from interactions with other molecules [221, 166]. The change in Gibbs free energy ΔG^0 for micelle formation of size N is given by [224]:

$$\Delta G^0 = -k_B T \ln K = -k_B T \ln \left(\frac{X_N}{N}\right) + N k_B T \ln X_1 \qquad (2.4)$$

With the Boltzmann constant k_B and the equilibrium constant K, given by the mole fraction X_N of micelles with size N and the number of monomers X_1. Micelles form spontaneously in aqueous solution when $\Delta G^0 < 0$, whereas at $\Delta G^0 = 0$ (with $K = 1$) most monomers stay in solution [224]. This can also be expressed in terms of the difference in free energies where most molecules will be in the monomer state when the free energies equal ($\mu_N^0 = \mu_1^0$) while spontaneous micelle formation occurs when $\mu_N^0 < \mu_1^0$ [224]. Here, μ_N^0 is the free energy of an amphiphile in a micelle and μ_1^0 is the free energy of a separate amphiphile in solution. Differences between these values originate solely from interactions with solvent or other monomers [221]. It has to be noted that the process of micelle formation differs from phase separation in the aspect that aggregates formed are not of infinite size. This arises from the composition of amphiphiles, which leads to aggregates that are composed of a finite number N monomers with a minimum free energy μ_N^0 in an aggregate of defined size [166].

The solubility of amphiphiles in water is determined by the length of the hydrocarbon chain and by the concentration of amphiphilic molecules [224]. The onset of particle formation is thus dependent on the monomer concentration in solution which is known as the critical micelle concentration which decreases as the chain length increases [221, 160]. Micelle formation was described as a process of "opposing forces": While hydrophobic forces promote the diminishment of contact area between hydrophobic molecules and water, hydrophilic headgroups tend to increase this contact area [160]. The interaction free energy μ_N^0 per molecule in the micelle is thus determined by the particle structure [224]. It results from contributions of the attractive hydrophobic or interfacial tension forces and the electrostatic repulsion forces between the headgroups as well as steric repulsion between headgroups and between hydrophobic chains [222, 224]. Attractive and repulsive components can be summarized by formula 2.5, where the attractive contributions between hydrocarbon chains have been defined as interfacial free energy per unit area γ from the area of the hydrocarbon-water interface a [222, 223]. The overall repulsive free energy contributions are incorporated in the term C/a where C is a constant including all repulsive portions of the interfacial area a [222].

$$\mu_N^0 = \gamma a + C/a \tag{2.5}$$

As mentioned in chapter 2.1.1, the limited solubility of hydrocarbons in water is due to the much larger free energy of attraction between water molecules between themselves in comparison to the interaction free energy between hydrophobic molecules and water [221]. This gives rise to the hydrophobic effect which is characterized by the tendency of hydrophobic molecules to minimize their contact to water. Thus, micelles were not believed to be formed due to strong attractive forces, as hydrophobic forces between hydrophobic molecules were shown to be comparatively small [160]. This absence of strong attractive forces brings upon the fluidity of the formed structures which would otherwise present a rather rigid and less flexible compartment [221]. The contribution of repulsive forces by anionic headgroups (such as the foldon domain at neutral pH [37]) increases with surface area or pH, while it decreases with ionic strength [223, 226].

The contributions of attractive and repulsive forces result in an optimal "headgroup surface area" a_0 at which the total interaction free energy is minimal. The formation of a specific vesicle or micellar structure is thus dictated by this optimal headgroup surface area a_0 where energetic and packing constraints favor the formation of assemblies with the lowest possible aggregation number. Another restriction is given by entropic terms, as assemblies with lower aggregation number are entropically favored. This explains why single chained amphiphiles prefer to self-assemble into small micellar aggregates instead of the formation of larger vesicles or bilayer structures [222]. Comparatively, when double-chained lipids do not form micelles, this is because of energetic and geometrical reasons. The aggregation number of self-assembly structures increases in the following order: spherical micelle, cylindrical micelle, spherical vesicle, planar bilayer [222].

The packing constraints that dictate the dimensions of self-assembly structures can be explained by geometrical arguments. Important factors are the micelle radius of curvature R, the

hydrocarbon-water interfacial area a with the hydrocarbon chain volume v and thickness l. Considering a spherical micelle with a radius R that equals l, the following relation holds [222]:

$$\frac{4\pi R^3}{3v} = \frac{4\pi R^2}{a} = N \tag{2.6}$$

It can be seen from this that the surface area a depends on the number of amphiphiles N in the aggregate which is optimal for a_0 and when ΔG^0 is minimal. For certain values of N, the value of ΔG^0 will be positive and no micellization will occur. It follows that stable micelles feature a narrow size distribution [224]. From equation 2.6 the following relation is obtained for spherical micelles [222, 223]:

$$\frac{v}{a_0} = \frac{l_c}{3} \tag{2.7}$$

The radius of the micelle must thereby not exceed a critical hydrocarbon length l_c [221, 223]. Also the headgroup area has an upper limit for feasible values as too large areas would result in an increased contact between hydrophobic chains and water, involving diminished hydrophobic driving forces of micelle formation. Micelles formed by longer hydrocarbon chains have smaller surface-to-volume ratios and larger aggregation numbers where the headgroup areas are generally smaller [160, 221]. The lower limit of the headgroup area is dictated by the repulsion between the charged headgroups [221]. The addition of salt can diminish electrostatic interactions by screening the charges of the hydrophilic headgroup. Simultaneously, salt can influence hydrophobic interactions and thus also has an impact on the phase transition of ELPs [37]. A geometric consideration of the nanoparticle used in this work based on Israelachvili's concepts of packing constraints in self-assembled structures [222] can be found in chapter 4.1.3.

2.3. Stability aspects of nanoparticle solutions

Since particle aggregation can affect the toxicity and reactivity of a particle system [227] and thus its biomedical applicability, it is of highest interest to understand the causes of aggregation in order to improve a particle solution's properties. Particle interactions are influenced by a range of factors including shape, size, surface composition and solution conditions [228]. This section gives a brief introduction on the forces involved in particle interaction and aggregation. It is mainly based on the works of J. Israelachvili and coworkers [166, 229, 228].

Long-range forces between particles that are smaller than 100 nm in diameter are controlled by Brownian diffusion, causing collisions between the particles [227]. These collisions between the particles and water molecules can have a sufficient force-to-mass ratio to compensate for the tendency to settle due to gravitational force [230]. Thus, small particles of soft matter with diameters below a critical value (typically below 100 nm) are less likely to settle during long-term incubation. When particles in solution collide with each other, the particles can either adhere or repulse, depending on whether the forces are predominantly attractive or repulsive [227].

Particle interactions in solution have been described by the Derjaguin-Landau-Verwey-Overbeak (DLVO) theory [231, 232]. It includes the VdW and electrostatic double-layer (edl) forces which are both long-range forces [228]. The VdW interaction energy E_{VdW} originates from the fluctuating electric dipole moments of molecules [228]. It includes dipole-dipole interactions (Keesom), interactions between dipoles and induced dipoles (Debye) and interactions between two induced dipoles (London-Dispersion) [166]. For two particles of radii r_1 and r_2 at a large separation distance d, the London equation defines E_{VdW} as:

$$E_{VdW} = -\frac{16Ar_1^3r_2^3}{9d^6} \qquad \text{for } d > r_1, r_2 \qquad (2.8)$$

Comparatively, for two spherical particles whose centers are a distance d apart which is much smaller than their respective radii r_1 and r_2 (typically $d < r/100$), E_{VdW} is defined as [166]:

$$E_{VdW} = -\frac{A}{6D}\left(\frac{r_1r_2}{r_1 + r_2}\right) \qquad \text{for } d \ll r_1, r_2 \qquad (2.9)$$

Both relations include the material specific Hamaker constant A. Particles that are more prone to aggregate feature a higher Hamaker constant A [227]. When the attractive VdW interaction between particles of alike materials becomes dominating, they eventually coalesce into larger aggregates [233]. It has to be noted that other attractive forces such as ionic, H-bonding or hydrophobic forces can be stronger than the VdW force and thus determine the interaction if they are present [228]. The electrostatic "double-layer" interaction energy E_{edl} between two charged spherical particles decays exponentially with their distance d [166]:

$$E_{edl} = \left(\frac{r_1r_1}{r_1 + r_2}\right) Ze^{-\kappa d} \qquad \text{for } d \ll r_1, r_2 \qquad (2.10)$$

The expression is appropriate for spherical particles at distances d smaller than their radii r_1 and r_2. It involves the Debye length κ^{-1} as characteristic decay length of the interaction and the interaction constant Z which depends on the electrolyte valency and the particle surface

properties [228, 166]. As the Debye length κ^{-1} depends on the solution conditions, the electrostatic double-layer repulsion can be influenced by salts and pH. A high surface charge density σ increases the stability of particle solutions [228]. Upon the approach of the two surfaces, the particles eventually repel each other due to the overlap of the electric double layers. This effect can be influenced by salts and pH: At high ionic strength, the Debye length κ^{-1} of a particle decreases as the salt compresses the layer, leading to a reduced electrostatic double layer repulsion. The critical coagulation concentration (ccc) marks the point of complete electrostatic screening at which the particles eventually coalesce into larger aggregates [227]. It was observed that divalent ions such as $MgCl_2$ or $CaCl_2$ provoked a lower ccc than monovalent ions [234, 235]. Additionally, it was found that the salt effect is increased for smaller particles [236]. Comparatively, a specific pH can cause the particle surface to have a neutral charge, which can promote aggregation via a dominating VdW interaction [227].

The DLVO theory describes particle interactions in terms of their interaction energies, where the VdW and edl interactions contribute to the interaction between two molecules as a function of distance [228]. The interaction is attractive at very small and very large separations, which can cause the trapping of particles in two different minima, denoted as primary and secondary minimum [228]. Particles in the secondary minimum are reversibly aggregated (and can be re-dissolved by the application of shear-forces) whereby particles in the primary minimum are characterized as irreversibly aggregated [227, 237]. When the separation distance between two particles becomes smaller than their particle diameter, the attractive forces are larger for non-spherical particles as these have a greater number of atoms in close proximity [238]. For a transition into the primary well, particles have to overcome a specific force barrier that increases with the surface charge density σ of the particles. For particles with high surface charge in low salt conditions the barrier is typically largest when the particles are at a distance of 1 to 5 nm. This energy barrier is usually of the order of several kT [166]. For particles with low surface charge this barrier can become very low (and even below zero), which results in coagulation [166].

At very small distances, where the VdW force would dominate the interaction, other forces can get involved, including steric, hydration and hydrophobic interactions. Therefore, the analysis of surface interactions at small distances can get very complex. Additional interaction terms established so far are summed up under the notation extended DLVO theory [227]. Some of its aspects that might be of primary interest for the analysis of the nanoparticle system presented here, will be shortly mentioned in the following.

There can be different structural forces in water: At close approach of two surfaces, hydration forces can influence the interaction between the two surfaces. Thereby, solvent-solvent interactions can make attractive or repulsive contributions, depending on the orientation of the bound water molecules [228]. A primary hydration shell bound to the surface of a particle causes surface-solvent interactions that can decrease adhesive forces between two surfaces [228]. Hydrophobic forces can be much larger than the VdW interaction if the material has a small Hamaker constants, such as is true for hydrocarbon surfaces [228]. The hydrophobic interaction energy between to hydrophobic surfaces increases exponentially with decreasing distance and can result in the aggregation of hydrophobic particles in water [228].

The repulsive "steric" force is counteracting the attractive terms and is defined by the macromolecule's surface structure. It influences to which distance the two particles can approach and thus has an impact on the adhesion energy between the interacting spheres [228]. If the structure is flexible, the overall binding energy can be maximized via rearrangements [228]. Such a surface restructuring can evolve very slowly in the range of days and lead to increased adhesive VdW contacts [228]. This can also lead to an attractive electrostatic interaction through the formation of discrete ion pairing. This effect is facilitated by the fact that at very short separations, a surface does not present a net overall charge but is characterized by its individual charges [228]. These effects might be of interest when comparing nanoparticles below and above T_t. Swollen particles below T_t might expose peptide chains, due to a presumably more loose, open and flexible structure of the outer third of the particle. This open conformation of the particles may provoke increased adhesive interactions between deformed particles which may finally lead to particle coalescence.

The stability of a particle solution can be increased by the addition of polymers to the surface which can provide electrostatic stabilization via the introduction of charges [233]. Electrostatic stabilization can also lead to the formation of a hydration layer which can act against particle aggregation [233]. In case of the presented nanoparticle system, the foldon headgroup acts as electrostatic surface and most likely features a bound hydration layer, which is assumed to provide particle solution stability.

3. Material and Methods

3.1. Material

3.1.1. Laboratory equipment

AFM	MFP-3D SA Asylum Research, Santa Barbara, CA
Branson Sonifier 250	Heinemann Ultraschall- und Labortechnik
Centrifuge	Sorvall Evolution RC (rotors SS-34 / SLC4000)
Confocal microscope	Leica Type TCS SPS II, Leica Microsystems CMS GmbH
DLS	Zetasizer nano series instrument Malvern Instruments, United Kingdom
Incubator	Sartorius Cartomat BS-1
Oven	Universal Oven UNB300, Memmert
pH Meter	Digital Labor pH Meter Lab850 SI Analytics GmbH Mainz
	Laboratory pH Meter CG 842 SCHOTT Geräte GmbH
pH electrode	InLab® Micro Pro Mettler-Toledo GmbH
UV-Vis	Peqlab Biotechnologie GmbH, ND-1000
	Amersham Biosciences GeneQuant pro
Table centrifuge	Heraeus Biofuge fresco
TEM	JEOL JEM 100CX
Thermomix	Eppendorf Thermomixer comfort

3.1.2. Chemicals and material

α,ω-bismaleinimide poly(ethylene glycol)	Rapp Polymere
Ammonia (32%)	VWR
Ampicillin trihydrate	VWR
Atto647N NHS-ester	ATTO-TEC
BL21 (DE3)-T1^{R} Competent Cells	Sigma-Aldrich

DyLight™ 594 NHS-ester	Thermo Fisher Scientific
Dithiothreitol (DTT)	Sigma-Aldrich
Filter paper	Whatman grade 1
Filters (regenerated cellulose), 0.2 µm	Corning®
Neutral fluorescein isothiocyanate (FITC)-dextrans	Sigma-Aldrich
Gel Extraction Kit	Qiagen
Glycine	Sigma-Aldrich
Hellmanex	VWR
Highly Oriented Pyrolytic Graphite (HOPG) (thickness dispersion ± 0.2 mm)	NT-MDT Service and Logistics, Limerick, Ireland
Hydrogen peroxide (35%)	VWR
Isopropyl β-D-thiogalactopyranoside (IPTG)	VWR and Sigma-Aldrich
Kaleidoscope Precision Plus	Bio-Rad
Laemmli	Bio-Rad
LB Broth (Lennox)	VWR and Sigma-Aldrich
2-(N-morpholino)ethanesulfonic acid monohydrate (MES)	VWR
Mini-PROTEAN TGXTM gel (4-20 %)	Bio-Rad
Silicon nitride cantilevers, MLCT	Bruker SPM Probes
Phosphate buffered saline (PBS) tablets	Sigma-Aldrich
Pur-A-Lyzer Maxi dialysis devices (12 kDa MWCO)	Sigma-Aldrich
Plasmid Mini Kit	Qiagen
Quick ligation kit	New England Biolabs
Restriction enzymes: NdeI, PflMI, BglI	New England Biolabs
Slide-A-Lyzer MINI dialysis devices (20 kDA MWCO)	Thermo Fisher Scientific
Sodium hydroxyde (NaOH) (10 M)	Sigma-Aldrich
Sodium phosphate dibasic heptahydrate	Sigma-Aldrich
Sodium phosphate monobasic monohydrate	Sigma-Aldrich
UV cuvette micro (8.5x10 mm)	VWR

3.1.3. Buffers and solutions

Agar plates LB_{amp}

Agar	15 g
LB_0	1 L
Ampicillin (100 mg/mL)	1 mL

BL21 (DE3)-T1 frozen glycerol stock

BL21 (DE3)-T1 culture in LB_{amp}	500 µL
Glycerol (50 % v/v)	500 µL

Destain solution

Acetic acid	100 mL
H_2O_{dd}	900 mL

Medium LB_0 (Lennox), 1 L

NaCl	5 g
Peptone	10 g
Yeast extract	5 g

Medium LB_{amp} (Lennox), 1 L

LB_0	1 L
Ampicillin (75 mg/mL)	1 mL

Phosphate buffer (0.1 M, pH 8.0)

Sodium phosphate monobasic monohydrate, 0.2M	15.9 mL
Sodium phosphate dibasic heptahydrate, 0.2 M	284.1 mL
Double distilled water (H_2O_{dd})	300 mL

Reaction buffer *(Typical salt conditions in solution after cross-link)*

MES	0.3 mM
Phosphate buffer	0.3 mM
Cross-linker α,ω-bismaleinimide poly(ethylene glycol)	< 0.8-1.2 mM
pH	6-7

RCA solution

H_2O_{dd}	500 mL
Ammonia (32 %)	100 mL
Hydrogen peroxide (35 %)	100 mL

SDS-PAGE running buffer (10x), 1 L

Tris	250 mM
Glycine	2 M
SDS (10 w/v)	100 mL

SDS-PAGE sample buffer

Laemmli	500 µL
SDS	7.1 % w/v
DTT	250 mM

Standard buffer: Phosphate buffer (10 mM, pH 8.0-8.4)

Phosphate buffer (0.1 M, pH 8.0)	100 mL
H_2O_{dd}	900 mL
Addition of NaOH (0.1 M)	
pH 8.0-8.4	

3.1.4. Polypeptide solution

The following protein sequence was used as basic building block for nanoparticle formation:

MGH(GVGVP)$_{36}$-(GCGVP)(GVGVP)$_{21}$-GV-GYIPEAPRDGQAYVRKDGEWVLLSTFL-GPGWP

The sequence is composed of 327 amino acids and has a MW of 27811.7 g/mol. The hydrophobic ELP sequence is at the N-terminal part while the foldon is at the C-terminus of the peptide sequence. It facilitates the assembly of the construct into a trimeric form. The sequence features tryptophane (W) for protein concentration determination. The molar extinction coefficient ε is 14065 $M^{-1}cm^{-1}$ as determined according to the method of Gill and von Hippel [239].

3.2. Methods

3.2.1. Gene design

The gene design was carried out according to the protocol reported by Ghoorchian et al. [37] in which a modification of the recursive directional ligation from Meyer and Chilkoti [63] is described. The method employs successive ligation of genetic sequences encoding for the pentapeptide. Herein, the sequence had cutting sites for the restriction enzymes *Nde*I, *Pfl*MI and *Bgl*I. A construct with the sequence (GVGVP)(GCGVP)$(GVGVP)_{21}$ was double digested with *Nde*I and *Pfl*MI and a construct of $(GVGVP)_{35}$ was double digested with *Nde*I and *Bgl*I. The samples were separated via agarose gel electrophoresis, followed by purification via gel extraction (gel extraction kit, Qiagen). The purified constructs were ligated with a quick ligation kit (New England Biolabs), inserted in a pET-20b expression vector which was transformed into an *Escherichia coli* (*E. coli*) BL21 (DE3)-T1 strain (Sigma) as described below. The final construct was sequenced by the Cleveland Clinic Genomics Core and by GATC Biotech AG (Konstanz, Germany). For sequencing by GATC, the plasmid was extracted with the Qiagen® plasmid purification kit.

3.2.2. Bacteria transformation and frozen stocks

The plasmid designed according to section 3.2.1 was used for transformation of bacteria of the *E. coli* strain BL21 (DE3)-T1 (Sigma). Cell aliquots were taken from -80 °C storage and allowed to thaw on ice. The cells (50 µL) were mixed with vector solution (1 µL) and incubated on ice for 15 min. Cell permeability was induced by 1 min heat shock at 42 °C, followed by incubation on ice for 10 min. The solution was mixed with 900 µL medium LB_0 and incubated on a thermomixer for 1 h at 300 rpm and 37 °C. Cells were harvested by centrifugation at 5000 rpm for 3 min and resuspended in 100 µL LB_0. The cells were streaked on LB_{amp} agar plates and incubated overnight (o/n) at 37 °C. The grown colonies, positive for the transformed vector, contained the gene construct of interest. Frozen stocks were made by transferring a colony of the transformed bacteria into 25 mL LB_0 medium. After o/n incubation at 37 °C and 300 rpm, the culture was transferred to 250 mL LB_0 and incubated (37 °C, 300 rpm) until an optical density at 600 nm (OD_{600}) of 0.4-0.5 was reached. The frozen stocks were made by the addition of 500 µL glycerol (50 % v/v in H_2O) to 500 µL of culture. The aliquots were stored at -80 °C.

3.2.3. Protein expression and purification

For protein expression, a starter culture was made containing 250 µL of the frozen stock in 150 mL LB_{amp} which was incubated o/n (120 rpm, 37 °C). The culture was transferred to 0.8-1.0 L of LB_{amp} in a 2 L Erlenmeyer flask and incubated until an OD_{600} of 0.8 was reached. At this point, protein expression was induced by the addition of isopropyl-β-D-thiogalactopyranosid (IPTG) (0.1 mM), followed by incubation (120 rpm, 37°C, 4-7 h). The cells were harvested by centrifugation for 30 min at 3000 g and were kept at -20 °C o/n. After resuspension of each pellet in 15 mL PBS and homogenization via vortexing, the cells were lysed on ice by sonication with a Branson Sonifier 250 (Heinemann Ultraschall- und

Labortechnik), applying a 30 % duty cycle and an output control 6. The purification procedure was done by the ITC [65, 66] which is based on multiple centrifugation steps below and above the specific T_t for the used construct. A first centrifugation was carried out at 4 °C for 20 min and 14000 g, leading to a pellet of the cell debris resulting from cell lysis. The supernatant contained the dissolved ELP which was used in a second centrifugation step at 40 °C (20 min, 14000 g). A pellet with the concentrated ELP coacervate was obtained. The pellet was resuspended in phosphate buffered saline (PBS). The procedure was carried out three times after which the ELP was finally dissolved in standard buffer. The solution was filtered with membranes of regenerated cellulose containing a 0.2 µm pore size (Corning). The expression yield was defined by UV-Vis measurement at 280 nm with a spectrophotometer ND-1000 (peqlab Biotechnologie GmbH). The expression yield was typically around 20 mg/L.

3.2.4. Protein detection

3.2.4.1. SDS polyacrylamide gel electrophoresis (SDS-PAGE)

The purity of the sample was confirmed by SDS-PAGE, by which proteins can be separated according to their MW. In this method, proteins are dissolved and unfolded by the addition of SDS. The protein obtains a net negative charge with SDS bound at a constant mass fraction (approximately 1.4 g SDS / 1 g protein). This causes the molecule to move towards the anode when an electrophoretic field is applied [240]. The method according to Laemmli was performed with a 4-20 % Mini-PROTEAN TGXTM gel (Bio-Rad). The gel was inserted into an electrophoresis chamber and filled with SDS-PAGE running buffer (1x). The samples were mixed 1:1 (v/v) with Laemmli sample buffer, containing 7.1 % (w/v) SDS and 250 mM DTT. They were heated for five minutes at 95 °C and then applied to the stacking gel. The heating and the presence of SDS facilitated the dissociation of the trimeric foldon, while the sulfide groups are reduced by DTT. The marker Kaleidoscope Precision Plus (Bio-Rad) was used as MW standard. The separation was started with the application of 60 Volt until the samples passed the stacking gel, then it was increased to 120 Volts and stopped when the migration front had reached the end of the gel. The gel was destained in diluted acetic acid (10 % v/v).

3.2.4.2. Ultraviolet-visible spectroscopy

The growth of the *E. coli* culture was tracked via the increase in OD_{600} using a spectrophotometer (Amersham Biosciences GeneQuant pro). The determination of protein concentration after purification and before cross-link was carried out with a spectrophotometer ND-1000 (peqlab Biotechnologie GmbH) at 280 nm. The same instrument was used for definition of labeling degrees after trimer-modification with Atto647N-NHS and DyLight™ 594-NHS respectively.

3.2.5. Particle formation and chemical cross-link

The protein sample was equilibrated to RT and dissolved in H_2O_{dd}, providing a low-salt protein solution. The sample was typically allowed to equilibrate at RT for 1-2 h before use. Buffer conditions had to be optimized with view to the salt and pH conditions. A basic starting pH was needed to facilitate micelle formation. In most experiments NaCl was excluded to keep micelle

sizes at a minimum. The concentration of NaCl is indicated in the results if present. The final protein concentration was 20 µM and the pH was adjusted to 9.6-10.3 by the addition of NaOH (0.1 M). The samples and an aliquot of H_2O_{dd} for cross-linker dilution were stored in an oven above T_t (50-55 °C). The aliquots were incubated for 0.5-2 h before cross-link to ensure a well equilibrated solution temperature with a homogeneous nanoparticle solution.

Cross-linking with maleic acid imide (maleinimide [VI]) functionalities is a well-established method for the modification of sulfhydryl groups [88, 230, 241]. The reaction presented in Reaction Scheme 1 shows the reaction scheme which follows a Michael addition: The free sulfonyl group of a cysteine reacts as nucleophile with the non-saturated carbonyl group of the maleinimide. The double bond undergoes an alkylation reaction whereby a stable thioether bond is formed. On the one hand, the reaction is specific for thiol groups in the pH range 6.5-7.5 [242, 243] where its reaction rate is around 1000 times greater for cysteines than for amines [244]. On the other hand, the cysteine side chain is much more reactive in its deprotonated thiolate form in basic conditions [245] where other reactions can compete, which is discussed in 4.2.3.

As cross-linker served the homobifunctional α,ω-bismaleinimide poly(ethylene glycol) (PEG) linker with a MW of 2 kDa (Rapp Polymere, Tübingen, Germany). The cross-linker (approximately 6 mg) was freshly dissolved in 100 µL MES solution (10 mM, pH 7.5). In some instances, NaCl was added and respective concentrations are indicated in the results if present. The solution was mixed by short vortexing, spinned down and then diluted in H_2O_{dd} in a 1:10 (v/v) ratio. The solution was equilibrated above T_t and then added to the nanoparticle solution in a 1:2 (v/v) ratio with 100 µL cross-linker solution in 200 µL particle solution. The reaction was run in 0.3 mM standard buffer / 0.3 mM MES o/n in an oven above T_t (50-55 °C). The cross-link protocol implied the use of a nearly 100-fold molar excess of cross-linker over protein, with final concentrations of 0.8-1.2 mM cross-linker and 13 µM protein respectively. With a maleinimide concentration of 706 µmol/g in the cross-linker powder as given in the specifications data sheet and considering the dilution factors, a concentration of approximately 1.4 mM reactive groups can be estimated. With a concentration of cysteine groups of 40 nM (given the protein sequence with 327 amino acids), this leads to a 35000-fold molar excess of cross-linker over protein.

[VI] This functional entity is either spelled maleinimide or maleimide in literature.

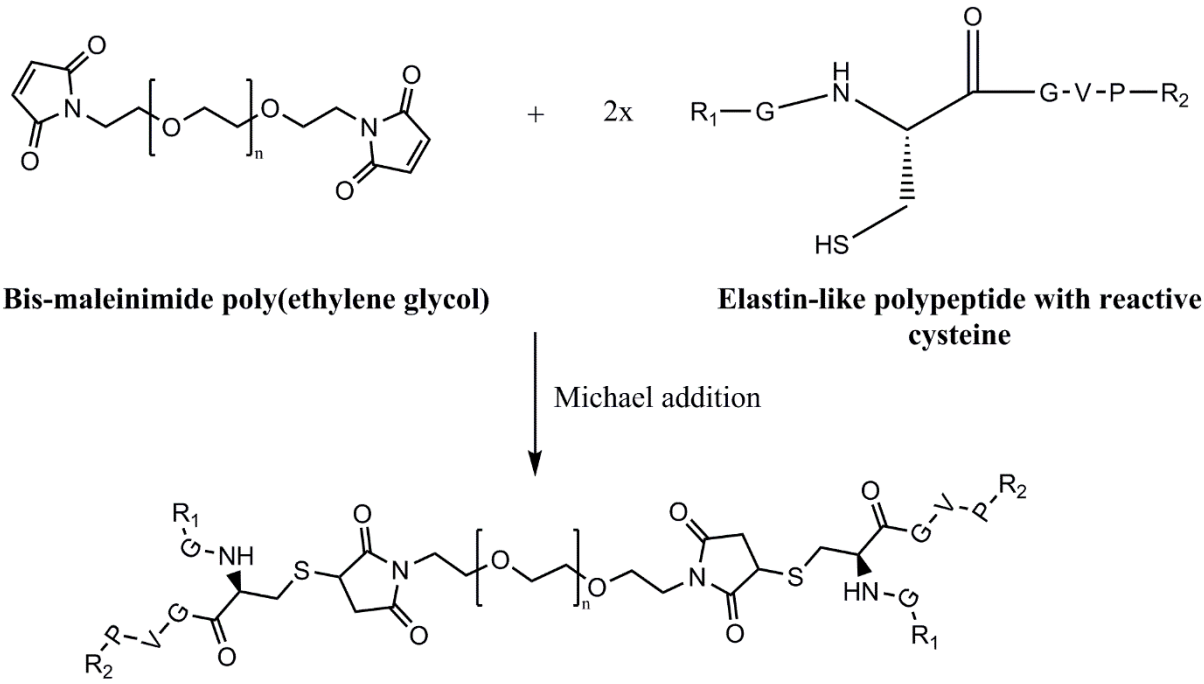

Reaction Scheme 1: Reaction scheme showing cross-link of two ELP chains with a bis-maleinimide poly(ethylene glycol) (PEG) linker via a Michael addition. Reaction scheme adapted from Hermanson, 2008 [230] and adjusted to the ELP system and the homobifunctional linker used in this work.

For analysis and further modifications, the particles were dialyzed o/n against standard buffer in an incubator above T_t at 70 rpm with Slide-A-Lyzer MINI dialysis devices (Thermo Fisher Scientific) with a cutoff membrane of 20 kDa. The dialysis temperature was typically around 43 °C to prevent membrane damage at higher temperatures. The samples were stored below T_t (RT) or in an oven above T_t (50-55 °C). Purification after long time storage was carried out via centrifugation if indicated.

3.2.6. Particle size measurements

3.2.6.1. Dynamic light scattering (DLS)

DLS is a method for the determination of particle sizes in fluid [246]. It is also known as photon correlation spectroscopy (PCS) or quasielastic light scattering (QELS). The experimental setup is illustrated in Figure 7, derived from a basic scheme given in [246]. It is composed of a laser source illuminating the analyte in solution, a cuvette with the solution of interest, a detector, a signal analyzer and a computer. Particles in the solution cause a scattering of the light. This can be observed on the detector which is located at a distinct angle θ. The detector, typically a photomultiplier, is connected to a correlator as signal analyzer and a computer for data conversion and analysis.

The molecules in solution can be seen as single scattering centers which scatter light in different directions. The light paths originating from these different scattering centers can be different in phase which results in constructive or destructive interference. As a result of thermal diffusion

known as the Brownian motion of the molecules, the scattering pattern on the detector will fluctuate [247].

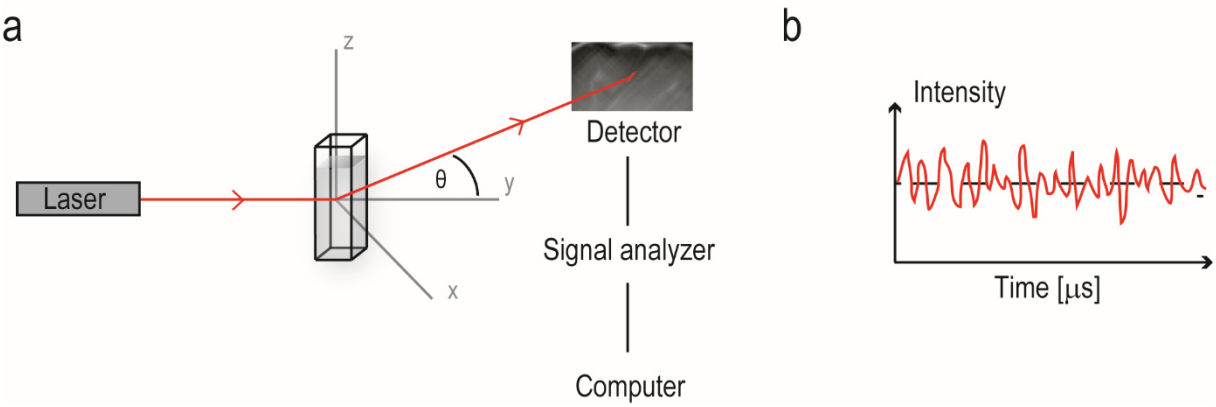

Figure 7: Experimental setting of a dynamic light scattering (DLS) experiment, with basics derived from reference [246]. **(a)** A laser source illuminates the scattering volume and gets scattered by the analyte. The scattering pattern is detected under a distinct angle θ with respect to the beam's propagation direction. The signal is analyzed and data is sent to a computer. **(b)** The fluctuations of the scattered light are recorded over time.

The measurement principle of DLS is based on the time-dependent intensity fluctuations of the light whereby the number of photons is measured in time intervals over a distinct time period and then analyzed via an autocorrelation function [246]:

$$G(\tau) = \lim_{T\to\infty} \frac{1}{2T} \int_{-T}^{T} I(t)I(t+\tau)dt \qquad (3.1)$$

The intensity of a signal *I(t)* is multiplied with its signal intensity after a specific time interval τ, the correlation time interval. At the beginning of the experiment, the difference in signal intensities will be at a minimum and increase over time. As small molecules diffuse quickly, they cause a fast fluctuation of the scattering signal [246] and an autocorrelation function with a steep decay [247]. The measurement gives an intensity-weighted particle distribution of all different particle sizes in solution [248].

There are multiple approaches for fitting the correlation function to derive the average diffusion constant *D* of a certain particle population. The choice is depending on the homogeneity of the solution. A monodisperse solution will feature a correlation function with a single exponential decay while a polydisperse solution will produce a correlation function consisting of a sum of exponential decays [247]. For the translational diffusion of a monodisperse sample (of non-interacting solid spheres), the theoretical form of the correlation function has a single exponential decay which can be written as [248]:

$$g^{(1)}(\tau) = e^{-Dq^2\tau} \qquad (3.2)$$

The term Dq^2 defines the correlation decay constant Γ [249]. The scattering vector q is dependent on the scattering angle θ, the wavelength λ of the incident light in vacuum and the solution index of refraction n as follows [247]:

$$q = \frac{4\pi n}{\lambda_0} \sin\left(\frac{\theta}{2}\right) \qquad (3.3)$$

By fitting the correlation function with a suitable algorithm, the translational diffusion coefficient D can be extracted. The cumulants analysis introduced by Koppel [250] can be used for monodisperse samples [251]. It derives an average decay rate of the distribution (the first cumulants K_1) and the distribution width around the average value (the second cumulants K_2). Values derived from the cumulants analysis are the Z-Average diffusion constant and the polydispersity index (PI) [247, 248]. Solutions with a PI smaller 0.1 are considered monodisperse [252]. In polydisperse solutions, the different size populations will contribute to the correlation function which will therefore be a sum of exponentials. The diffusion constants can be extracted by multi-exponential fitting methods such as CONTIN or the non-negative least squares algorithm. The DLS instrument used in this work (Zetasizer Nano ZS, Malvern Instruments, United Kingdom) contains a "Protein Algorithm" for data analysis which is a standard regularized non-negative least squares algorithm.
The diffusion constant D is related to the particle's hydrodynamic radius R_H via the Stokes-Einstein relation, with the Boltzmann's constant k_B (with $1.38 \cdot 10^{-23}$ J/K), the temperature T and the viscosity η of the solvent [246]:

$$D = \frac{k_B T}{6\pi\eta R_H} \tag{3.4}$$

DLS measurements were carried out with a commercial instrument of the Zetasizer Nano ZS series from Malvern Instruments (United Kingdom). The instrument was composed of a 4 mW He-Ne gas laser at 632.8 nm and a detector at 175° scattering angle (non-invasive backscatter detection). Thermal cycling measurements were conducted below T_t (25 °C) and above T_t (55 °C). The sample temperature was regulated with a Peltier instrument. Before each measurement, the sample was typically equilibrated for five to ten minutes to achieve a stable count rate during measurement and to ensure that particle sizes were fully equilibrated. A measurement was typically a set of 10 runs with 30 seconds (s) run duration each. The software version 7.03 was used for measurement and data analysis. The autocorrelation function was analyzed via the Cumulants Analysis and the Protein Algorithm provided by the Malvern Software. Sizes are derived from the particle size distribution (PSD) by intensity, if not otherwise noted.

3.2.6.2. Fluorescence correlation spectroscopy (FCS)

Fluorescence correlation spectroscopy (FCS) is a method that allows the determination of the diffusion coefficient from fluorescently labeled freely diffusing molecules excited by lasers in a confocal microscope. These measurements were carried out to verify the size data obtained from DLS measurements. Sample preparation of nanoparticle solutions (labeled with Atto647N as described in section 3.2.8) involved dilution in standard buffer in a 1:100 (v/v) ratio, followed by incubation at RT for some days to allow potential larger aggregates to be removed via sedimentation. Before measurement, the sample was equilibrated at the measurement temperature for around 10 min.

A home-built confocal microscope was used for measurements, which resembled other published setups [253, 254, 255]. A pulsed 640 nm laser was used for excitation of the labeled nanoparticles and time traces of photons were recorded with a single photon avalanche

photodiode (PDM-50 µm, PicoQuant). A commercial data acquisition system (HydraHarp 400, PicoQuant) with picosecond time resolution was used. The correlation function was fit with equation 3.5 [256, 257, 258, 259], from which the diffusion time τ_d was obtained.

$$G(\tau) = \left(1 - T + Te^{(-\tau/\tau_T)}\right)\left(1 + \frac{\tau}{\tau_d}\right)^{-1}\left(1 + \frac{\tau}{\tau_d \kappa^2}\right)^{-1/2} \quad (3.5)$$

With T as the fraction of molecules being in the triplet state and τ_T as the triplet time [258]. The first part of the equation describing the triplet time was only used for fit optimization and was not part of the analysis. The geometrical parameter κ was held constant for each fit and the relative diffusion time τ_d through the confocal volume was extracted from the fit parameters.

Measurement lengths and fitting procedure were varied for the diverse experimental sets showing different degrees of solution heterogeneity where aggregates were observed to be more pronounced in measurements at high temperature. The correlation functions were evaluated via a single, a double or a triple exponential fit respectively, to account for the degree of free dye and aggregated particles that fluctuated between experiments. Details are given below:

Measurements from experiment 1 and 2 were carried out for a duration of 60-300 s. In the first experiment, results were obtained from a fit on the correlation function obtained from a measurement of 120 s length. The data was fit with a single diffusion coefficient with a non-fixed value for parameter α. From the second experiment, a correlation function was obtained from a cutout of 180 s measurement length, which was fit with two diffusion coefficients (with non-fixed α) to account for the fraction of free dye. In the third experiment, the correlation functions resulted from measurements of 10 min length that were split into 30-60 sec intervals. This was done in order to cut out the observed aggregates to enable a fit with one diffusion constant with a non-fixed value for parameter α. Results from experiment 4 are obtained from a fit on the correlation function obtained by 10 min measurement length. The fit involved three diffusion coefficients to account both for free dye and aggregates. In order to keep the number of free parameters of the fit to a minimum, the value for parameter α was set to 1 for both the diffusion coefficient of nanoparticles and aggregates.

As described for DLS evaluation, the experimentally defined diffusion coefficient is directly proportional to the hydrodynamic radius according to the Stokes-Einstein relation given in formula 3.4. The value for the viscosity η of standard buffer was taken from the dispersant specifications in the Malvern software of the DLS instrument, where it was defined to η_{RT} = 0.8948 centi Poise (cP) [10^{-3} kg · m^{-1} ·s^{-1}] at RT. Values for measurements above T_t were $\eta_{42°C}$ = 0.6338 cP, $\eta_{44°C}$ = 0.6124 cP and $\eta_{45°C}$ = 0.6023 cP.

3.2.6.3. Atomic force microscopy (AFM)

AFM is a scanning probe microscopy (SPM) method developed in 1986 by Binnig et al. [260]. It is based on the measurement of forces between a sharp tip and a sample surface, which can be detected by the optical lever method [261, 262]. The small tip acts as a force sensor which enables the user to detect forces in the piconewton range in single-molecule force measurements and to image surfaces with nanometer resolution under native conditions [263]. The setting of an AFM measurement is illustrated in Figure 8 a) which shows the cantilever spring, the sample surface

on a piezoscanner, a photodiode as optical detection system and a feedback circuit. The measurement probe is a sharp tip located at the end of a flexible cantilever with a specific spring constant. A laser beam is focused on the cantilever backside and gets reflected onto a four-quadrant photodiode. As the cantilever gets into contact with the sample surface, interaction forces between the surface and the cantilever cause the cantilever to deflect in z-direction, which produces an electrical differential signal on the photodiode. This signal is proportional to the bending of the cantilever and the deflection is subsequently processed by a computer. The backside of the cantilever is typically coated with a metal layer to provide good reflection of the laser beam. The sample surface is mounted on a piezoscanner that can react in the x-y-z direction with sub-nanometer precision [263].

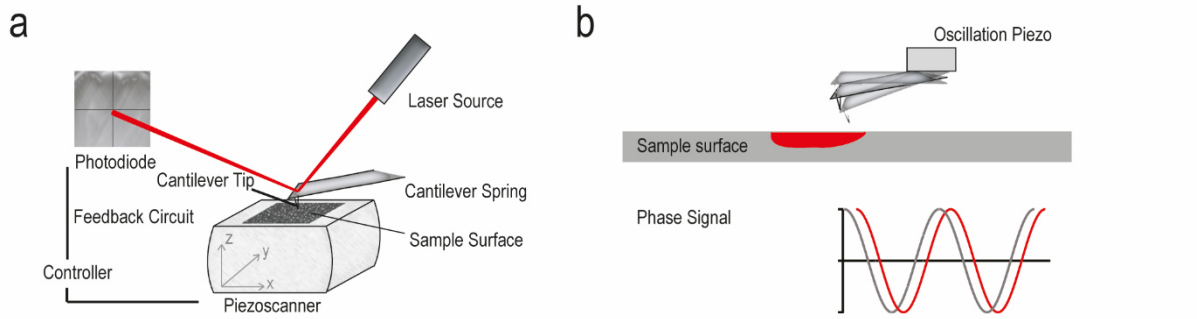

Figure 8: Schematic representation of an AFM measurement setting, based on a representation from reference [263]. **(a)** Basic components are a cantilever with a sharp tip that is in contact with a sample surface, mounted on a piezoscanner. A laser beam is reflected from the cantilever backside onto a four-quadrant photodiode. **(b)** In tapping mode, the cantilever is brought to oscillation near its resonance frequency via an oscillation piezo. Interactions between the sample and tip can differ, depending on the material properties, which can result in phase lags between the piezo-oscillation driver and the resulting oscillation of the cantilever.

Atomic tip-sample interactions can be described by the Lennard-Jones potential with VdW attractive forces at larger distances and electrostatic (Coulombic) repulsion at small distances. Additional forces that can play a role are capillary and frictional forces. Two basic operation modes in AFM are the contact mode and the intermittent-contact mode which can be conducted in air or in fluid. In contact mode, the cantilever is brought into contact with the surface and scanned relative to the surface. In constant force mode, an electronic feedback loop uses the deflection information on the photodiode to drive the piezoscanner in order to maintain a constant force such that a topographic image of the surface is created [263].

Intermittent-contact mode [264, 265, 266], represented in Figure 8 b), is a dynamic mode where the cantilever is induced to oscillate at a frequency ω near its resonance frequency ω_0 via an oscillation piezo. As the surface is scanned, interactions between the sample surface and the tip cause variations in the oscillation amplitude and lead to a new oscillation frequency. A feedback loop is used to keep the amplitude constant. Phase imaging is based on the phase lag between the oscillation signal sent to the piezo-driver and the resulting oscillation of the cantilever. It can give additional information on the material properties as different sample properties can give rise to differences in phase [263, 267, 268]. The phase shift can be related to the alteration in the tip-sample energy dissipation [269]. However, the quantification of the dissipated energy is complex as the phase shift is dependent on a range of different factors such as the amplitude ratio A/A_0 [267, 268] as well as the driving force and cantilever parameters [268]. In the analysis included in this work, the phase shift is analyzed qualitatively in addition to topography, in

order to support the discrimination of protein from the sample surface. One of the main advantages of AFM imaging is the visualization of biomacromolecules under native conditions under ambient buffer and temperature conditions. Intermittent-contact mode with its low lateral [264] and capillary forces [270] is especially useful when imaging soft and biological samples. Regarding the analysis of the size data, one has to be aware that the resulting image represents a convolution of the tip radius with the structures of interest [271]. Typical radii of cantilever tips are 10 nm for etched Si tips and 20-60 nm for standard Si_3N_4 tips [263].

AFM measurements in this work were conducted with a MFP-3D SA (Asylum Research, Santa Barbara, CA, USA). Silicon nitride cantilevers of the MLCT model (Bruker SPM Probes, Camarillo, CA, USA) were used for imaging, which was carried out in tapping mode with the triangular shaped F-Lever (nominal values are a resonance frequency of 125 kHz, a spring constant of 0.3 N/m and a nominal tip radius of 20 nm). Before imaging, the cross-linked nanoparticles were adsorbed to a freshly cleaved surface of highly oriented pyrolytic graphite (HOPG) which has a typical root mean square surface roughness of 0.1 nm over an area of 1 μm^2 [263]. The surface used in this work featured a thickness dispersion of ± 0.2 mm (NT-MDT Service and Logistics Ltd., Limerick/Ireland). The particle solution (30 - 100 µL) was adsorbed for 10-15 min at RT and imaged in the fluid drop or in a fluid cell that was subsequently filled with H_2O_{dd} (2 mL). The image analysis comprised the evaluation of particles with spherical shape in the x-y-plane that featured a height more than 4 nm. These particles were analyzed via their section line of which the height was measured. To define the particle diameter, each cross section was fitted with a Gaussian fit from which the full width half maximum (FWHM) was evaluated. The value was corrected for the effect of tip radius, which was approximated to 10 nm (the nominal 20 nm radius given by the manufacturer appeared to overestimate tip dimensions). Image analysis was conducted with the Igor Pro Software, Version 6.1.2.1 from WaveMetrics (OR, USA).

3.2.6.4. Transmission electron microscopy (TEM)

Samples were prepared for TEM measurements via negative staining at RT. A solution of cross-linked nanoparticles (5 µL with approximately 0.4 mg/mL protein) was applied on glow-discharged carbon-coated grids and incubated for 2 min. The excess solution was blotted off with filter paper (Whatman grade 1) after which the sample was rapidly transferred to a drop of ammonium molybdate stain solution (5 µL, 2% (w/v), pH 7.0). It was observed that sample quality was better the faster the transfer was carried out. Samples were incubated for 1.5 min. Afterwards, excess solution was blotted off and samples were left to air-dry.

Measurements were carried out with a JEOL JEM 100CX microscope at 100 kV. Micrographs were taken on Kodak SO-163 electron image films and featured a nominal magnification of 20,000x with a slight negative defocus. The images, digitized with a FlexTight Precision II array scanner (Hasselblad), featured a calibrated pixel size of 7.9 Å at the sample level. Analysis was carried out with ImageJ (version 1.44e) where a median filter with a 2 pixels radius was applied to the image. Particle sizes were manually approximated with a circle, from which the diameter was determined.

3.2.7. Statistical analysis

Statistical analysis was carried out with the RStudio Software from RStudio Inc. (Boston, MA, USA). For analysis, the mean particle sizes from DLS measurements were used from samples featuring a Gaussian size distribution of the particle population. When minor aggregates were observable in the intensity-weighted plot but were absent in the number-weighted plot, the sample quality was classified as sufficient for analysis and used in the statistical test. Statistical significance of size differences was assessed by the analysis of variance (ANOVA) analysis. Primarily, requirements for this analysis were tested which included the Levene test for homogeneity of variances and Shapiro Wilk test for normality. A p-value of < 0.05 indicated the applicability of the Tukey test. The results of the Tukey test are given in the box plot where the corresponding levels of significance are as follows:

0-0.001: *** / 0.001-0.01: ** / 0.01-0.05: *

3.2.8. Labeling nanoparticles

Fluorescent labeling was carried out in two different ways: By marking the individual trimers before micelle formation and cross-link or by labeling the cross-linked nanoparticles. Both labeling procedures were carried out by using NHS chemistry as shown in Reaction Scheme 2. The labeling reaction was carried out in standard buffer to provide good reaction conditions for a modification of the N-terminus, which has a reported pK_a value of approximately 7.6-8 [244]. The N-termini of the trimers were located in the particle interior and lysines were present in the foldon headgroup.

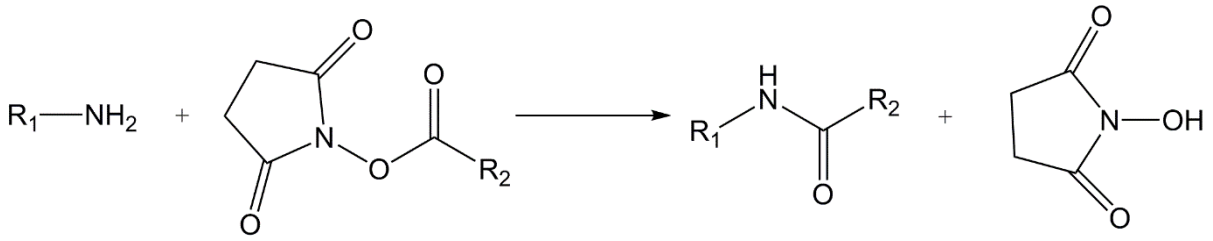

Reaction Scheme 2: Modification of amine group with NHS-ester containing molecule by formation of an amide bond, based on reaction from reference [230].

The labeling degree was determined according to formula 3.6 [272]:

$$DOL = \frac{A_{max}/\varepsilon_{max}}{A_{prot}/\varepsilon_{prot}} = \frac{A_{max} \cdot \varepsilon_{prot}}{(A_{280} - A_{max} \cdot CF_{280}) \cdot \varepsilon_{max}} \qquad (3.6)$$

With the absorption maxima A_{max} and A_{prot}, the extinction coefficients for the dye and protein ε_{max} and ε_{prot} and the correction factor CF_{280}. Values for DyLight™ 594 were $\varepsilon_{max} = 80.000\ M^{1}cm^{-1}$ and $CF_{280} = 0.585$. Values for Atto647N-NHS were $\varepsilon_{max} = 150.000\ M^{1}cm^{-1}$ and $CF_{280} = 0.03$.

Trimer-labeling with DyLight™ 594-NHS

Trimer labeling was carried out with the dye DyLight™ 594 (Thermo Fisher Scientific) which was freshly dissolved in DMSO before use. The dye solution was added to 73 µM protein in

standard buffer, leading to a final dye concentration of 18 µM. The reaction mixture was incubated rotating at RT for 2 h. This was followed by dialysis at RT against 1.5 L standard buffer with Pur-A-Lyzer Maxi dialysis devices (12 kDa MWCO, Sigma-Aldrich) for approximately 6 h, including one buffer exchange. For micelle formation and cross-link, the labeled trimers were mixed with unlabeled trimers in a 1:7 (v/v) ratio. The DOL was defined to 22 %.

Nanoparticle-labeling with Atto647N-NHS

Cross-linked nanoparticles were dialyzed against standard buffer, as described in 3.2.5 and subsequently labeled. The dye Atto647N-NHS (ATTO-TEC, Siegen, Germany) was freshly dissolved in DMSO and the labeling reaction was initiated by the addition of the dye to the particle solution in a 1:10 (v/v) ratio. The final dye concentration of the labeling solution was defined and the solution was incubated shaking at RT for the time indicated. As dialysis was carried out above T_t (at 43 °C) the reaction vessels with the nanoparticle solution and the dialysis devices with standard buffer were equilibrated above T_t before dialysis. As devices, Slide-A-Lyzer MINI dialysis devices (Thermo Scientific GmbH) were used which had a cutoff membrane of 20 kDa. Dialysis was carried out above T_t at 70 rpm for the time indicated. The samples were used in FCS measurements and cartilage studies. Small alterations in the labeling procedure for different FCS experiments were as follows:

Experiment 1: The labeling solution had a final dye concentration of 50 µM and was incubated on a shaker at RT for 1:20 h. The samples were consecutively equilibrated above T_t (43 °C) for 1 h. Dialysis against standard buffer was carried out in an incubator for 1 h at 43 °C, 50 rpm after which the dialysis buffer was exchanged. Samples were further dialyzed o/n at 43 °C at 90 rpm. The DOL of the sample to be used in FCS measurement was defined to 8.4 %. Labeling was carried out two days after cross-link, measurement was performed ten days after cross-link.

Experiment 2: The dye was added to the nanoparticle solution in a 1:9 (v/v) ratio. The solution had a final dye concentration of 13 µM and was incubated at RT for 2:15 h. The reaction vessels with the nanoparticle solution and the dialysis devices with standard buffer were equilibrated 3:40 h above T_t before dialysis. Dialysis was carried out over the weekend above T_t at 50 rpm. The DOL was defined to 4 %. Labeling was carried out two days after cross-link, measurement was performed 15 days after cross-link.

Experiment 3: The solution had a final dye concentration of 12 µM and was incubated at RT for 40 min. The reaction vessels with the nanoparticle solution and the dialysis devices with standard buffer were equilibrated 15 min above T_t before dialysis. Dialysis was carried out above T_t for 4 days at 70 rpm while the dialysis solution was exchanged several times. The DOL was defined to 5 %. Labeling was carried out two days after cross-link, measurement was performed eight days after cross-link.

Experiment 4: The solution had a final dye concentration of 14 µM and was incubated at RT for 40 min. The reaction vessels with the nanoparticle solution and the dialysis devices with standard buffer were equilibrated 15 min above T_t before dialysis. Dialysis was carried out above T_t for one day and twice o/n at 70 rpm while the dialysis solution was exchanged several

times. The DOL was defined to 6 %. Labeling was carried out nine days after cross-link, measurement was performed 32 days after cross-link.

3.2.9. Loading nanoparticles

3.2.9.1. FITC-dextrans

For DLS measurements, a stock solution of neutral fluorescein isothiocyanate (FITC)-labeled dextrans was prepared (2 mM in standard buffer) and diluted in H_2O_{dd} leading to a second stock of FITC-labeled dextrans with 0.2 mM concentration. ELP solutions (18-19 µM, without fluorescence label) were spiked with the two solutions in a 1:9 (v/v) ratio. An additional volume of a NaCl stock solution was added (1 M, 10 µL) to one sample. The added solutes were included in the dispersant specifications at the respective concentrations.

For preparation of nanoparticles for colocalization experiments, neutral FITC-labeled dextrans with a MW of 4 kDa (Sigma Aldrich) were added to the protein solution before cross-link to facilitate their incorporation into micelles. A stock of FITC-labeled dextrans (2 mM in standard buffer) was added to the protein solution, leading to a final dye concentration of 129 and 131 µM respectively. For micelle formation and cross-link, the labeled trimers were mixed with unlabeled trimers in a 1:7 (v/v) ratio. Particle sizes were increased by spiking the solution with NaCl (1M) before cross-link to facilitate imaging by confocal microscopy (Leica Type TCS SPS II, Leica Microsystems CMS GmbH). Protein solutions (11 µM) in phosphate buffer (1.5 mM) had final salt concentrations of 16 mM and 32 mM NaCl respectively. Solutions were dialyzed o/n against standard buffer with Pur-A-Lyzer Maxi dialysis devices (12 kDa MWCO, Sigma-Aldrich) in order to remove excess FITC-labeled dextrans. The laser wavelengths for dye excitation were 488 nm for the FITC-dextrans and 633 nm for the DL594-labeled particles. Emission was detected in the range of 500-550 nm and 653-695 nm.

3.2.9.2. Cryptophane cage A

Cryptophane cages [273] are hydrophobic macromolecules used in Xenon-based NMR measurements [274]. Xenon gas atoms are characterized by their high affinity to hydrophobic regions and the high sensitivity of their chemical shift to the local environment [275]. The specific chemical shift signature makes Xenon an attractive molecule as a biosensor [275]. It distributes well into tissues which can be analyzed by a specific chemical shift [276]. Sensitivity of Xenon-based NMR measurements can be greatly increased by optical pumping and subsequent polarization transfer to Xenon, reviewed in [277]. Hyperpolarized ^{129}Xe NMR measurements have been used to study the temperature-driven swelling of PNIPAm-based hydrogels [278].

The incorporation of Xenon gas atoms into a hydrophobic molecule can significantly increase detection sensitivity [279]. Xenon atoms encapsulated in cryptophane cages are stabilized via London forces in the molecular cage and show a shift in resonance frequency of about 160 ppm, compared to dissolved Xenon [274]. It has been shown that the acetic acid derivative of the cryptophane cage Carboxy-Cryptophane-A (CrA-COOH) can also encapsulate Xenon gas atoms in its interior [275]. CrA-COOH is a water-soluble cryptophane cage that contain one acid group as indicated in Figure 9.

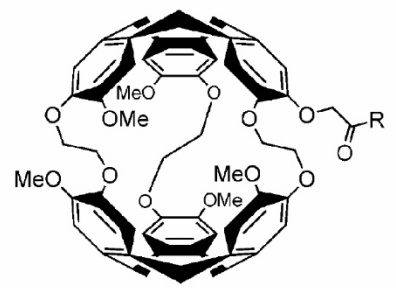

Figure 9: Molecular structure of Carboxy-Cryptophane A with R = OH. The macromolecule was provided via the group of Prof. L. Schröder, synthesized by Kang Zhao, Tianjin University, China. Reprinted with permission from Sloniec et al., 2013, Chem. Eur. J. 19, 3110-3118, Copyright © 2013 John Wiley and Sons [280]

It was shown that derivatives of the cryptophane cage were able to locate into vesicle membrane structures [280]. Likewise, the entrapment of the hydrophobic carrier system into a protein-based carrier on the nanoscale may further increase the range of potential applications in magnetic resonance imaging. It is assumed that the encapsulation of such molecular cages into carrier system may increase the applicable concentration and may have effects on its biocompatibility. Furthermore, the presence of a hydrophobic molecule might support hydrophobic association of micelle formation. This may also have an effect on T_t, which may be reduced to lower values.

Here, it was tested in DLS experiments if the presence of CrA-COOH has an effect on micelle formation or nanoparticle solution stability. In two experiments, CrA-COOH was added to the ELP solution before cross-link. For this, CrA-COOH was dissolved in DMSO and diluted 1:10 (v/v) in H_2O_{dd}, giving the stock solution of CrA (88µM). The stock was added to the ELP solution to obtain a concentration of 30 µM. In one experiment it was tested whether the addition of CrA-COOH to cross-linked particles did affect particle stability. For this, the solution was spiked with cryptophane cage dissolved in DMSO (2.5 mM) leading to an end concentration of 49 µM CrA-COOH in the nanoparticle solution. The switching in size was verified via a DLS heating cycle.

4. Results and Discussion

4.1. Geometrical considerations

This chapter gives a theoretical estimation of the sizes of the trimers as particle building blocks, the cross-linker and the nanoparticle size. It concludes with an estimation of the temperature-induced nanoparticle size change.

4.1.1. The hydrophobic domain: The ELP sequence

A molecule can be described as a succession of *N* segments featuring a characteristic Kuhn length l_{Kuhn}. Under assumption of an ideal chain configuration where the individual orientations are uncorrelated, the contour length l_c of the unfolded monomer can be approximated by [281]:

$$l_c = n \cdot l_{Kuhn} \tag{4.1}$$

The ELP sequence has been given in section 1.3. With the number of *n* amino acids as (5·58+5) and the average Kuhn length l_{Kuhn} of an amino acid as 0.363 nm [282], the l_c of an unfolded ELP chain results to 107 nm. In analogy to Ghoorchian et al. [37], an approximation of the folded construct with 20 % of the unfolded contour length results in a length of 21 nm for a folded trimer. The radius of gyration R_g for an ideal linear polymer is related to the mean-square end-to-end distance $\langle R^2 \rangle$ by the following expression [162, 281]:

$$R_g = \sqrt{\frac{\langle R^2 \rangle}{6}} = l_{Kuhn}\sqrt{\frac{n}{6}} \tag{4.2}$$

The Flory approximation for real chains includes the effect of the solvent characteristics on the polymer size [281]. It includes a scaling exponent *v* for the number of monomers *n*, which depends on the solvent qualities for the respective polymer [281]. For ideal polymers, the exponent is 1/2, while for real chains in good solvents an exponent of 3/5 was approximated [281]. Assuming an exponent *v* of 3/5 of a swollen linear polymer in a good solvent [281] and an average amino acid length of 0.363 nm [282], the R_g of an ELP trimer below T_t can be defined to a value of 8.7 nm. In this work, the molecular sizes are to a large part determined by DLS which defines the hydrodynamic radius R_h of a molecule in solution [246]. For a molecule in a random coil conformation, the radii are related by R_g/R_h= 1.51 [162]. This gives a R_h of 5.8 nm and a hydrodynamic diameter of 11.6 nm for an unfolded trimer. These values assume the polymer to be in a random coil conformation. For ideal polymers in an *f*-arm star configuration, the mean radius of gyration has been given by [281]:

$$R_g = \sqrt{\left[\left(\frac{N}{f}\right)\frac{l_{bond}^2}{6}\right]\left(3 - \frac{2}{f}\right)} \tag{4.3}$$

For a polymer composed of *f* arms where each arm is composed of *N/f* monomers of Kuhn length l_{Kuhn}. For the ELP construct composed of three arms of 885 amino acids in total with an

l_{bond} of 0.363 nm [282], one obtains an R_g of 6.5 nm and an R_h of 4.3 nm. These estimations give valuable information for comparison with DLS-derived values for free trimers in solution.

4.1.2. The cross-linker: Bismaleinimide poly(ethylene glycol)

The cross-linker for the covalent stabilization of the nanoparticles had a MW of 1983 g/mol. The functional group maleinimide and one PEG entity have a MW of 97 g/mol and 44 g/mol respectively which implies a MW of 1789 g/mol of the PEG sequence without functional groups:

$$MW_{PEG} = 1983\ g/mol - 2 \cdot 97\ g/mol = 1789\ g/mol \tag{4.4}$$

This leads to the number of PEG units n_{PEG} as follows:

$$n_{PEG} = \frac{1789\ g/mol}{44\ g/mol} = 40.65 \approx 41\ units \tag{4.5}$$

The mean-square end-to-end distance $\langle R^2 \rangle$ can be calculated by the number of segments N of Kuhn length l_{Kuhn} [281]:

$$\langle R^2 \rangle = l_{Kuhn}^2 N \tag{4.6}$$

With an approximation for PEG molecules that l_{Kuhn} is around twice the monomer length [283], one may employ formula 4.1 for calculation of contour length, by using a number of 41 segments with a specific monomer bond length. Under consideration of fractional helix formation in water, by using a bond length of 2.8 Å for a helical and 3.58 Å for a planar configuration of PEG [283], one obtains a L_c of 11.5 nm or 14.6 nm respectively. This implies that upon stretching, the PEG chain contour length can increase by 22 %, if stretching of bonds is neglected.

With approximately 20 segments of Kuhn length l_{Kuhn} of 7 Å [283], this gives an end-to-end distance $\langle R \rangle$ of 3.1 nm. The radius of gyration R_g can be calculated by formula 4.2, assuming a good solvent with ν = 3/5. This leads to a value of R_g = 1.7 nm and a R_h = 1.1 nm for a single PEG linker with a MW of 2 kDa. It has to be noted that PEG was reported to be in a random coil formation with a fraction of helical regions where the helicality increased with the number of subunits, thereby rendering the overall surface more hydrophobic [284].

4.1.3. The cross-linked nanoparticle

The calculations based on protein density and occupied volumes are from the geometrical considerations in the Supplement of Kracke et al. (2015) Macromolecules 48,5868-5877 [125].

The occupied volume V_{trimer} of a single trimer can be calculated with an approximation of the protein density ρ = 1.2 kg/l, analog to the reported density of elastin [285]. The calculation includes the assumption that the ELP-based nanoparticle above its T_t contains the same volume percentage of protein as typical ELP coacervates, with 37 % protein [174]. This leads to the occupied volume of one trimer in the coacervate form V_{trimer}:

$$V_{trimer} = \frac{MW_{trimer}}{\rho \cdot N_A} = \frac{83435.1\ \frac{g}{mol} \cdot \frac{100}{37}}{1.2 \cdot 10^3 \frac{g}{l} \cdot 6.022 \cdot 10^{23} \frac{1}{mol}} = 11.55 \cdot 10^{-23} l = 312\ nm^3 \quad (4.7)$$

When analyzing a micelle with a radius of 14.5 nm, the resulting particle volume is

$$V_{micelle} = \frac{4}{3}\pi r^3 = \frac{4}{3}\pi(14.5\ nm)^3 = 12770\ nm^3 \quad (4.8)$$

From this, one can obtain the packing density which is termed the "aggregation number" *N*.

$$N = \frac{trimers}{micelle} = \frac{V_{micelle}}{V_{trimer}} = \frac{12770\ nm^3}{312\ nm^3} = 41\ \frac{trimers}{micelle} \quad (4.9)$$

The aggregation number of the used construct is estimated to be 41 trimers per micelle. As introduced in section 2.2, geometrical dimensions of particles can be estimated with the dimensionless packing factor which is determined by the relation of the hydrophobic chain volume *v* to its length *l* and the optimal headgroup area a_0 [222, 223]. For a packing into spherical micelles the following relation holds [223]:

$$\frac{v}{a_0 l} = \frac{1}{3} \quad (4.10)$$

The packing into small micelles is limited by the maximum feasible length of the hydrophobic chains [221, 223] and the occupied surface area of the headgroup which can adopt an optimal value a_0 [223]. It was further defined that micelles form when the hydrocarbon chain is around the double value of the headgroup diameter [222].

The transition of the ELP into a collapsed polymer of specific length fulfills the above requirements and thus facilitates a packing into micelles. The effective headgroup area a_0 of the ELP fusion protein in a micellar assembly with diameter *d* results to:

$$a_0 = \frac{6v}{d} = \frac{6 \cdot 312\ nm^3}{2 \cdot 14.5\ nm} = 65\ nm^2 \quad (4.11)$$

Hereby, the critical length of the hydrophobic chain in the micelle ($r_{micelle}$) is not exceeding the calculated contour length l_c of 21 nm of a folded trimer which facilitates micelle formation. It appears that trimers in micellar assemblies are even more compact since the measured micelle radius is typically smaller than the calculated value of l_c. A micelle with a radius of 14.5 nm, a total area of 2642 nm² and trimers with an optimal headgroup area of 65 nm², feature a packing density 41 trimers per micelle. The corresponding effective headgroup diameter is 9 nm. This is in accordance with the headgroup diameters for the fusion construct used by Ghoorchian et al. [37]. The theoretically defined value for the contour length with 21 nm for a folded trimer would lead to a micelle diameter of around 42 nm. This is larger than the observed diameter of 29 ± 6 nm reported in 4.2.2. The difference might be ascribed to a slightly increased compactness of the micelles.

The value of the headgroup area matches the value for single chain fatty acids as dodecyl chains which have been reported to be 60 to 65 Å in micellar assemblies [221]. Thus, the geometry of a folded trimeric ELP fusion protein resembles the geometry of a single chain lipid. The apparent

headgroup area decreases with increasing salt concentrations via electrostatic shielding [37] and thus reduced electrostatic repulsion.

4.1.4. Estimation of temperature-triggered size change

Based on the contour length of the ELP and the decrease in chain length upon the phase transition, the extent of diameter change of a cross-linked nanoparticle can be approximated. A theoretical estimation of the diameter of a completely swollen micelle can be obtained with twice the unfolded contour length [37]. For the used construct this is 107 nm which leads to a diameter of 214 nm for a swollen nanoparticle. Such a particle would need to be stabilized via the N-termini located in the particle interior. As the particles are stabilized at 1/3 of the ELP sequence away from the particle surface, this leads to a partly unfolded chain with a contour length of 36 nm for each construct. A nanoparticle stabilized as such would have a diameter $d_{swollen}$ below its T_t as follows:

$$d_{swollen} = 2 \cdot \left(l_{c,f} \cdot \frac{2}{3} + l_{c,uf} \cdot \frac{1}{3} \right) = 2 \cdot \left(21\ nm \cdot \frac{2}{3} + 107\ nm \cdot \frac{1}{3} \right) = 99\ nm \qquad (4.12)$$

With a folded contour length of $l_{c,f}$ of 21 nm and the unfolded contour length $l_{c,uf}$ of 107 nm, one obtains a micelle diameter of 99 nm below T_t and with 42 nm above T_t. Comparatively, with the use of the DLS-derived micelle radius of 15 nm before cross-link, instead of $l_{c,f}$, the obtained value for a swollen particle is slightly smaller, with 91 nm below its T_t. Both values overestimate the particle dimensions below T_t, as will be seen in 4.3.1. This might be due to an increased compactness of the micelles, as mentioned above.

As the covalent cross-links are located in the particle interior at a distance of approximately 1/3 of the chain length N-terminal to the foldon, one can estimate the theoretical inner particle surface with:

$$A_{micelle} = 2\pi \left(\frac{2}{3} \cdot R_h \right)^2 = 2\pi \left(\frac{2}{3} \cdot 30\ nm \right)^2 = 1676\ nm^2 \qquad (4.13)$$

Where the experimentally defined radius R_h of approximately 30 nm after cross-link below T_t is used for calculation. Assuming a nanoparticle with 41 trimers, this leads to an approximate occupied area for an individual trimeric ELP strand of 41 nm² in the particle interior. By considering the individual chains being in motion and adding the linker sequences with a R_g of 2.7 nm and a total l_c of 28.7 nm, this gives an idea of the conditions in the particle interior.

4.2. Nanoparticle synthesis

This chapter reports on trimer characterization via SDS-PAGE after purification, followed by DLS measurements of micelle formation. The last part defines the conditions to obtain cross-linked ELP nanoparticles.

4.2.1. Expression and purification of ELPs

Recursive directional ligation and ligation into the expression vector was carried out by the cooperation partner, the group of Prof. Dr. N. B. Holland at the Chemical and Biomedical Engineering Department at Cleveland State University, Ohio, US. The chapter is based on the publication of the author: Kracke et al. (2015) Macromolecules 48,5868-5877 [125].

The trimeric ELP $(GVGVP)_{36}(GCGVP)(GVGVP)_{21}$-foldon was successfully expressed and subsequently purified via the ITC method [65, 66]. This yielded a clean protein solution which was evidenced by SDS-PAGE. For this, the final protein stock solution was diluted in standard buffer and mixed with Laemmli buffer (250 mM DTT, 7.1 % (w/v) SDS) in a 1:1 (v/v) ratio. The DTT was added to reduce potential disulfide bridges between individual ELP chains and the SDS was added to induce denaturation and disassembly of the trimers. The results are illustrated in Figure 10. One sample was heated 5 min at 95 °C prior to loading on the gel (lane 1) while the second sample was loaded directly without heating (lane 2). As protein marker served Kaleidoscope Precision Plus (BioRad).

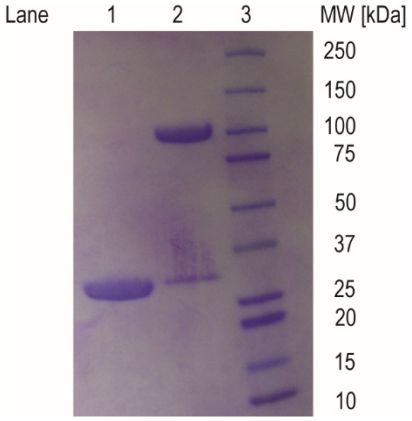

Figure 10: SDS-PAGE showing highly purified ELP $(GVGVP)_{36}(GCGVP)(GVGVP)_{21}$-foldon. Lane 1 contains a sample that was heated for 5 minutes at 95 °C prior to loading on the gel and is thus in the monomeric form. The unheated sample in lane 2 shows the trimeric construct. Protein marker Kaleidoscope Precision Plus (BioRad) was loaded in lane 3. Reprinted with permission from B. Kracke et al., 2015, Macromolecules 48, 5868-5877, Copyright © 2015 American Chemical Society [125].

As heating at 95 °C causes thermal denaturation of the foldon domain [137], lane 2 shows monomeric ELP sequences. The monomers with a MW of 27,812 Dalton (Da) can be seen in lane 1. The unheated sample with the intact trimeric constructs can be seen in lane 2. It is observable that the expected signal at 83,435 Da is slightly shifted to higher values. It could be that the non-denatured headgroup is associated with less SDS molecules than it would theoretically be in the denatured state, leading to a diminished migration through the gel. A minor fraction in lane 2 is present in monomeric form, which could be the result of partial denaturation by SDS in the sample buffer. It can be seen that the SDS did not induce complete denaturation of the construct at the used concentrations.

4.2.2. Particle formation

Parts of this chapter are based on the publication of the author: Kracke et al. (2015) Macromolecules 48,5868-5877 [125].

The protein stock solution was diluted in H_2O_{dd} to obtain a low concentrated phosphate buffer (< 1 mM) which lacked NaCl and had a pH between 9.6-10.5. The basic pH was needed for deprotonation of the N-termini in the particle interior, where the absence of charges facilitated micelle assembly [286]. Protein concentration was set to 20 µM. The size measurement was carried out in form of a thermal cycling measurement where sizes below and above T_t were measured. Such a formation of micelles with reversibility of the assembly and the absence of a hysteresis behavior had been reported for a similar construct by Ghoorchian et al. [37]. A typical DLS-derived size graph of micelle formation is presented in Figure 11. The trimer population can be seen below T_t with a size distribution of 14 ± 2 nm before heating and 16 ± 2 nm after heating. The presence of larger aggregates can be observed below T_t which disappeared upon the supply of heat. The micelle size of 29 ± 6 nm is slightly larger than the value for $(GVGVP)_{40}$-foldon [37] which is expected, since the current trimeric construct contained 18 additional pentapeptide sequences. Micelle solutions had a very high degree of solution homogeneity, indicated by the low PI value that was typically below 0.1. Solutions with a PI < 0.1 are typically considered monodisperse [252].

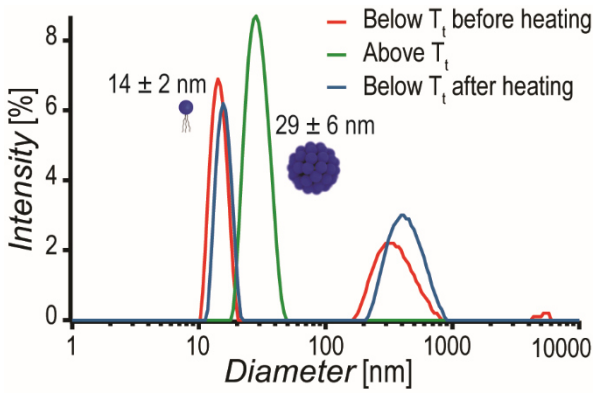

Figure 11: Reversible micelle formation of the ELP fusion protein $(GVGVP)_{36}(GCGVP)(GVGVP)_{21}$-foldon at 20 µM in 0.4 mM phosphate buffer, pH 10.2. Sizes are defined by DLS measurements and shown is the PSD by intensity where sizes are tracked in a temperature cycling measurement. Diameters are 14 ± 2 nm below T_t before heating (red), 29 ± 6 nm above T_t (green) and 16 ± 2 nm below T_t after heating (blue). Reprinted with permission from B. Kracke et al., 2015, Macromolecules 48, 5868-5877, Copyright © 2015 American Chemical Society [125].

The micelle formation of three individual ELP stocks with 20 µM protein concentration in low salt conditions (0.4 mM phosphate buffer, pH 9.6-10.3) is shown in Figure 12. The measurement was conducted in discrete heating steps of 0.2 °C with 5 min equilibration time before each measurement. The transition is marked by a distinct increase in size, accompanied by the decrease in PI and a considerable increase in the derived count rate (DCR). The data shows the sizes of the main populations with trimer sizes as 13 ± 1 nm and 15 ± 1 nm respectively and nanoparticles with diameters smaller than 50 nm. The sizes represent the mean diameter from intensity-weighted DLS size graphs.

Previous studies typically determined the T_t of ELPs via turbidity assays where it was defined as the midpoint between the baseline and the maximum of the absorbance curve at 300 nm [169].

In the DLS analysis shown here, the T_t was defined in an analogous way via the size tracking: The value of T_t was determined as the turning point of the sigmoid fit on the size transition plot. This provided a mean T_t of 36.6 ± 0.5 °C for the presented protein solution (20µM). The onset of micelle assembly was at around 35 °C. It was accompanied by a decrease in PI, as can be seen in Figure 12 b), illustrating an increase in solution homogeneity. As was also observable in Figure 11, a second larger side population was present in solution below T_t. This was also observed for the solutions presented in Figure 12 and Figure 13 but were left out for clarity. Above the T_t, the side population was sometimes observed in intensity-weighted graphs but represented a minor fraction that was present in the number-weighted graphs only on very rare occasions (see Appendix 7.4 for all size populations from intensity-weighted graph).

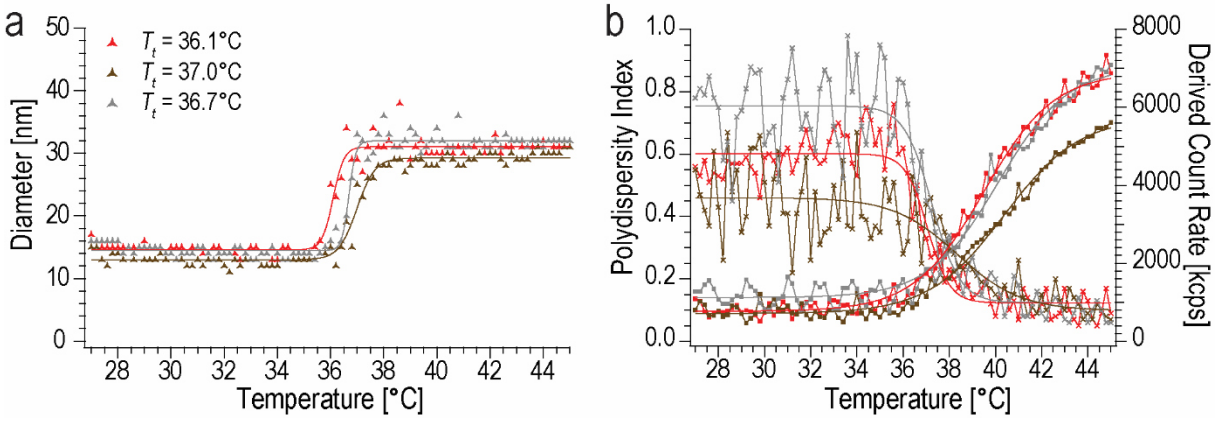

Figure 12: Definition of T_t of micelle formation with 20 µM ELP fusion protein in low salt (0.4 mM phosphate buffer, pH 9.6-10.3) in DLS-derived temperature trends. Sizes were tracked in discrete temperature steps (0.2 °C) in the temperature range 27-45 °C. **(a)** Sizes are the mean values derived from the peak analysis of the intensity-weighted size distribution and T_t was defined as the turning point of the sigmoidal fit. Reprinted with permission from B. Kracke et al., 2015, Macromolecules 48, 5868-5877, Copyright © 2015 American Chemical Society [125]. **(b)** Tracking of DLS-derived polydispersity index and derived count rate during micelle formation.

It can be seen that there is a considerable increase in scattering upon the clustering of scattering centers. This can be seen by the increase in DCR which is illustrating an increase in scattering intensity upon the phase transition. It evolves along with the size increase, caused by the micelle assembly, whereas its onset is slightly shifted to higher temperature. The DCR increase can be attributed to a modification in the optical properties (the refractive index) of the scattering centers [287]. Here, the micelle may be viewed as a denser sphere of condensed protein with collapsed trimers forming a particle that scatters more light than individual trimers. The formation of a secondary protein structure above T_t, which is assumed to be analogous to the reported structure of ELPs [126], might further increase the scattering intensity. An increase in scattering intensity has also been reported for the temperature-driven aggregation of other ELP constructs which was assigned to changes in conformation [109, 288].

For analysis of the concentration dependence of the T_t, the temperature trend measurements were carried out at 60 µM and 4-5 µM in 2-3 mM and 0.1 mM phosphate buffer respectively. The graphs in Figure 13 show a similar transition behavior with a steep increase in particle size. As expected, the T_t is shifted depending on the protein concentration, with 32.5 ± 0.3 °C for 60 µM and 38.5 ± 0.9 °C for 4-5 µM protein concentration. When comparing Figure 13 a) and c), it is obvious that on average, the transition curve is steeper at higher concentrations which is in analogy to observations in other studies [49, 124]. The deviations in the T_t for the low

concentrated samples which fluctuates up to 2 °C can be explained by the deviations in concentration measurements, where a slight variation in concentration appears to have a larger effect on the T_t than for higher concentrated samples. Moreover, the DCR trend graph is more unstable for samples with low protein concentrations. The high concentration samples appear to be more homogeneous with a lower PI.

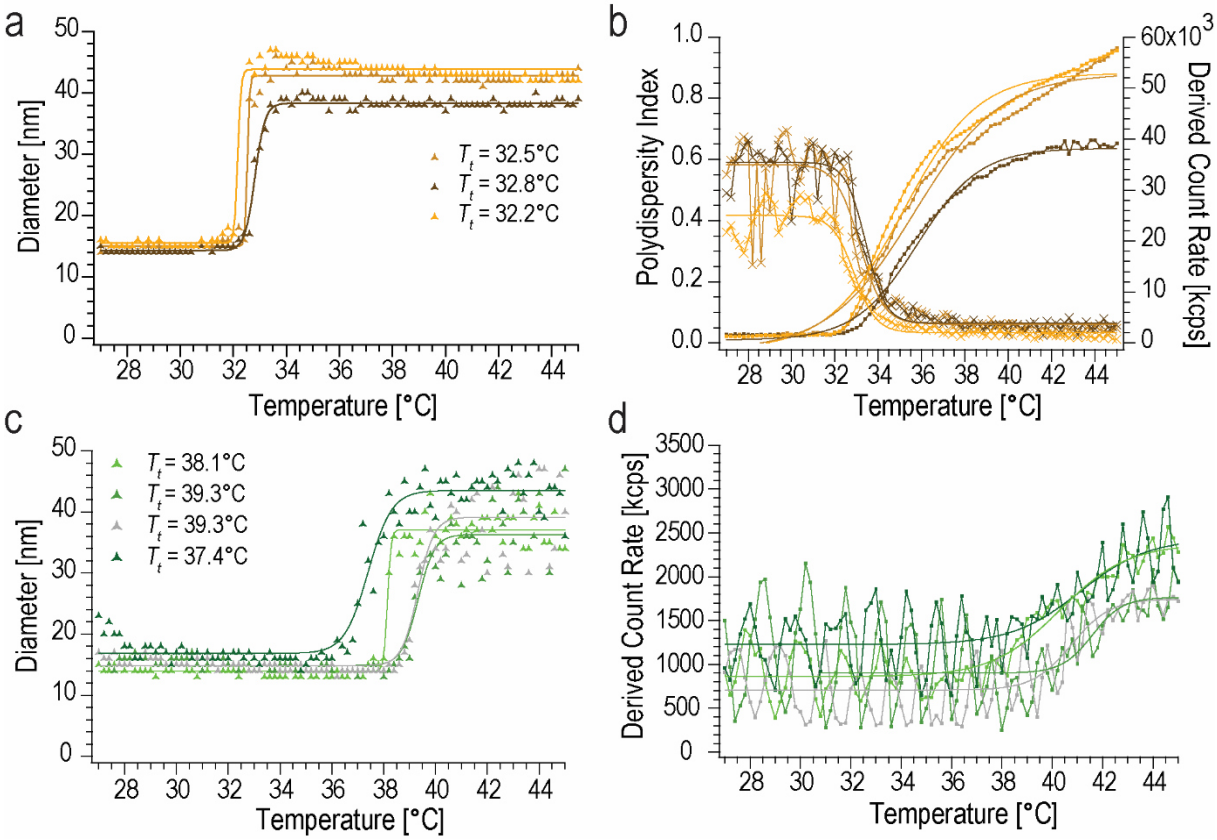

Figure 13: DLS temperature trends for definition of T_t of micelle formation. Sizes were tracked in discrete temperature steps (0.2 °C) in the temperature range 27-45 °C. Concentrations were **(a + b)** 60 µM ELP fusion protein (2-3 mM phosphate buffer, pH 10) and **(c + d)** 4-5 µM ELP fusion protein (0.1-0.3 mM phosphate buffer, pH 10-10.2). **(a)** Mean sizes derived from the peak analysis of the intensity-weighted size distribution with T_t as the turning point of the sigmoidal fit. **(b)** Polydispersity and derived count rate. **(c)** Mean sizes derived from the peak analysis of the intensity-weighted size distribution with T_t as the turning point of the sigmoidal fit. **(d)** Derived count rate. **(a + c)** Reprinted with permission from B. Kracke et al., 2015, Macromolecules 48, 5868-5877, Copyright © 2015 American Chemical Society [125].

In contrast to the plateau of the size measurements at high temperatures, the increase in DCR does not appear to be fully completed at 45 °C, which is especially true for the samples at high concentration. Figure 14 shows temperature trend measurements at three different concentrations in a larger temperature range of 27-55 °C to detect the completion of the DCR increase. It appears that for the high concentrated sample, a second incline in DCR might onset at around 50 °C. This was also seen for other samples (see Appendix 7.4). It might be caused by an additional extrusion of water, which had been observed for other ELPs after prolonged storage at around 80 °C [174]. In the present case, it might also be caused by a loss of total solution volume over the extended measurement time which might have had an effect on the relatively small measurement volumes of 100 µL.

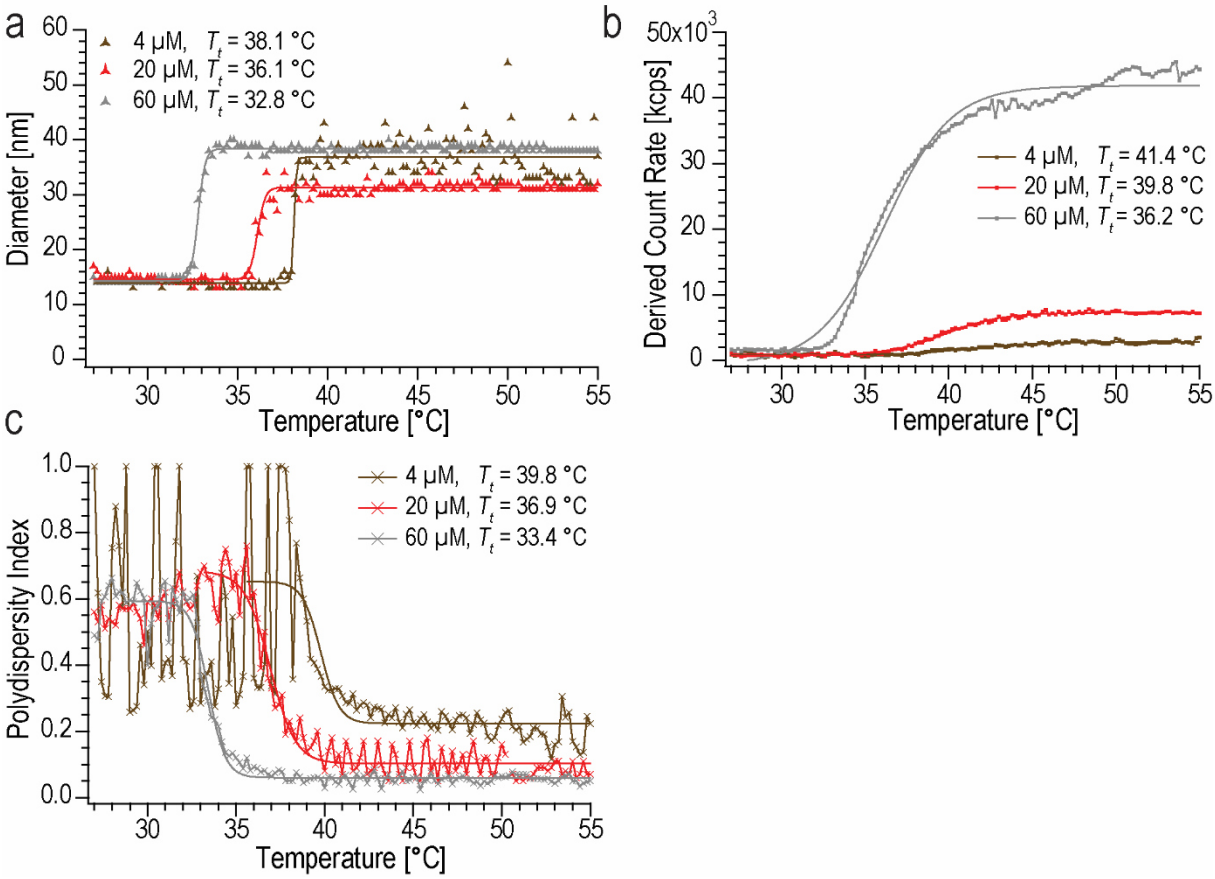

Figure 14: Micelle formation for 4 µM, 20 µM and 60 µM ELP in DLS-derived temperature trends, tracked in discrete temperature steps (0.2 °C) in the range 27-55 °C. **(a)** Mean sizes derived from the peak analysis of the intensity-weighted size distribution with T_t as the turning point of the sigmoidal fit with **(b)** corresponding derived count rate and **(c)** polydispersity index.

The values for the transition points were defined by fitting the graphs of particle size, PI and DCR with sigmoidal fits. The midpoint of each curve was assigned as T_t value. The T_t values are plotted against concentration in Figure 15 a), in order to analyze the concentration dependence of the phase transition. In comparison to the semi-log representation of larger concentration ranges for different constructs [37, 201] the data in the present case can be approximated with a linear fit in a non-log representation at it covers a relatively small concentration range.

It has been reported that the region of the transition can be as narrow as 2 °C [97]. To test if this behavior is true for the used construct, the temperature range ΔT for the transition was plotted in Figure 15 b). It can be seen that the temperature range for the size transition is around 2 °C and appears to be concentration-independent for the concentration range studied. The diminishment of the temperature range for the high concentration samples is only very small. It can further be observed that the transition range of PI values is a bit larger. Thus, establishment of solution homogeneity appears to be a slower process. A pronounced effect is the increased temperature range for the DCR shift, which is even increasing with protein concentration. It has to be noted that these values were taken from measurements between 27 and 45 °C. Taking into account that in some cases the DCR development did not appear to be fully completed for 60 µM samples, the extent might be even higher. However, as the cause for the second DCR transition is not completely solved yet, only the measurement until 45 °C was

included in this analysis. The DCR increase may hint at some structure formation and is seen to follow-up the micelle formation by a small delay.

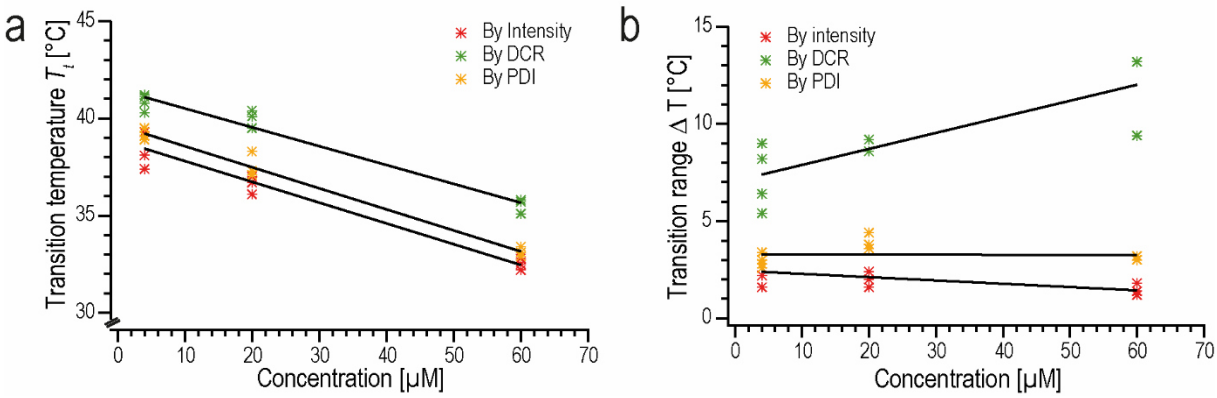

Figure 15: Analysis of concentration dependence of micelle assembly. **(a)** Transition temperature T_t plotted against concentration. **(b)** Transition range ΔT of the transition for size, PI and DCR trends.

The observations are in agreement with the ELP phase transition mechanism proposed by Yamaoka and coworkers [124]. In their study, circular dichroism measurements proved differences in temperature trend progression depending on the wavelength analyzed [VII]. They reasoned from their observation that the process of ELP coacervation may be a two-step process with primary association, followed by secondary structure formation (see chapter 2.1.3). The concentration-dependence of the ELP phase transition (with differences in transition curve steepness) was ascribed to this association process. The decrease in slope steepness with decreasing concentration was also shown elsewhere [289]. Another study classified the ITT as a two-step process composed of dehydration and folding and assembly [171]. All these observations support the conclusions drawn here from DLS temperature trend measurements. The transition appears to proceed via an early coacervation and later maturation step as was noted elsewhere [290].

4.2.3. Cross-link

Cross-linking of ELPs has already been carried out in studies on hydrogels where it was achieved via γ-radiation at different doses [161] with relatively high protein concentrations of approximately 500 mg/mL. Drawbacks of a radiation-induced cross-link is the risk of backbone damage and the lack of chemoselectivity [120]. By comparison, products from glutaraldehyde cross-linking can show cytotoxic effects [291] and the method itself is a rather unspecific one and can lead to different results depending on the age of the glutaraldehyde solution [230]. Furthermore the degree of cross-link is difficult to control, especially when a one-step conjugation protocol is applied [230].

For these reasons, these cross-link approaches were circumvented by the employment of a site-specific reaction. The targets were cysteines in the ELP chain, in order to obtain a stabilized particle with covalent linker sequences in the particle interior. As ELPs are highly sensitive

[VII] The disappearance of the signal characteristic for a random coil formation (at 195 nm) was not concomitant with the development of the β-turn structure (tracked at 210 nm). A concentration dependence for this behavior was speculated but experimental proof for this in particular was not shown.

against salts, buffering conditions had to be optimized to facilitate micelle formation and cross-link without largely affecting particle sizes, which will be discussed in the following section.

As the construct of interest, the monomeric ELP sequence, contained only one cysteine, the method involved cross-link specificity. The sulfhydryl group, with the thiolate ion as particularly reactive species among amino acid side groups, features a pK_a of 8.6 [244]. At a pH value close to this pK_a or above, the thiol holds its highest reactivity [244, 245]. It has been shown that the reactivity of the thiolate form is increased by a factor of $5 \cdot 10^{10}$ in comparison with the protonated form (whereby reactivity is additionally influenced by the direct environment of the reacting amino acid side chain) [245]. Comparatively, cross-link specificity depends on the solution pH and maleinimide groups react specifically with sulfhydryl groups in the pH range 6.5-7.5 [242, 243]. At a pH > 8 in aqueous solution, competing reactions with amine groups can take place [242, 292, 293], shown in the following reaction scheme. The scheme is adapted from Wong and Jameson [244] and shows the reaction of one of the cross-linker's reactive sites.

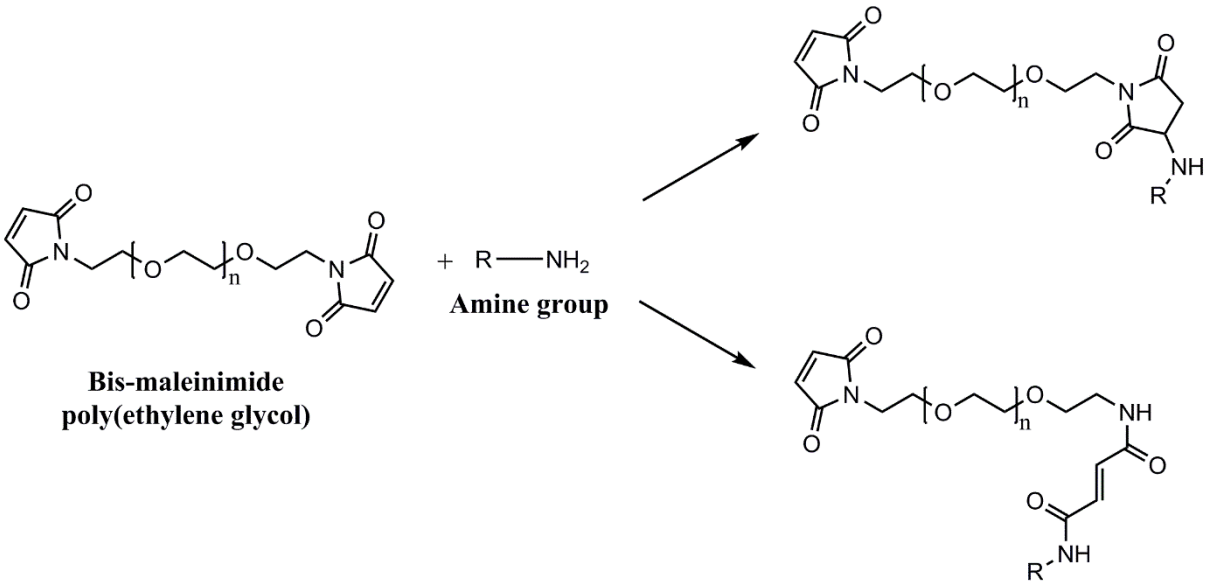

Reaction Scheme 3: Potential side reaction of bis-maleinimide with amine group. The amine can attack the double bond via a Michael reaction or add to the carbonyl group, leading to ring opening. Reaction scheme adapted from reference [244].

It was important that the pH was sufficiently high to guarantee micelles of small size. Given the required basic pH for micelle formation, it cannot be excluded that some minor fraction of the PEG-maleinimides reacts with lysines in the foldon or with the N-termini in the particle interior. These side reactions may be facilitated by high pH and high cross-linker concentration [293]. Controversially, due to the large excess of maleinimides over protein, it is assumed that sufficient cross-linkers are present to form the bonds between the cysteines. A reaction of the N-terminus of the ELP chains would lead to further stabilization of the particle core. As no increased extent of interparticle cross-link was observed, the effect of amine-reactivity of lysines in the headgroup was assigned to be negligible.

A second side reaction that could occur along with the main reaction is hydrolysis, as shown in Reaction Scheme 4. The reaction can be promoted by basic conditions [294, 295, 296]. It leads to the formation of the open form maleamic acid, which can imply a drop in pH. Particle sizes did not appear to be influenced by this and it is assumed that cross-link was effectuated sufficiently fast as cross-link efficiency was proven to be sufficiently high (compare to chapter 4.3.4). It appears

that the large excess of cross-linker over protein is necessary to guarantee high cross-link efficiency in this basic pH range. The pH decreased to value of around 6 to 7. It is assumed that this was a result of the hydrolysis reaction to maleamic acid and the addition of diluted cross-linker solution to the basic ELP solution. Apparently, this did not affect cross-link success but it may be a cause for the slight increase in nanoparticle size upon cross-linking.

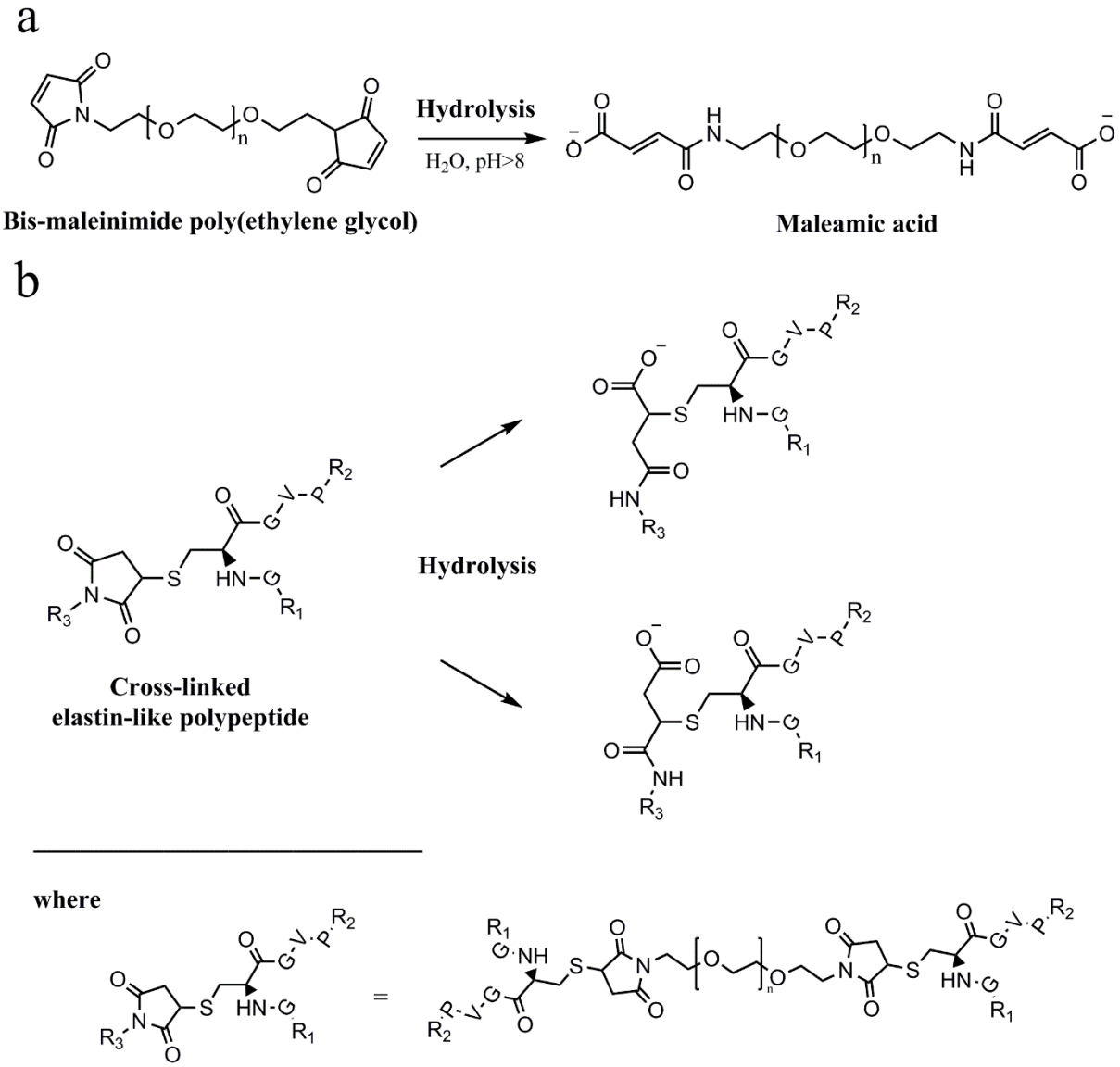

Reaction Scheme 4: Hydrolysis reactions that can occur in maleinimide chemistry for cysteine-modification. **(a)** Hydrolysis of linker before cross-link reaction, leading to maleamic acid. Scheme adapted from reference [244]. **(b)** Ring-opening via hydrolysis of the thioether product after cross-link reaction. Reaction scheme is based on scheme from reference [297].

Ring opening through hydrolysis can also occur for the formed thioether product, as shown in Reaction Scheme 4 b), based on observations from Fontaine et al [297]. The reaction is promoted by the attack of water molecules at one of the carbonyl atoms of the imido group [297]. The rate of hydrolysis is increased at higher pH [230] and hydrolyzed products feature a greater solution stability [297, 298, 299, 300]. The reaction was reported to be facilitated by an electron-withdrawing inductive effect. When the microenvironment is more hydrophobic (without being aromatic), and large steric hindrance by other groups is present, the product undergoes less likely hydrolysis [297]. For the cross-linked nanoparticle in this work, stability would not be affected by

ring-opening as covalent linkages would be preserved. An increased portion of hydrolysis decreases the extent of thiol exchange, which is an unwanted *in vivo* effect of drug conjugates [300, 298, 301]. For the presented nanoparticle system, this effect is assumed to be insignificant since the ELP chain linkages are buried in the particle interior.

It can be speculated that decreasing the cross-linker concentration might improve cross-link quality. Controversially, an interparticle cross-link via maleinimides has been estimated negligible for the presented case. Instead, the side reaction of hydrolysis to maleamic acid appears to be present, as observed by the drop in pH. It is therefore assumed that a lower cross-linker reaction may be applicable. In contrast to this, it may also be considered that the large excess of cross-linker is needed to guarantee a sufficient extent of cysteine cross-links at the basic pH conditions given.

4.3. Nanoparticle size characterization

This chapter reports on the characterization of ELP nanoparticles after cross-link. Temperature-dependent sizes were defined by DLS and FCS measurements and particles were imaged below T_t by AFM and TEM imaging. The chapter concludes with a comparison of the results obtained. The chapter is based on the publication of the author: Kracke et al. (2015) Macromolecules 48,5868-5877 [125].

4.3.1. Thermo-responsive size transition in DLS

Particle switching was monitored via DLS measurements after each cross-link. A typical intensity-weighted size graph is shown in Figure 16 a) where the thermally induced size changes are visible, with (137 ± 27) nm below T_t before heating (red), (83 ± 10) nm above T_t (green) and (133 ± 25) nm below T_t after heating (blue). The observed PI in the range of 0.03-0.04 on the first day after cross-link demonstrates the high homogeneity of the solution. Particle swelling and collapsing was consistent throughout different batches of cross-link, where samples before dialysis showed a diameter decrease of about (39 ± 3) % upon heating above T_t. This corresponds to an approximate volumetric difference of (77 ± 3) %, relative to the volume at low temperature.

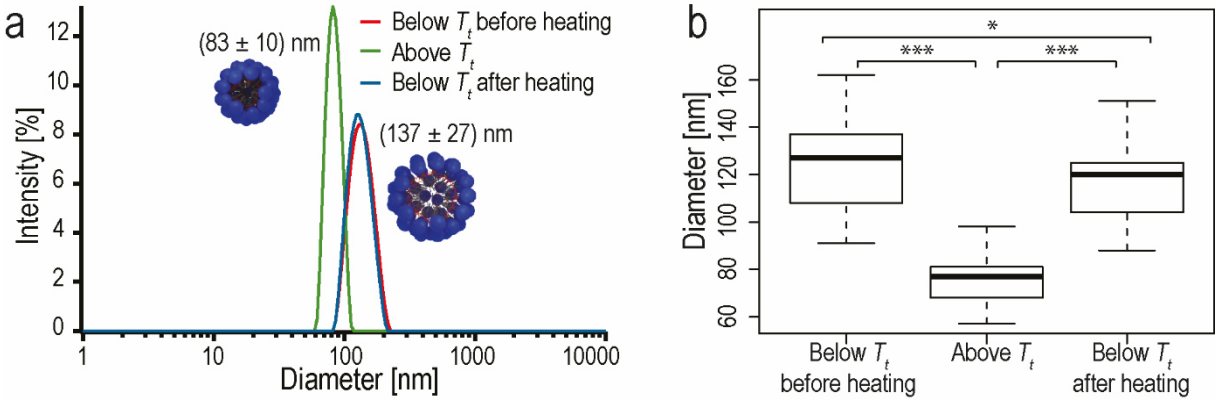

Figure 16: Temperature-dependent sizes of cross-linked nanoparticles, determined via DLS measurements. **(a)** Thermal cycling of cross-linked nanoparticles in DLS measurements, showing distinct temperature-induced size transitions without hysteresis. Particle sizes are represented as intensity-weighted distributions and show particles on the first day after cross-link before dialysis. Diameters are (137 ± 27) nm below T_t before heating (red), (83 ± 10) nm above T_t (green) and (133 ± 25) nm below T_t after heating (blue). **(b)** Boxplot showing nanoparticle sizes derived from intensity-weighted DLS thermal cycling measurement before dialysis. The statistical analysis was conducted with 49 samples from 9 experiments, where a sample corresponds either to a single cross-link or a pool of 2-4 cross-link samples. Mean sizes were (123 ± 16) nm below T_t before heating, (75 ± 10) nm above T_t and (116 ± 14) nm below T_t after heating. **(a + b)** Reprinted with permission from B. Kracke et al., 2015, Macromolecules 48, 5868-5877, Copyright © 2015 American Chemical Society [125].

Statistical significance of size differences between particles below and above T_t was verified via ANOVA analysis, followed by a posthoc Tukey test. The test was conducted for samples before dialysis. For this, 49 samples from 9 experiments were involved, whereby one sample corresponded to either a single cross-link sample or a pool from 2-4 cross-links that were combined for subsequent dialysis. For the presented case of non-dialyzed samples, Levene test for homogeneity of variances had a p-value of 0.02 which is smaller than the required $p < 0.05$. This difference in the distributions below T_t is most likely an effect of heating, which is assumed to render the particle more defined. Normality of the three groups was confirmed with the

Shapiro Wilk test and the results of the succeeding Tukey test can be seen in Figure 16 b). It proves significant difference of particle sizes below and above T_t. Mean sizes observed were (123 ± 16) nm below T_t before heating, (75 ± 10) nm above T_t and (116 ± 14) nm below T_t after heating. It can be observed that overall sizes were slightly larger than expected, as a micelle diameter before cross-link was shown to be around (29 ± 6) nm. This discrepancy is most likely caused by leftover reactants in the solution that were not specified in the solution conditions but influenced the solution viscosity and thus the derived diameters.

Leftover reactants were removed via dialysis and Figure 17 a) shows three representative samples in standard buffer, measured in DLS thermal cycling after storage above T_t. It can be seen that values for particles above T_t are still slightly increased, compared to non-cross-linked nanoparticles. As the proteins are highly sensitive to solution conditions, this behavior is not necessarily unexpected. This minor increase might have been caused by the incorporation of an appreciable amount of cross-linker or by a drop in solution pH upon the cross-link reaction. Statistical analysis was carried out for samples after buffer exchange with mean sizes from intensity-weighted DLS graphs from thermal cycling measurements. The statistical analysis included 14 samples from four experiments with adequate sample homogeneity [VIII] where one sample represented a pool of 2-3 cross-links. Levene test for homogeneity of variances showed a p-value of 0.31, which is above the required value of $p < 0.05$. Shapiro Wilk test proved normality of the three groups. Results are presented in Figure 17 b). Mean sizes were (66 ± 8) nm below T_t before heating, (46 ± 9) nm above T_t and (64 ± 6) nm below T_t after heating.

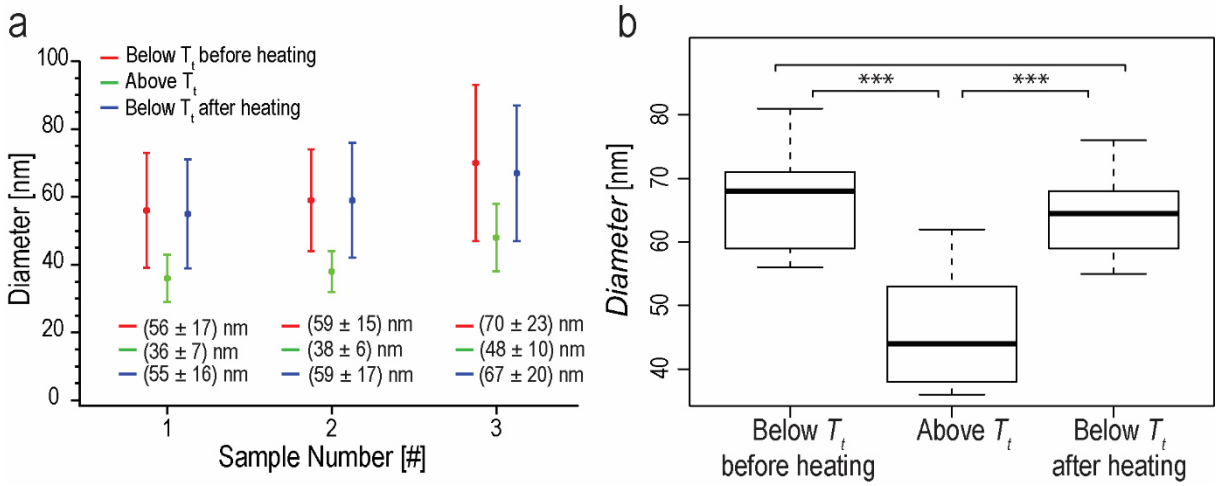

Figure 17: (a) Three representative nanoparticle solutions showing size transitions in thermal cycling measurements. Presented are the mean values with standard deviation, originating from one sample each, derived from intensity-weighted DLS graphs. Corresponding values (in nm) are given below. **(b)** Box plot showing significant differences between particle sizes below and above T_t. Sizes are mean values derived from intensity-weighted DLS measurements in a thermal cycling measurement. The analysis involved 14 samples from four experiments where one sample represented a pool from 2-3 cross-links. Mean sizes are (66 ± 8) nm below T_t before heating, (46 ± 9) nm above T_t and (64 ± 6) nm below T_t after heating. **(a + b)** Reprinted with permission from B. Kracke et al., 2015, Macromolecules 48, 5868-5877, Copyright © 2015 American Chemical Society [125].

[VIII] Sufficient homogeneity was defined via DLS-derived size distributions: Size distributions showing minor larger aggregates in the intensity-weighted plot but lacking this side population in the number-weighted plots were defined as adequate for analysis.

The following table sums up the mean values and corresponding swelling degrees in terms of diameter and volume change. The swelling degrees were defined for each sample separately and then used for definition of mean values. The diameter decrease and volume decrease were calculated with reference to diameters below T_t before and after heating, resulting in two different changes in diameter ΔD1 and ΔD2, and ΔV1 and ΔV2. For particles after dialysis, the average change in diameter was defined to (31 ± 6) % and (28 ± 8) %, while the average volume transition was calculated to (66 ± 9) % and (62 ± 13) %. Samples after dialysis represent samples that were stored above T_t after dialysis. This was observed to increase solution homogeneity. The great change in volume can be explained by the way cross-linking was achieved. As cross-linkers were only present in one layer in the particle interior, the degree of covalent linkages between individual trimers is relatively low: Cross-linking points present in one particle layer would thus enable a complete swelling of the outer third of the particle.

Sample	Mean diameter [nm] below T_t (1)	Mean diameter [nm] above T_t	Mean diameter [nm] below T_t (2)	ΔD1 [%]	ΔD2 [%]	ΔV1 [%]	ΔV2 [%]
Before dialysis	123	75	116	39 ± 3	36 ± 2	77 ± 3	73 ± 2
After dialysis	66	46	64	31 ± 6	28 ± 8	66 ± 9	62 ± 13
Calculated	99	42	99	58	58	92	92

Table 1: Mean diameters from boxplot analysis are presented for samples before and after dialysis at the three different temperature in thermal cycling measurement. Size transitions are analyzed in terms of diameter decrease, compared to the size below T_t before heating (ΔD1) and the size below T_t after heating (ΔD2). For this, each sample was evaluated separately in terms of its diameter change and volume change. All values were summed up as ΔD1 and ΔD2 including the mean value and standard deviation. Corresponding volume changes were summed up as ΔV1 and ΔV2 with mean value and standard deviation. The table compares samples in reaction buffer before dialysis and samples after dialysis with defined size distribution after incubation above T_t.

There is an observable discrepancy between the calculated values from section 4.1.4 and the experimentally observed size change. The calculated values are based on the fully extended contour length of the polymer which may not be feasible. Additionally, the inner two third of polymer chains may be sterically hindered by the cross-linkers, which may cause a decreased value of shrinking of cross-linked particles. A second observance is the difference in size before and after dialysis. This is most likely a result of the viscosity specifications defined in the software, where no specifications for PEG molecules were available. It is assumed that this might result in a viscosity differing by a factor of two which inversely affects the defined size in the Stokes-Einstein relation (refer to formula 3.4).

The swelling ratios by volume with (66 ± 9) % (ΔV1) and (62 ± 13) % (ΔV2) match significantly well the reported value for cross-linked ELP hydrogels, which have been reported to exhibit a volume change of 62.4 % [120]. However, one has to consider that the degree of cross-link density can affect the swelling degree of a matrix [177] and could thus lead to considerable differences in swelling degrees. Also γ-irradiation cross-linked hydrogels have been studied in terms of volume changes [161, 302, 303] and swelling ratios were defined as the ratio of weight of fully hydrated gel / weight of dried gel. They were shown to range around 2 above T_t for gels of various degrees of cross-link density [302] whereas the swelling ratio increased to around 35 below T_t. In an analogous way, one may compare the volume ratio of swollen and collapsed cross-linked particles to non-cross-linked particle volumes. This gives a ratio of 3.6 above T_t and a

factor of 10 below T_t. Comparatively, the ratio of a swollen / collapsed cross-linked particle volume is 2.7. Mean volumes applied were 14137 nm³ (30 nm diameter) before cross-link, 50965 nm³ after cross-link (46 nm diameter) above T_t and 137258 nm³ below T_t (64 nm diameter).

4.3.2. Particle sizing with FCS

FCS measurements and fitting procedures were carried out by Björn Hellenkamp at the physics department of TU Munich.

FCS measurements were carried out to support size distributions derived from DLS measurements. For this, nanoparticles were labeled with Atto647N to enable size characterization via FCS. Measurements presented in Figure 18 show a nanoparticle sample eight days after cross-link. The average diameter with standard deviation was defined to (60 ± 13) nm below T_t and (48 ± 7) nm above T_t from the correlation functions shown below.

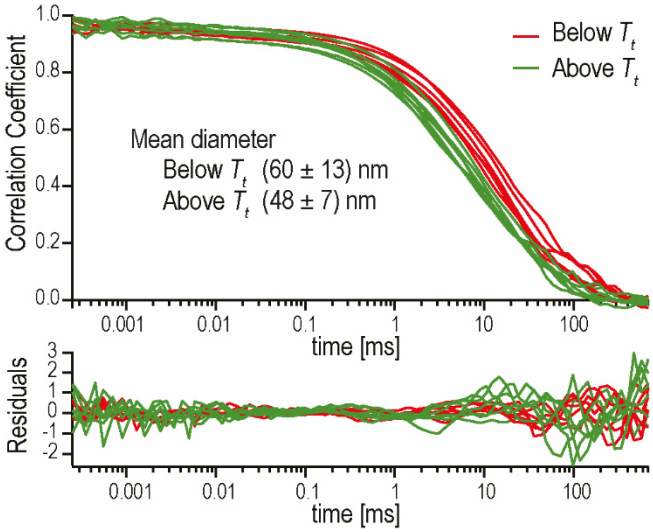

Figure 18: Correlation functions from fluorescence correlation spectroscopy of cross-linked nanoparticles eight days after cross-link, labeled with Atto647N.

All FCS experiments are summed up in Table 2, where the correlation functions from Figure 18 correspond to 'experiment 3'. As described in chapter 3.2.6, the fitting procedure of the correlation function varied for the different experiments, depending on solution heterogeneity. Sizes at RT were defined for two other samples, originating from two different experimental sets. Diameters were defined by one measurement each to 52 nm and 57 nm respectively (experiment 1 and 2). These values fit to the results from experiment 3 presented above.

a

Experiment Nr.	Temperature [°C]	Diffusion Coeff. [µm²/s]	Diameter [nm]
1	25	9.4	52
2		8.6	57
3		7.7	63
		5.9	83
		9.0	54
		10.8	45
		8.2	59
		8.5	57
Mean ± Std			59 ± 11

b

Experiment Nr.	Temperature [°C]	Diffusion Coeff. [µm²/s]	Diameter [nm]
3	42	12.9	56
		18.2	40
	44	16.2	47
		14.2	53
		20.2	38
		16.2	47
	45	13.9	56
4	42	15.6	47
		17.3	42
		17.9	41
		12.8	57
Mean ± Std			48 ± 7

Table 2: FCS-derived diffusion coefficients and corresponding diameters defined in four separate experiments, consisting of one or more measurements. Measurement temperature was **(a)** below T_t and **(b)** above T_t. Experiments yielded mean diameters of (59 ± 11) nm and (48 ± 7) nm below and above T_t.

Measurements above T_t were repeated in FCS experiment 4 with a sample from a different experimental set. Mean sizes below and above T_t were defined to (59 ± 11) nm and (48 ± 7) nm, which corresponds to an average diameter decrease of 19 % and a volume decrease of 46 %.

4.3.3. AFM imaging of cross-linked nanoparticles

Particles were visualized via AFM intermittent-contact mode in H_2O_{dd} three days after cross-link. The sample shown in Figure 19 was imaged before dialysis and thus shows a notable number of residual trimers. Size distributions were obtained from four images with 5 µm scan size, leading to a count of 911 trimers (population 1) and 27 nanoparticles (population 2). Sizes were approximated by fitting each particle section line with a Gauss fit, giving the diameter by the FWHM of the Gaussian fit. The resulting particle distributions are presented in Figure 19 b) and c). The mean particle diameter was approximated by a Gauss fit on the distribution and was subsequently corrected for the effect of the tip radius. The latter was assumed to be around 10 nm, as a nominal 20 nm tip radius given by the manufacturer seemed to overestimate tip dimensions. This resulted in a trimer population with (20 ± 6) nm diameter and a nanoparticle population with (65 ± 10) nm diameter. With 41 trimers in a nanoparticle, these distributions represent an apparent cross-link efficiency of 55 %, with the residual trimers equaling a theoretical count of 22 nanoparticles. It is assumed that the hydrophobic parts of the non-cross-linked trimers have a considerable affinity towards the hydrophobic HOPG surface. The shielding of the hydrophobic nanoparticle interior by a hydrophilic shell might also be an explanation for the smaller number of counted nanoparticles. Thus, the apparent cross-link efficiency might underestimate the real value. Furthermore, it was observed that surface coverage with particles could fluctuate on different spots on the surface. It was concluded that no definite evaluation of cross-link efficiency can be made from this imaging method.

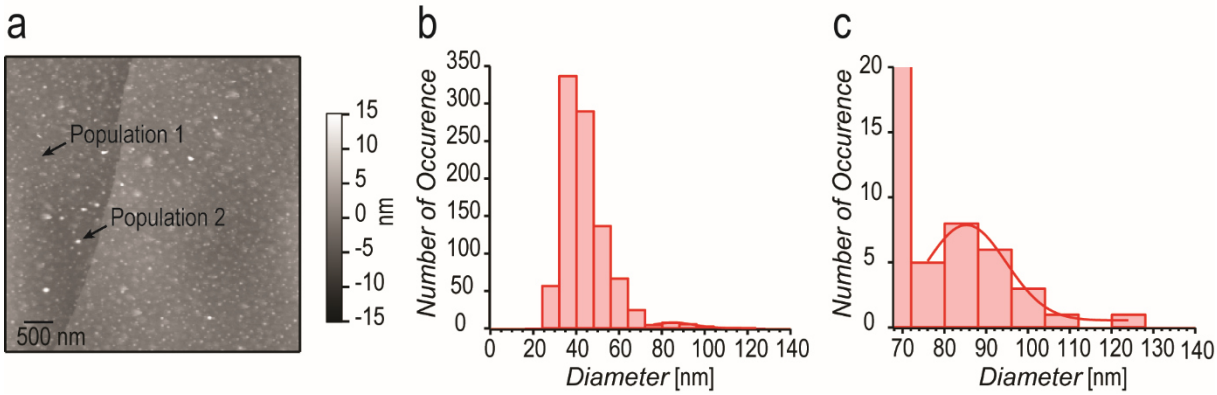

Figure 19: AFM image of cross-linked nanoparticles before dialysis, imaged in fluid on HOPG via intermittent-contact mode. **(a)** Height image with 5 µm scan size. Scan parameters: Setpoint 0.27 V, scan rate 0.4 Hz, drive amplitude 1 V. **(b)** Histogram resulting from a total count of 938 particles from the analysis of four images of 5 µm scan size respectively. There are two populations present which were divided into trimers (population 1) and cross-linked nanoparticles (population 2). Particle diameters were obtained through a Gaussian fit on the particle section line, yielding the FWHM of the particle. The distribution was divided at a value of 72 nm. The mean diameter with standard deviation for both distributions were obtained by a Gauss fit on each distribution and yielded (40 ± 6) nm for the trimers and (85 ± 10) nm for the nanoparticles. The values were subsequently corrected by deducing twice a tip radius of 10 nm. **(c)** Zoom image of size distribution of the nanoparticle population. **(a - c)** Reprinted with permission from B. Kracke et al., 2015, Macromolecules 48, 5868-5877, Copyright © 2015 American Chemical Society [125].

A representative zoom image (500 nm scan size) of a single particle is shown in Figure 20 a) with a three-dimensional representation in Figure 20 b). The image was obtained from a different nanoparticle solution where particles had been cross-linked in 0.5 mM phosphate buffer / 0.33 mM MES with 3.33 mM NaCl. The particle illustrated had a diameter of 74 nm and a height of 19 nm. The detected height of imaged particles was typically smaller than expected. This might have been caused by the adsorption of the particle onto the surface, causing a flattening of the particle, or via effects of the measurement.

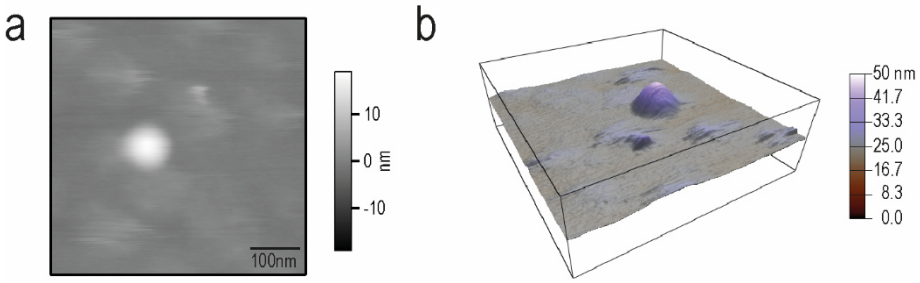

Figure 20: (a) Zoom image with 500 nm scan size showing a particle with 74 nm width and 19 nm height. Scan parameters: Setpoint 0.21 V, integral gain 14, scan rate 0.5 Hz, drive amplitude 1 V. **(b)** Corresponding three-dimensional representation. The scaling in x-y plane is the same as in (b).

The reduction in the measured height of nanomaterials, imaged via AFM intermittent-contact mode has been reported in a work of Mechler et al. [304], where factors influencing the final height data were named to be the value of the cantilever's oscillation amplitude and material properties. During the imaging of ELP nanoparticles, it was generally observed that a reduced setpoint could damage the particle and result in a "smearing out" in scan direction, which was assigned to an increased force exerted on the sample. Therefore, the setpoint value was continuously adjusted during measurement to keep particle damage to a minimum.

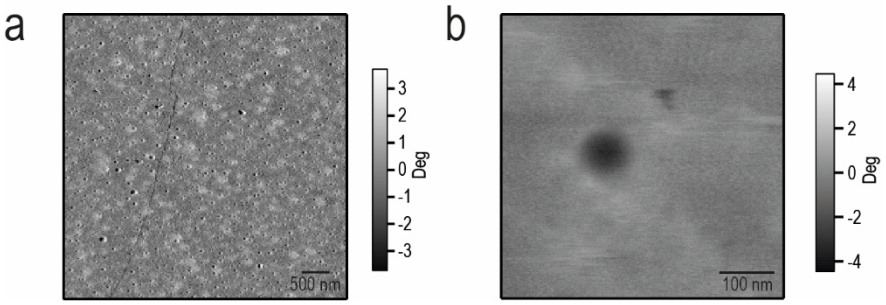

Figure 21: Phase image of cross-linked nanoparticles on HOPG, imaged via AFM intermittent-contact mode in fluid. Phase images correspond to height data shown in Figure 19 and Figure 20. **(a)** The sample was adsorbed on HOPG and the fluid cell was filled with 2 mL of H_2O_{dd}. **(b)** The sample was adsorbed on HOPG and the measurement was carried out in the fluid drop of 100 µL.

As described in chapter 3.2.6, the phase signal obtained by AFM intermittent-contact mode can give information about differences in material properties [263, 267, 268]. Here, the difference in phase signal was used in addition to topographic information in order to distinguish the protein from the sample surface. Figure 21 shows the phase signal for the two images presented above. It can be observed that the phase was reduced when imaging protein-based material.

4.3.4. TEM imaging of cross-linked nanoparticles

TEM measurements were carried out by Dr. Christoph Kaiser at the chemistry department of TU Munich.

Nanoparticle solutions were analyzed via TEM imaging both before and after dialysis. Representative images can be seen in Figure 22 a + b), illustrating nanoparticle solutions prepared two days after cross-link. The corresponding particle distributions are shown in Figure 22 c + d) for a sample before and after dialysis respectively. Both samples feature two size populations. For solutions in reaction buffer, a population with small size was assigned to trimers (population 1) with diameters of (13 ± 3) nm. The larger population was assigned to nanoparticles (population 2) with diameters of (69 ± 11) nm.

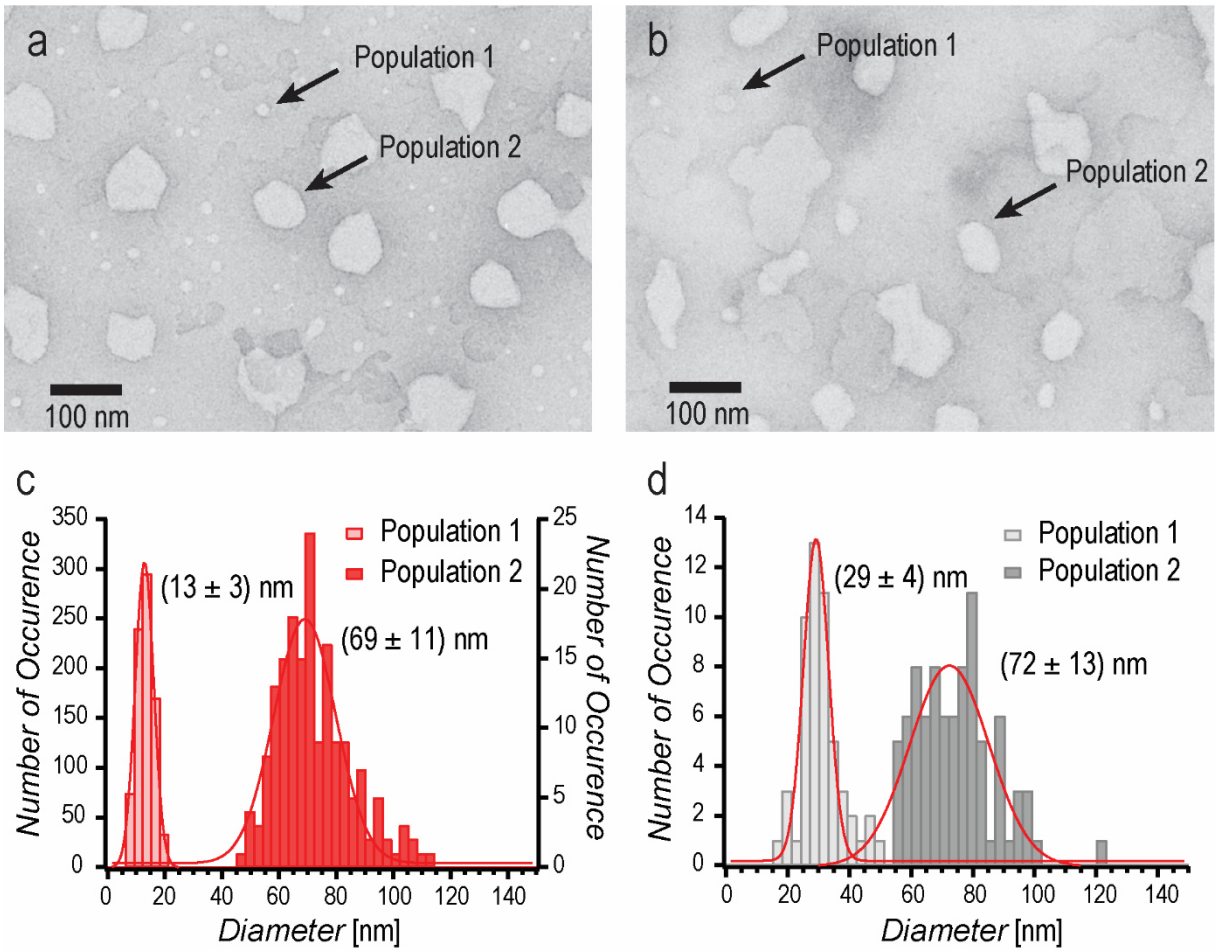

Figure 22: Cross-linked nanoparticles imaged via transmission electron microscopy after negative staining. **(a)** Nanoparticles before dialysis and **(b)** nanoparticles after dialysis in standard buffer. Both images were taken at 20K magnification. The scale bar indicates 100 nm. **(c + d)** Corresponding particle distributions with Gauss fit and resulting mean diameter with standard deviation from both populations respectively. **(c)** Sample before dialysis shows trimers (population 1) of (13 ± 3) nm and nanoparticles (population 2) with (69 ± 11) nm. Values are derived from 986 particles in total. **(d)** Sample after dialysis with leftover trimers (population 1) of mean diameter (29 ± 4) nm and nanoparticles (population 2) of (72 ± 13) nm. Values are derived from 138 particles in total. **(a - d)** Reprinted with permission from B. Kracke et al., 2015, Macromolecules 48, 5868-5877, Copyright © 2015 American Chemical Society [125].

The ratio of trimers to nanoparticles was 813:173. With a calculated packing of 41 trimers into particles, this corresponds to an apparent cross-link efficiency of 90 %. After sample purification via dialysis, nanoparticles (population 2) with (72 ± 13) appeared less

homogeneous in shape while some residual trimers (population 1) with (29 ± 4) nm were observed as well. These values were obtained after subdividing the distributions at a threshold of 50 nm, resulting in 53 trimers and 85 nanoparticles. It can be observed that the overall shape of particles before dialysis is more regular than for particles after dialysis. Nanoparticles in reaction buffer mostly show a spherical shape. This might have been caused by the presence of PEG which is assumed to fill the particle interior to some extent. It appears that the residual PEG molecules might have a stabilizing effect on the particles by occupation of the nanoparticle cavities that would otherwise be filled with water. This would reduce the water loss which can occur during the drying in the staining procedure and upon the sample insertion into high vacuum [305]. The preserving effect of PEG during the drying process of elastin structures has already been observed in earlier studies [306]. The sample after dialysis shows a size increase for population 1. This is probably caused by some association of leftover trimers. The complete images with a total nanoparticle count (including population 1 and population 2) of 986 particles before dialysis and 138 particles after dialysis can be found below.

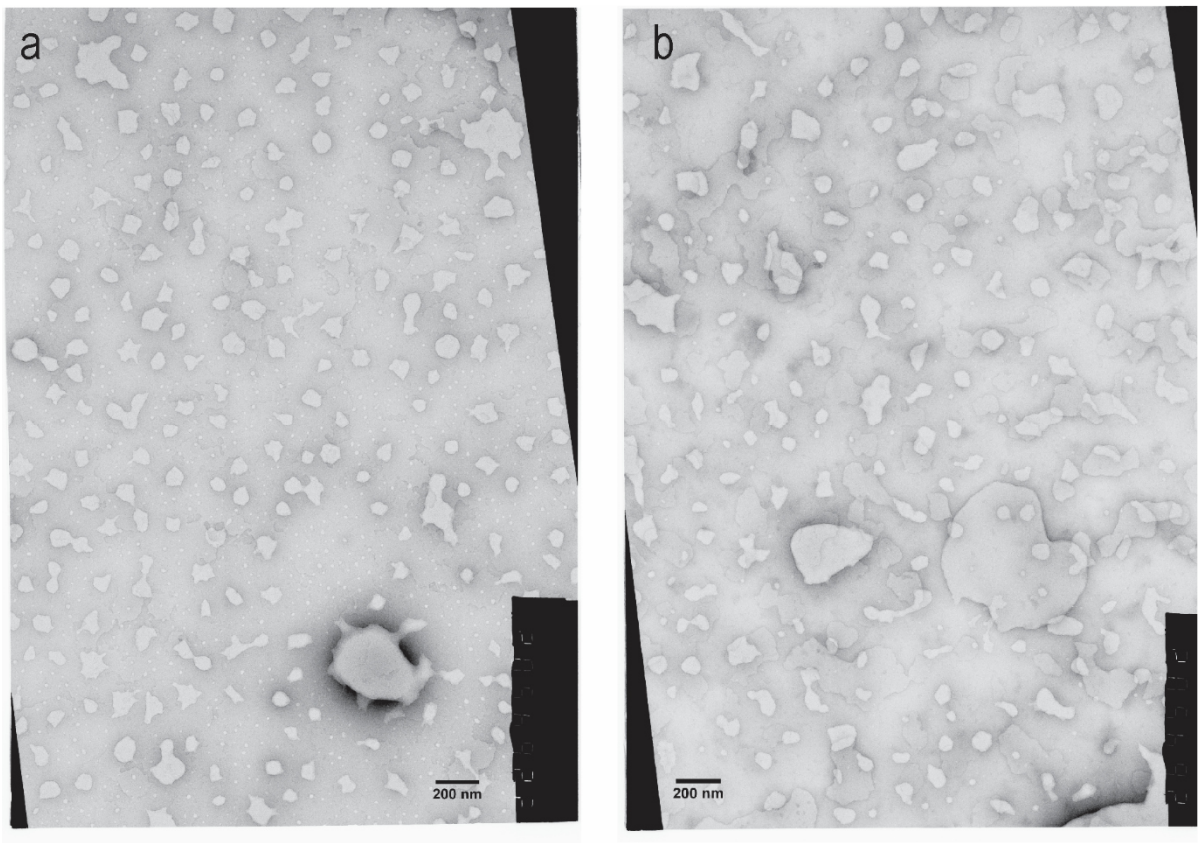

Figure 23: Cross-linked nanoparticles imaged via transmission electron microscopy after negative staining with **(a)** nanoparticle solutions before dialysis in reaction buffer and **(b)** nanoparticles after dialysis in standard buffer. Both images were taken at 20K magnification with scale bar indicated. Reprinted with permission from B. Kracke et al., 2015, Macromolecules 48, 5868-5877, Copyright © 2015 American Chemical Society.

4.3.5. Comparative analysis

Particle size distributions were defined by solvent-based and surface-associated measurements. The mean sizes derived by each method are summarized in Table 3. An overall good agreement of particle sizes, obtained by the diverse methods, can be seen. One has to be aware that each particle sizing method can be influenced by different factors as was indicated in the corresponding sections above.

The DLS-derived sizes correspond to values from boxplot analysis where the size below T_t represents the distribution before heating. Since DLS defines the hydrodynamic radius of a particle [247], a difference in size might be expected for values defined via DLS and TEM measurements. A deviation of TEM-derived particle sizes from their true value might arise from a flattening of the particles upon adsorption and drying of the sample to the carbon grid [305]. This might compensate for the difference in particle sizes from DLS and TEM. It may be speculated that a complete water loss upon TEM sample preparation could lead to a distribution comparable to DLS-derived particle sizes above T_t. From the results obtained, it is concluded that water loss was either relatively low or was compensated by particle flattening upon adsorption to the sample grid. The estimation of the tip radius may have involved some deviation of the approximated particle radii from their true value.

Method	Diameter [nm] below T_t	Diameter [nm] above T_t
DLS	66 ± 8	46 ± 9
FCS	59 ± 11	48 ± 7
AFM	65 ± 10	-
TEM	69 ± 11	-

Table 3: Comparison of particle size distributions obtained by different methods. DLS-derived sizes correspond to mean sizes obtained via boxplot analysis, with the standard deviation giving the scattering of mean size throughout different cross-link samples. The size below T_t represents the value before heating. Values from FCS measurements represent mean size from 8 and 11 samples below and above T_t, obtained from three and two experiments respectively. The smaller size population observed in TEM and AFM measurements is not included for clarity.

Both AFM and TEM images did show two size populations, which were explained by the existence of residual trimers in solution. In DLS measurements this smaller side population may occasionally appear as smaller subgroup or as a shoulder of the main population. In most cases the smaller population was not observable in the DLS graph which is assumed to arise from its low occurrence. They may have been hidden by the larger main population of higher concentration which represented the main fraction of the solution.

4.4. Detailed temperature dependence of cross-linked nanoparticles

This chapter presents a detailed analysis of cross-linked nanoparticles on the basis of DLS measurements, tracking micelle sizes in small heating steps. The progressive shrinking of nanoparticles is observed via size and count rate information from DLS measurements. The analysis is conducted with nanoparticle solutions after different storage periods. It was further tested if residual PEG molecules influence the transition of cross-linked nanoparticles.

Cross-linked nanoparticles were analyzed in detailed temperature trend measurements in the range of 25-55 °C, which were carried out in discrete heating steps of 0.5 °C. The mean sizes were derived from peak analysis of the intensity-weighted DLS graphs. They were tracked simultaneously with the PI and DCR which is presented in Figure 24. The following analysis presents the temperature-dependent size change of the population of interest [IX].

It can be seen from Figure 24 that the phase transition of cross-linked nanoparticles is characterized by a decrease in the particle mean size. The curve for the transition is not as steep as observed for micelle formation in stock solutions before cross-link (refer to Figure 12). It can further be seen that the onset of the transition is shifted to lower temperatures than was observed for the assembly of non-cross-linked particles. This is not unexpected, as local proximity of ELP chains has been reported to support the phase transition [124, 210].

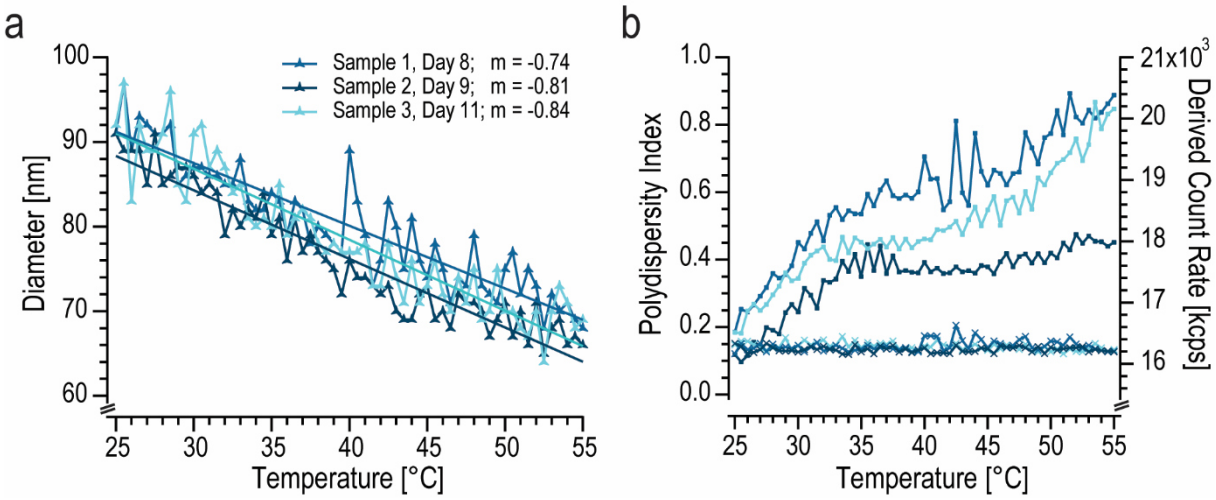

Figure 24: Cross-linked nanoparticles in standard buffer in the second week after cross-link. DLS-derived temperature trends show a size transition with **(a)** mean diameters from peak analysis of intensity-weighted size distributions with line fit giving the slope *m* for each sample. **(b)** corresponding polydispersity index (crosses) as quality control and derived count rate (squares).

The decrease in mean size is accompanied by an increase in the photon count rate. The latter can be assigned to a change in density of the particles as they collapse, causing a change in refractive index as reported for lipid phase transitions [287]. Referring to the change in DCR, a first part of the transition appears to occur in the temperature range 30-38 °C.

Most significantly, the size transition takes place over a broad temperature range. The gradual decrease can be fitted with a line for each sample, giving a mean slope of -0.8. This signifies a

[IX] Larger or smaller population occasionally observed were not included as they were only rarely seen and thus their concentration was rated negligible.

diameter change of approximately 4 nm over a temperature range of 5 °C. Such a relatively broad transition is not unusual. A gradual shrinkage and swelling has been reported for different ELP-based hydrogels that were cross-linked either chemically or via γ-radiation [120, 177, 303, 302]. Exemplarily, a study on chemically cross-linked ELP hydrogels reported on a hydrogel mass decrease of 80 - 90 % that occurred gradually over a 50 °C temperature range [177]. This stands in contrast to the phase transition of non-cross-linked ELPs, which proceeds over a narrow temperature range of around 2 °C [97], which was confirmed for the construct in this work (refer to 4.2.2). One explanation for the transition broadening was found by Trabbic-Carlson et al. [177]. They assumed that it was caused by differences in ELP segment lengths, resulting from various cross-link distances between the individual chains. These segments would show different values for T_t [177]. In the present case, the broadened transition might be provoked by the combination of relatively high polymer concentration in the particle interior and regions of lower protein density in the outer third of the particle. Additionally, the presence of cross-linker segments in the interior may influence the swelling behavior. The gradual decrease was exclusively assigned to a temperature effect and denoted as time-independent since each sample was equilibrated 5 min before each measurement.

It can further be observed that mean sizes are larger than defined for samples in the boxplot analysis from Figure 17 and size distributions are quite broad (see Figure 25). This may be explained by the degree of restructuring, where the boxplot analysis in Figure 17 involved samples in the most complete restructured form.

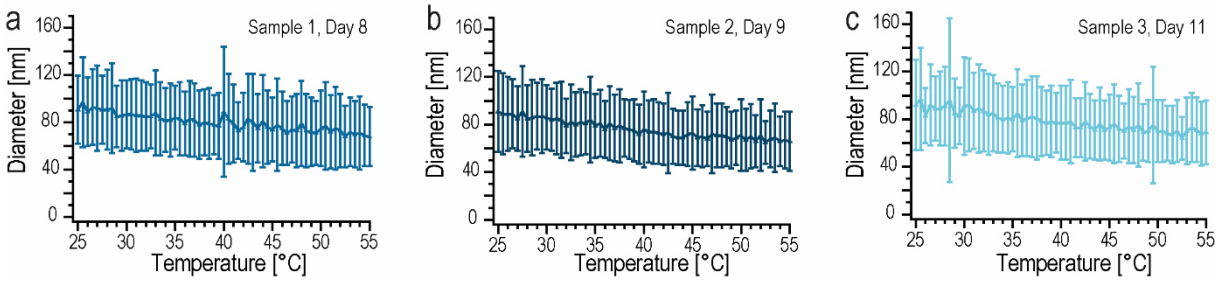

Figure 25: Cross-linked nanoparticles in standard buffer in the second week after cross-link. DLS-derived temperature trend giving mean diameters with standard deviations from peak analysis of intensity-weighted size distributions. Samples shown correspond to samples from Figure 24 with **(a)** sample 1, **(b)** sample 2 and **(c)** sample 3.

To further characterize this effect, the size transition of particles in standard buffer (sample 3 from Figure 24) was analyzed after one and after ten weeks of incubation above T_t. Figure 26 shows that size distributions after buffer exchange can be broader. It is assumed that this is a result of a decreased sample quality, which appears to improve upon storage above T_t. The transfer to new solution conditions with the removal of residual PEG linkers (which are assumed to fill the particle interior) might cause particle deformation or residual coalescence of the particles.

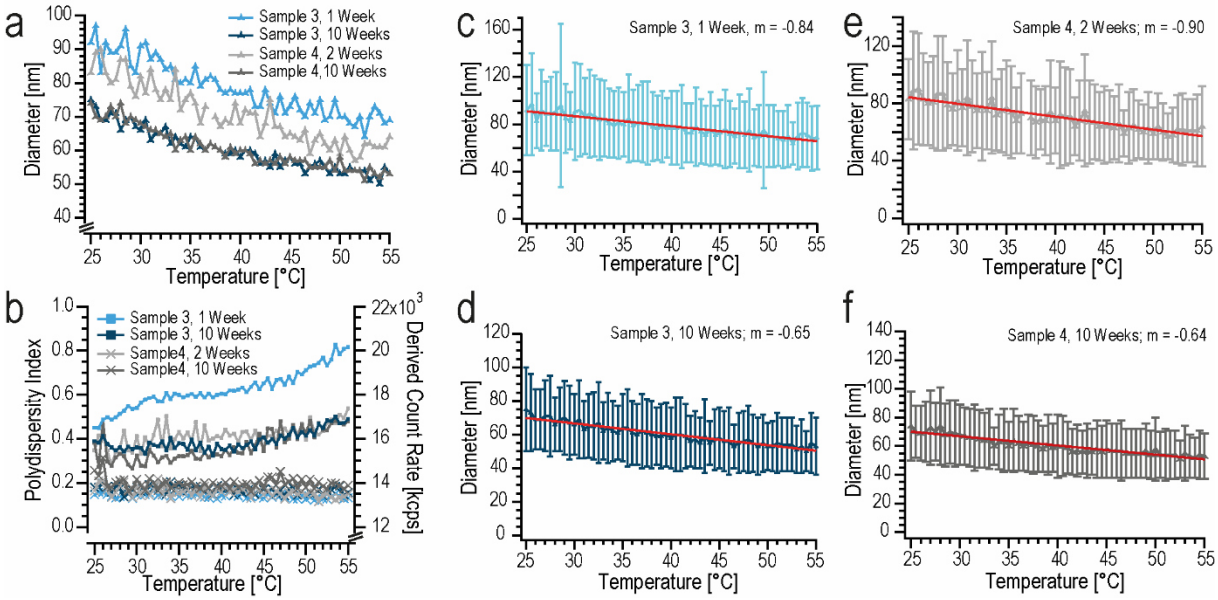

Figure 26: Cross-linked nanoparticles in standard buffer, where each sample represents a pool of three cross-link samples. Solutions were measured after one and ten weeks after cross-link after storage above T_t. DLS-derived temperature trends show a size transition with **(a)** mean diameters derived from peak analysis of intensity-weighted size distributions and **(b)** polydispersity index (crosses) and derived count rate (squares) **(c - f)** mean diameters derived from peak analysis of intensity-weighted size distributions with standard deviations and fit line giving slope *m*. Measurement was carried out after different storage periods for **(c + d)** sample 3 **(e + f)** sample 4.

The decrease of particle mean size upon storage above T_t was observable after different storage periods throughout different experimental sets. Figure 27 shows the temperature trend of four samples from two separate experimental sets (shown in green and red), where sample 3 and 4 are solutions presented in Figure 26. The absolute values of DCR can fluctuate among the samples. This may indicate different degrees of particle compactness. The trend of increasing DCR values upon temperature increase is observed throughout different experimental sets.

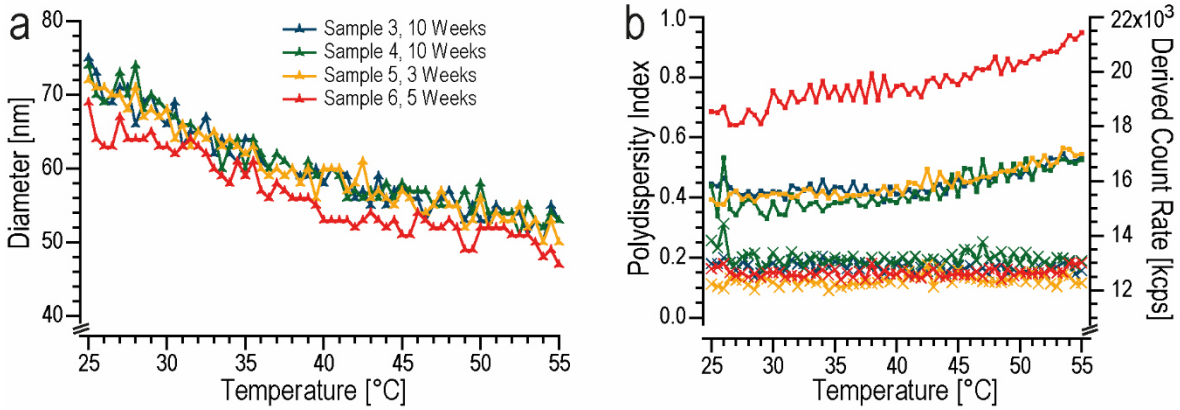

Figure 27: Cross-linked nanoparticles in standard buffer from two experimental sets (sample 3+4 and sample 5+6) after different incubation periods above T_t. DLS-derived temperature trends show a size transition with **(a)** mean diameters from peak analysis of intensity-weighted size distributions and **(b)** corresponding polydispersity index (crosses) as quality control and derived count rate (squares).

It was tested whether residual PEG-linkers in the solution may support the phase transitional behavior of ELPs. For this, two samples were analyzed before dialysis in detailed temperature trend measurements. It can be seen from Figure 28 that mean sizes are shifted to larger values as expected, while the DCR increases substantially. The DCR values are increased by around a factor of around 8 as compared to the DCR values of dialyzed samples shown in Figure 24. The

sizes with standard deviations of the DLS-derived particle distribution are shown in Figure 28 c) and d) where the most significant decrease in size is observed in the temperature range 25 to 35 °C and 25 to 42 °C respectively. A fitting of the region 25 to 35 °C gives a negative slope for each sample, with a value of -3.1 and -2.7. This supports the assumption that PEG molecules may support the size transition of cross-linked nanoparticles.

It has been reported elsewhere that PEG hydrophobicity increases with increasing chain length, which implies a higher ratio of ordered water structure around the molecule [284]. As this might have effects on other dissolved molecules, it was speculated that PEG molecules could drive phase separations [284]. In a study on ELP coacervate particles, PEG was denoted to prolong particle stability upon cooling below their T_t [307]. Comparatively, it has been proposed in a different work that at increased concentrations, PEG binds to a protein's hydrophobic sites [308].

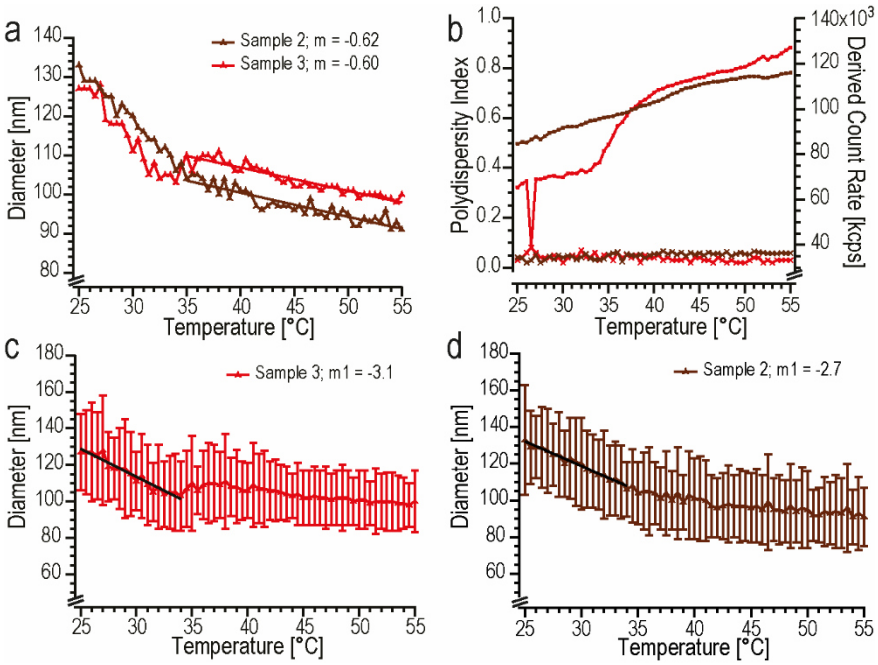

Figure 28: Cross-linked nanoparticles in reaction buffer before dialysis on the first day (sample 3) and the second day (sample 2) after cross-link. DLS-derived temperature trends derived from peak analysis of the intensity-weighted distributions show a size transition with **(a)** mean diameters. Decrease in size is fitted with a line in the temperature ranges 35-55 °C giving slope *m*. **(b)** corresponding polydispersity index (crosses) and derived count rate (squares). **(c + d)** mean diameters with standard deviations. Decrease in size is fitted with a line in the temperature ranges 25-34 °C, giving slope *m*.

Especially in the region below the T_t for particle formation of non-cross-linked ELPs, which is below 35 °C, a significant impact of PEG can be observed in that it appears to cause a pronounced particle shrinkage. On a molecular scale, the effect of pulling other solutes out of solution via increased PEG concentrations of large MW was already denoted as a competition for hydration [309]. This fits the findings noted above about PEG having a supporting effect on phase transitions. Taken together, PEG may support the phase-transition of cross-linked ELP nanoparticles, as concluded from DLS-based size measurements.

4.5. Long-term stability analysis

This chapter gives first insight into the long-term stability of nanoparticle solutions. Dialysis was carried out against different solutions and a transfer into standard buffer was proven successful. The stability over long-term storage was tracked in two experimental sets over several weeks. The effect of storage temperature on nanoparticle solution homogeneity was analyzed. The chapter is based on the publication of the author: Kracke et al. (2015) Macromolecules 48,5868-5877 [125].

The first long-term experiment included samples stored in reaction buffer and standard buffer. Figure 29 a) shows a cross-linked sample that was kept in reaction buffer and Figure 29 b) shows a sample that is a pool of two cross-linked samples brought into standard buffer via dialysis. The particle size transition was tracked via DLS heating cycle measurements. The solutions were stored for seven weeks below T_t at RT and subsequently for two weeks above T_t. In both presented particle solutions, the particle population of interest was observable for 12 weeks. The sample stored in reaction buffer contained occasional aggregates after nine weeks of storage. This fraction was around 1 % in the intensity-weighted distribution and absent in the number-weighted distribution. It was thus accounted as negligible fraction and was not included in the graph. The percentage of stable nanoparticles solutions ranged around 50 to 75 % for samples in standard buffer, and around 20 to 50 % for samples in reaction buffer over long-time storage. The defined stability yields fluctuated between the different measurement dates. These differences were assumed to be caused by residual aggregates in some measurement volumes, rendering it more difficult to define the population of interest. A second larger population became apparent after longer storage times and particle tracking was terminated in week 17-18 when aggregates became more dominant.

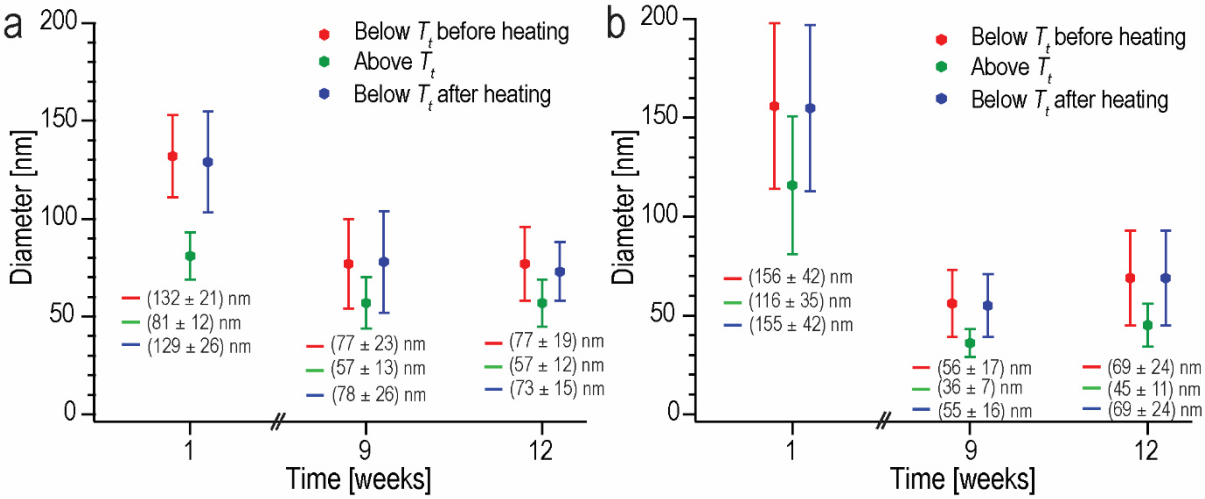

Figure 29: Size distribution of two nanoparticle solutions shown over a period over 12 weeks in DLS heating cycle measurements. Below each distribution, the corresponding mean size and standard deviation are given, based on intensity-weighted DLS graphs. Size distributions after several weeks were obtained after storage above T_t. Nanoparticles were stored in **(a)** reaction buffer (representing one cross-linked sample) and **(b)** standard buffer (representing a pool of two cross-links that were dialyzed against standard buffer). **(a + b)** Reprinted with permission from B. Kracke et al., 2015, Macromolecules 48, 5868-5877, Copyright © 2015 American Chemical Society [125].

Stability was also proven for several samples kept in reaction buffer. This is in agreement with a different study that reported on an increased stability of ELP coacervate particles if PEG

molecules were present at high concentration [307]. It was generally observed that samples measured on the first day after buffer exchange had a broader size distribution. The difference in size after nine weeks of storage is considerable for both particle solutions. From this it was concluded that storage temperature might have an effect on particle sizes and solution homogeneity. A storage above T_t was assumed to facilitate a particle restructuring, leading to smaller particles and generating a solution with increased homogeneity. To confirm this assumption, a second long-term study was carried out to further analyze the effect of temperature on storage.

The data shown in Figure 30 shows three different samples originating from a different experimental set [X]. Each sample had been partitioned into two aliquots and stored below and above T_t, which is shown in Figure 30 a) and b) respectively. The samples shown here originated from pooled samples, where sample 1 was composed of 9 cross-linked samples and sample 2 and 3 originated from 7 individual cross-links each. The cross-link samples had been stored above T_t for 2 weeks to facilitate particle stabilization after cross-link. This was needed to improve sample quality which had been considerably low directly after cross-link in this experimental set. The pooled samples were centrifuged at 5000 g for 5 min four weeks after cross-link. 30 days after cross-link, each sample was split into two aliquots, which were stored below and above T_t. The storage experiment showed a yield of approximately 60% stable particle solutions.

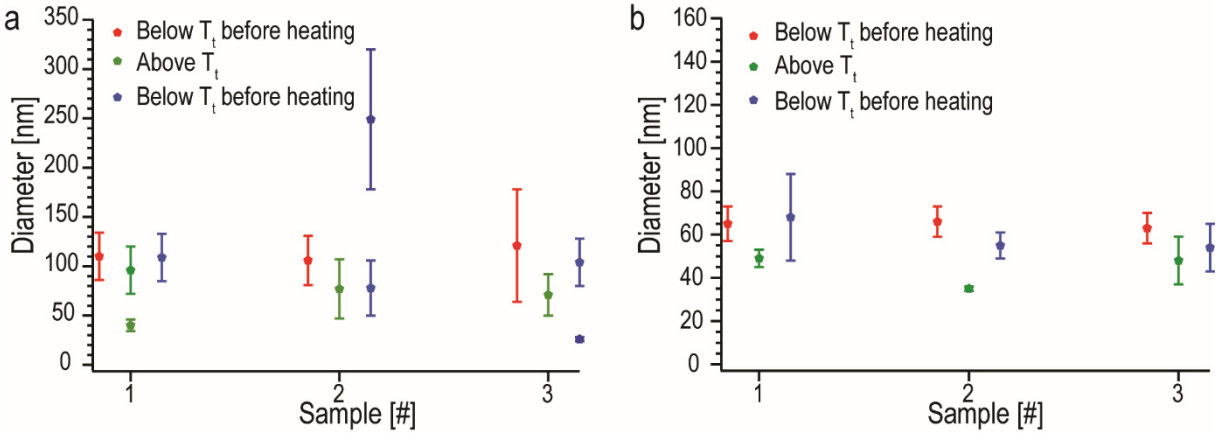

Figure 30: DLS-based thermal cycling measurement of three samples after 11 weeks of storage. Samples were stored above T_t for the first three weeks after cross-link and then splitted into two aliquots which were stored at different temperatures for the last eight weeks. Storage of the sample aliquots was done **(a)** below T_t at RT and **(b)** above T_t at 50 °C.

Figure 30 supports the assumption that storage temperature has an impact on the sample quality. Samples stored below T_t occasionally had a broader size distribution than particles stored above T_t. For some particle solutions in Figure 30 a) a divided peak of the size distribution was observed, indicating two size populations. This resulted in a broadened distribution around the mean, as can be observed for sample 2 above T_t or sample 3 below T_t before heating. It was observed that also a storage above T_t can result in residual aggregates, as was seen for sample 2 above T_t, where the correlation data indicated the presence of a second size population which

[X] This data set also proves well the independency of the size results on scattering angle, as these measurements were taken at 90° scattering angle, in contrast to all other presented measurements taken at 175° scattering angle. The samples were typically incubated for three minutes before a measurement of 5 runs with 30 s run duration.

was not apparent in the size graph. It can be concluded that long-term storage can be accompanied by the aggregation events in each storage method. A storage of protein-based nanoparticles over several weeks can bring with it the coalescence of individual particles. This can appear as a broadened size distribution, an increased PI, or the development of a second larger size population. Centrifugation or dilution (with standard buffer and in some cases an addition of H_2O_{dd}) can be an approach to purify the sample from residual aggregates. Samples shown in Figure 30 were treated in this way to enable size measurements.

The emergence of occasional particle fusions over long term storage is not unexpected for nanoparticles in the size range of 100 nm. As was introduced in 2.3, the attractive force between two particles increases when their distance *s* becomes smaller than their diameter *d*. This effect is even more pronounced for non-spherical particles [238]. A storage below T_t implicates that the outwards lying ELP chains are in the unfolded state. This might reveal more regions that could interact with other particles. For these particles with non-perfect spherical shape, a larger number of atoms in the immediate surrounding can lead to a larger attractive force [238]. Referring to a storage above T_t, it may further be assumed that the particles have a size below a critical value (100 nm) which may keep them from settling due to increased Brownian motion [230]. Furthermore, a more compact particle holds a higher charge density, which may have positive effects on particle solution stability.

Long-term stability of the cross-linked nanoparticles may be further increased by adjusting solution pH into a more basic range, which is assumed to result in an increased negative charge of the particle surface and therefore in an increased electrostatic repulsion [233].

4.6. Loading ELP nanoparticles

This chapter includes a theoretical estimation of a particle's loading capacity and first results on loading studies via DLS measurements and colocalization studies by confocal microscopy. First preliminary loading studies were carried out via tracking of micelle formation in DLS measurements. ELP solutions were spiked before cross-link with a stock solution of FITC-labeled dextrans. As hydrophobic loading molecule, CrA-COOH was added to ELP solutions before cross-link and to particle solutions after cross-link. CrA-COOH had been synthesized by Kang Zhao, at Tianjin University, China and was provided via the group of Prof. L. Schröder at the Leibniz-Institut für Molekulare Pharmakologie (FMP) Berlin. First experiments on colocalization studies were developed with Gary B. Braun at the Sanford Burnham Prebys Medical Discovery Institute (La Jolla, CA, USA).

4.6.1. Estimation of loading capacity

With 3 monomers per trimer and 41 trimers per particle, the MW of a particle $MW_{particle}$ can be calculated as follows (without including MW of incorporated PEG-linkers):

$$MW_{particle} = 27811.7\ \frac{g}{mol} \cdot 3 \cdot 41 = 3.42 \cdot 10^6\ \frac{g}{mol} \tag{4.14}$$

Taking into account the reported water content of ELP coacervates with 63 % by weight [174], the total MW of a particle MW_{total} in its coacervate form above T_t can be approximated:

$$MW_{total} = 3.42 \cdot 10^6\ \frac{g}{mol} \cdot \frac{100}{37} = 9.24 \cdot 10^6\ \frac{g}{mol} \tag{4.14}$$

With a water content of 63 % by weight, this gives a total MW_{H2O} of incorporated water molecules in one particle with $5.82 \cdot 10^6$ g/mol. With the MW of one water molecule as 18 g/mol, this can be converted into the number of loaded water molecules N_{H2O}:

$$N_{H2O} = \frac{5.82 \cdot 10^6\ \frac{g}{mol}}{18\ \frac{g}{mol}} = 3.23 \cdot 10^5\ \frac{molecules}{particle} \tag{4.15}$$

The nanoparticle concentration $c_{particles}$ can be calculated with the starting protein concentration of 13 µM in the cross-link reaction and the calculated value of 41 trimers per micelle, which corresponds to 106 nM particles in solution.

$$c_{particles} = 106 \cdot 10^{-9} \frac{mol}{L} \cdot 6.022 \cdot 10^{23} \frac{molecules}{mol} = 6.38 \cdot 10^{16} \frac{particles}{L} \tag{4.14}$$

One obtains $638 \cdot 10^{11}$ nanoparticles in 1 mL solution. With this, one can obtain the total number of H_2O molecules $N_{H2O,loaded}$ that would be loaded in the nanoparticles above T_t:

$$\begin{aligned} N_{H2O,loaded} &= 3.23 \cdot 10^5\ \frac{molecules}{particle} \cdot 6.38 \cdot 10^{16}\ \frac{particles}{L} \\ &= 2.1 \cdot 10^{22}\ \frac{molecules}{L} \end{aligned} \tag{4.15}$$

This would lead to a potential concentration $c_{H2O,loaded}$ of 35 mM loaded water molecules:

$$c_{H2O,loaded} = \frac{2.1 \cdot 10^{22} \frac{molecules}{L}}{6.022 \cdot 10^{23} \frac{molecules}{mol}} \approx 35\ mM \qquad (4.15)$$

With the occupied volume of a water molecule as 30 Å^3 [310]. The R_g of one FITC-dextran was defined to 1.7 nm, via its reported l_{bond} = 6 Å [311] and a number of segments N = 25 (with a MW of one dextran as 162 g/mol). For simplicity, the FITC-dextran was approximated by a sphere, which gives a volume of 5.6 nm³ for one FITC-dextran, with a R_h of 1.1 nm. This leads to a diminished concentration of dextran content, denoted as fraction $\theta_{dext,loaded}$:

$$\theta_{dext,loaded} = \frac{0.03\ nm^3}{5.6\ nm^3} \cdot 35\ mM \approx 188\ \mu M \qquad (4.16)$$

The potential loading concentration of 35 mM would thus be reduced to a fraction of loaded FITC-dextran $\theta_{dext,loaded}$ of 188 µM. This value was calculated for a particle in its coacervate form above T_t. As the water content below T_t is assumed to be much higher in analogy to ELP hydrogels [175, 176, 177], this may greatly influence the particle loading capacity. It is assumed that it is further influenced by the hydrophobicity of the molecule.

4.6.2. Loading studies via DLS

First preliminary loading studies involved the addition of FITC-dextrans to ELP solutions. Micelle formation was analyzed by DLS measurements above T_t, which proved particle formation in the presence of FITC-dextrans at different concentrations. The results can be seen in Figure 31. Micelle sizes did not change at dextran concentrations of 20 and 200 µM. The mean size of around 32 nm diameter did not seem to be influenced by the addition of dextrans at these concentrations. One first test involved the addition of NaCl, which caused a great increase in micelle size, as can be seen below.

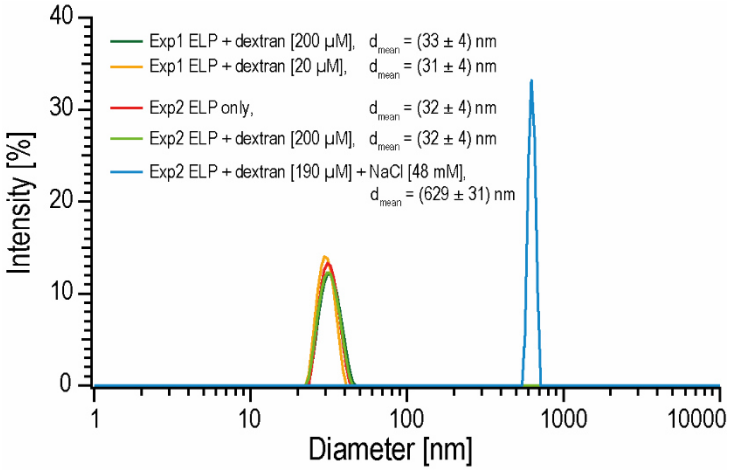

Figure 31: ELP solutions above T_t, presented as intensity-weighted graph from DLS measurements. ELP solutions were spiked with dextrans at various concentrations (20 or 200 µM) or contained dextrans at 190 µM with additional NaCl at 48 mM.

The solution showed some degree of heterogeneity, as can especially be seen in the correlation function (Appendix 7.3). Especially the sample containing NaCl indicates a second side population in the correlation graph. Populations observable at longer time delays might be a

result of high dextran concentration or some decrease in pH upon addition of dextrans and NaCl (pH value of ELP stock was at pH 9.8) It was reported elsewhere that a very high loading extent can lead to the increase of particle size [2]. This effect did not appear in the intensity plot. It may be speculated that the concentration range did not exceed possible loading capacity or excess dextrans remained in solution and did not result in particle size increase. To enable further analysis via confocal imaging, particle sizes were increased via the addition of NaCl, as will be outlined in chapter 4.6.3.

It was tested if micelle formation, cross-linking and thermal cycling of cross-linked nanoparticles were influenced by the presence of a hydrophobic molecule. For this, CrA-COOH was used as testing molecule. Thermal switching was analyzed for nanoparticle solutions, to which the cage was added before cross-link. It can be seen in Figure 32 a) that assembly into micelles can occur upon a temperature trigger in the presence of CrA-COOH. Figure 32 b) shows sizes of cross-linked nanoparticles, where 30 µM CrA-COOH had been added before cross-link. The graph sums up six samples from two experimental sets. ANOVA analysis with a posthoc Tukey test proved statistical significance of size differences above and below T_t in the presence of CrA-COOH. Levene test for homogeneity of variances showed a p-value of 0.75, which is above the required value of $p < 0.05$. Shapiro Wilk test proved normality of the three groups.

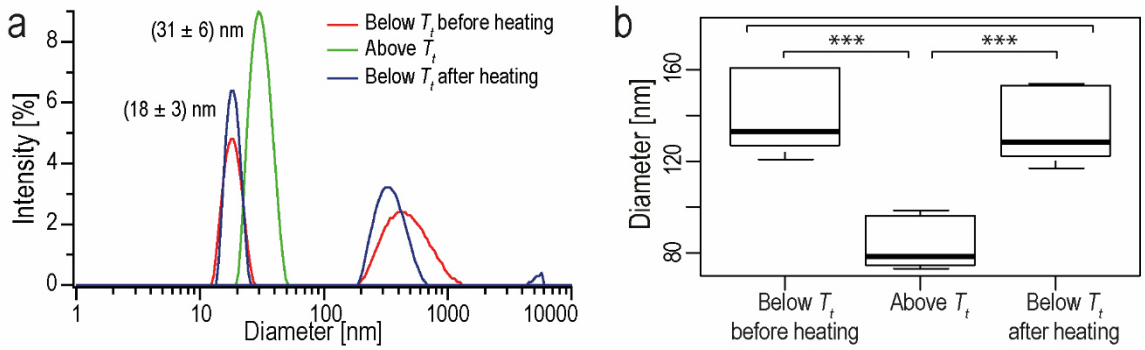

Figure 32: (a) DLS thermal cycling measurement proving micelle formation in the presence of CrA-COOH (30 µM), pH 10.0. Diameters of populations of interest are 18 ± 3 nm below T_t before heating (red), 31 ± 6 nm above T_t (green) and 19 ± 2 nm below T_t after heating (blue). **(b)** Boxplot analysis showing mean sizes of nanoparticles after cross-link in the presence of CrA-COOH (30 µM). DLS-derived mean sizes from thermal cycling measurements, including 2 experiments with six samples in total. Mean sizes are (139 ± 17) nm below T_t before heating, (83 ± 11) nm above T_t and (134 ± 16) nm below T_t after heating.

The effect of CrA-COOH on nanoparticle solution homogeneity was tested in one experiment where CrA-COOH was added after cross-link. For this, nanoparticles were cross-linked, brought into standard buffer and stored above T_t. Figure 33 a) shows the solution ten days after cross-link. The nanoparticle solution containing CrA (49µM) was measured 11 days after cross-link in a DLS heating cycle, shown in Figure 33 b).

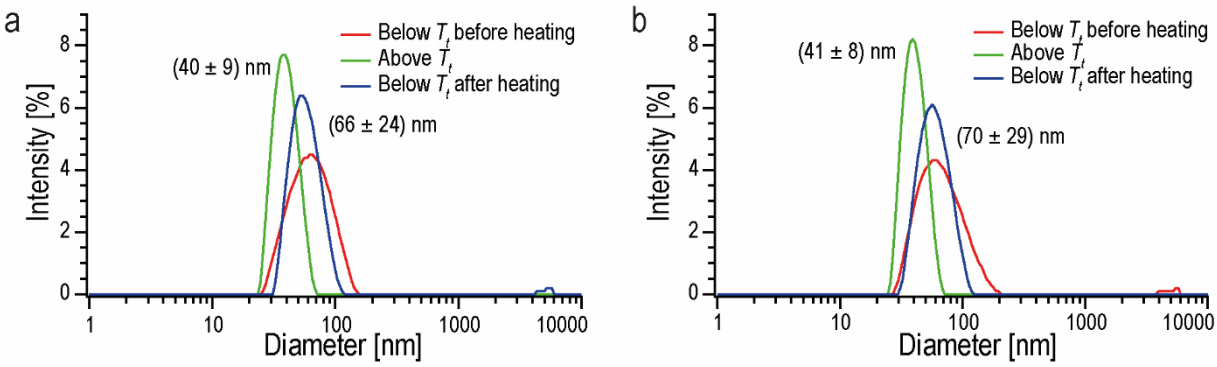

Figure 33: Size distribution of nanoparticles derived by intensity-weighted DLS graphs from heating cycle measurement. **(a)** Cross-linked nanoparticles ten days after cross-link, before addition of CrA-COOH. Diameters of populations of interest are (66 ± 24) nm below T_t before heating (red), (40 ± 9) nm above T_t (green) and (58 ± 15) nm below T_t after heating (blue). **(b)** Cross-linked nanoparticles, 11 days after cross-link, spiked with CrA-COOH (49 µM). Diameters of populations of interest are (70 ± 29) nm below T_t before heating (red), (41 ± 8) nm above T_t (green) and (60 ± 17) nm below T_t after heating (blue).

It can be seen that the addition of cage did not affect particle solution stability and thermal cycling measurements proved thermal switching. It was concluded from DLS measurements that the addition of CrA-COOH at these concentrations did not result in any significant differences in particle size.

4.6.3. Colocalization studies with loaded nanoparticles

The chapter is based on the publication of the author: Kracke et al. (2015) Macromolecules 48,5868-5877 [125].

For verification that the FITC-dextrans were loaded into particles, the nanoparticles were labeled with DyLight™ 594 to enable colocalization studies. Loading of nanoparticles was carried out before cross-link and was followed by dialysis against standard buffer o/n below T_t. In order to visualize the particles in confocal images, the sample was spiked with salt to increase particle size. Figure 34 shows FITC-dextran-loaded particles in solution with a final salt concentration of 32 mM in a-c) and 16 mM in d-f).

The figure shows nanoparticles, labeled with DyLight™ 594 detected in the red spectral range. Green fluorescence from dextrans, carrying a FITC label, was found in colocalization with the nanoparticles. To exclude the possibility of channel cross-talk during imaging, particles were excited at the two wavelengths separately and fluorescence was recorded at both detectors HyD2 (500-550 nm) and HyD4 (653-695 nm). The control sample of dialyzed FITC-dextrans only can be found in the Appendix 7.7.

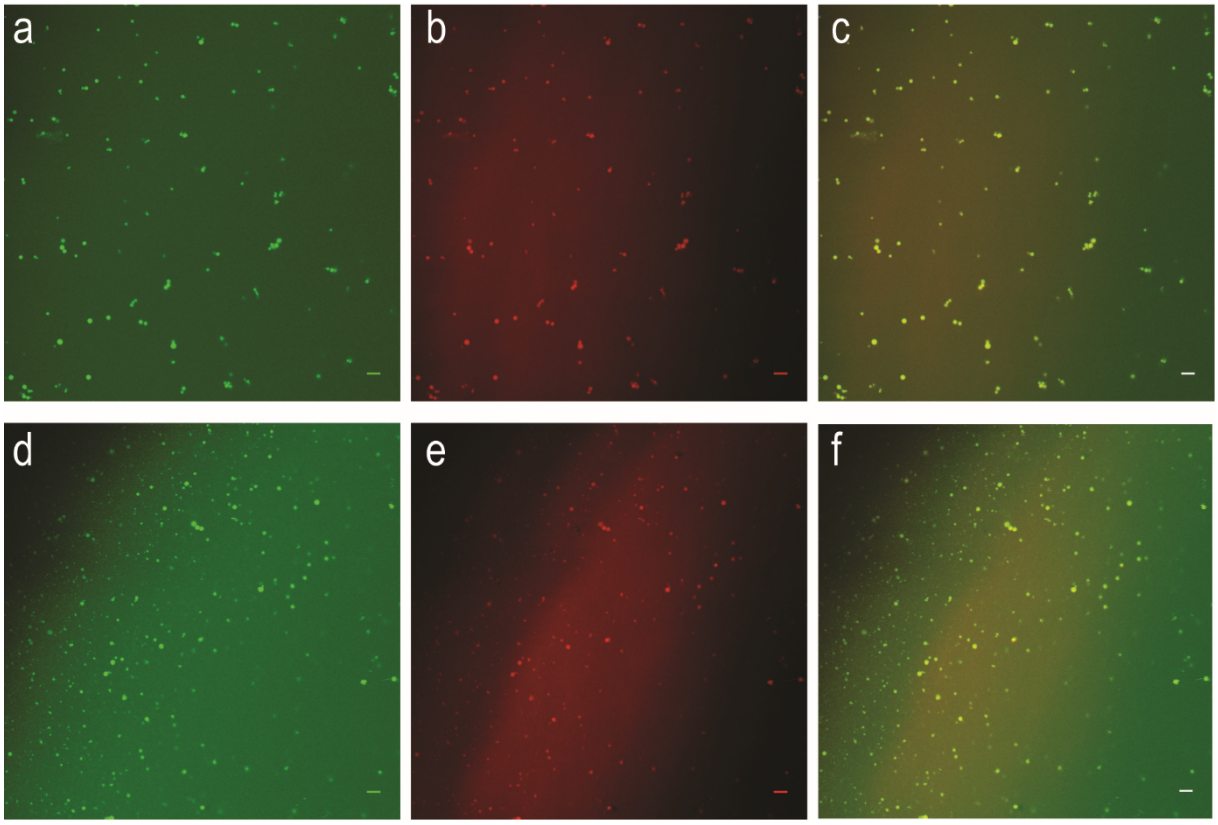

Figure 34: Colocalization study showing fluorescence images of DyLight™ 594-labeled particles loaded with FITC-dextran (4 kDa). Particle sizes were increased by the addition of salt in different concentrations with **(a-c)** 32 mM NaCl and **(d-f)** 16 mM NaCl. FITC signal was recorded via λ_{exc} = 488 nm, λ_{em} = 500-550 nm and DyLight™ signal was obtained via excitation at λ_{exc} = 633 nm and λ_{em} = 653-695 nm. The scale bar for all images is 5 µm. **(a – f)** Reprinted with permission from B. Kracke et al., 2015, Macromolecules 48, 5868-5877, Copyright © 2015 American Chemical Society [125].

For an additional experiment on the effect of temperature on dialysis, particles were dialyzed after loading at both at high and low temperature (refer to Appendix 7.7). It was concluded from the results presented that nanoparticles were successfully loaded with FITC-dextrans. It may be assumed that the size of dextrans (4 kDa) did hinder a diffusion of the molecules out of the particles. The effect of size and dialysis temperature may be a highly interesting subject for further analysis.

In summary, the particles have been loaded with molecules of different polarity: Firstly, PEG molecules were able to diffuse into the particle interior to facilitate cross-link. Secondly, FITC-dextrans were incorporated into the particles before cross-link. To enable visualization by confocal microscopy, particle sizes were increased by the addition of salts to the particle solution prior to cross-link. Their localization in labeled nanoparticles was proven at room temperature, which demonstrates their tendency to stay inside the particles below T_t. Their relatively large size (4 kDa) might hinder their diffusion into bulk solution or their retention might be caused via interactions with the ELP chains. In a third study, the hydrophobic cryptophane cage was added to nanoparticle solutions, which did not affect micelle formation and solution homogeneity of cross-linked particles. It remains to be elucidated whether these can diffuse in and out of the particle interior, in a temperature dependent manner.

Water channels have been reported for ELPs [181] and ELP coacervates were shown to have an overall high water content [168, 174], which may facilitate a loading of cross-linked ELP nanoparticles with hydrophilic molecules. It is further assumed that the hydrophobic intermolecular contacts [124, 126] may also enable a particle loading with hydrophobic molecules.

5. Conclusion and Outlook

This work reports on the development of a new carrier system on the nanoscale. The nanoparticle is based on an ELP fusion protein in a trimeric constitution, which had been developed by Ghoorchian et al. [37]. Here, the micelles were cross-linked via selective amino acid modification, to enable control over the final nanoparticle constitution. The size distribution of nanoparticle solutions was characterized via different methods and the ability of loading was proven in first loading studies. Being based on ELPs, the carrier systems show a stimulus-responsive behavior in that they show a thermally induced switching in size in a temperature range near body temperature. This temperature-responsiveness was shown via DLS and FCS measurements. This new particle system represents a very interesting carrier for *in vivo* drug administration and applications in the field of nanotechnology.

5.1. Future developments for the presented nanocarrier

Thermal switching was proven for the developed carrier system where temperature responsiveness started well below body temperature and passed 40 °C. As a polymer for application in hyperthermia treatment should be thermoresponsive near to body temperature [58], its responsiveness might be tuned to optimum conditions. The incorporation of smaller cross-linkers in the *particle interior* might reduce a potential hindrance of ELP interaction above T_t and decrease the response time and/or the temperature window of response. Altogether, the fine-tuning of the polymer in the particle interior may reduce the responsive temperature range. Already in an early work, the sharpness of a phase transition was ascribed to a hydrogel's composition [312]. However, it is yet unclear if cross-link with shorter linkers may be possible.

The carrier system may be further functionalized via its *particle shell*. PEG-linkers have proven a valuable tool for polymer modifications: They can largely increase the solubility of the system and decrease the immunogenicity by shielding the construct from the immune system [313]. PEG-linkers fused to biopolymers generally increase their circulation time by protecting the construct from proteolytic enzymes [313]. The modification of the nanoparticles with PEG would alter surface charges on the particle. This might be advantageous over the net negative charge of the foldon-shell, since a net negative charge of particles might lead to a decreased internalization into cells [2]. The effect of this charge in cell association and potential internalization remains to be tested.

The governing release mechanism for the system presented remains to be elucidated. It may be dominated by a diffusion-controlled drug release below T_t or a triggered expulsion of agents upon temperature increase and particle collapse. These mechanisms are the same as described for polymer hydrogels, which are illustrated in Figure 35, adapted from [314].

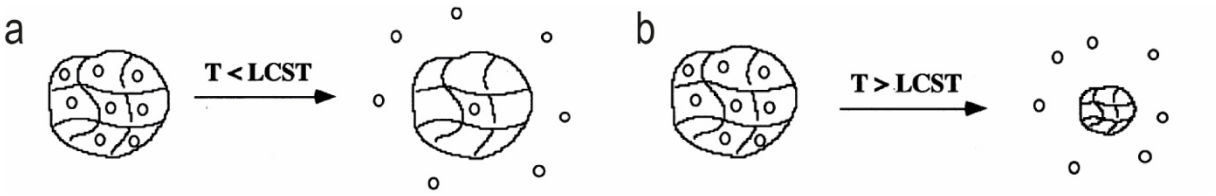

Figure 35: Different modes of drug release from hydrogel materials. **(a)** Diffusion-controlled release below the LCST **(b)** Triggered release through gel collapse above the LCST. **(a + b)** Reprinted from Bromberg and Ron, 1998, Advanced Drug Delivery Reviews 31, 197-221, Copyright © 1998, with permission from Elsevier [314].

These mechanisms have been described in an early work by Hoffman, on the release from temperature-sensitive hydrogels [312]. Both mechanisms have favorable characteristics: The first facilitates a prolonged release while the second can give control over administration via a collapse-induced release as reaction to a defined stimulus. This would show a fast response in the optimal case. The aspects of diffusion-controlled release of agents from hydrogels have been summed up in a review of Bromberg [314] where factors include the polymer's affinity towards the matrix it is encapsulated in, as well as the fraction of bulk water facilitating transport in the hydrogel, compared to bound water molecules that are associated with the polymer chains. It is expected that the release of loaded molecules from ELP-based nanoparticles would be dependent on the swelling degree, similar to the behavior of LCST-hydrogels [312]. A collapse-induced drug release would be caused by the increased pressure inside the gel [314] which can lead to the fast expulsion of the loaded molecules. This mechanism requires that the molecules do not get locked inside the polymer matrix of increased density. In both release modes below and above T_t, the pore size – which is in this work the distance between the foldon groups – is critical for enabling a release. Interactions between loaded molecule and polymer are an important aspect to consider [315].

The particles showed a stepwise shrinkage upon temperature modulation, which may be used in drug administration as such: A stepwise temperature increase would imply a defined degree of particle shrinkage, which would give great control over a sustained release of loaded molecules. Future studies should investigate the temperature-dependent release.

The use of ELP sequences enables a high control over polymer sequence [63], which can open new ways for future modifications. It may be extended with other characteristics such as responsiveness to pH, electromagnetic radiation or redox conditions. Such an additional feature may exploit the ΔT_t mechanism developed by Urry and coworkers [175, 176, 214, 219].

5.2. ELP nanoparticles in context of current nanoparticle developments

There have been various carrier designs developed that went to clinical trial testing which hints at the strong demand for new dosage forms that decrease a drug's toxicity and improve its pharmacokinetics [18]. The design of a novel drug carrier is complex since it must include considerations on size, loading capacity, release modalities and ways of its regulation, system stability, immunogenicity effects and biodegradability. The carrier system represents a valuable concept since it incorporates many advantageous characteristics, as outlined below.

One of the major advantages of micelles is their small size, as diameters ranging between 10 to 100 nm are generally preferred in carrier design [18], as was outlined in section 1.1.1. Thus, the ELP-based nanoparticles developed in this work present a promising carrier system due to their small size. Other ELP-based particle systems below 100 nm have been reported [100, 104, 105, 106, 110, 111, 112, 116]. These systems differ from the carrier developed here in that their assembly was reversible, which lead to the dissociation of the building blocks below their T_t. In contrast to these, the particle system presented here was rendered stable at both below and above its T_t via covalent cross-links in the particle interior. The particles were based on a hydrophobic ELP sequence fused to a hydrophilic headgroup domain, known as foldon [37]. As this hydrophilic domain represents a relatively small fraction of the nanoparticle, a large volume fraction of the particle could be accounted for loading, which might put this system superior to particles with a block copolymer structure where the hydrophilic regions can be bulkier [286].

The carrier shows many possibilities for additional modifications, via site-directed chemical modifications of amino acids in the foldon domain. As the foldon is composed of diverse amino acids with different reactive side groups, it may be reacted with various linker sequences. Exemplarily, lysines or the carboxy-termini may be modified with linker molecules that can target the nanoparticles to a specific recognition molecule. The use of an oligomerization domain as headgroup has the potential for multivalency [316]: In the homotrimeric foldon, three alike amino acids are present per trimer, which can enable the approach of multivalency. Besides this, the particle interior may be modified. This gives a large range of additional modifications, due to the ease of introduction of modifications into the ELP sequence at the genetic level [63] or via posttranslational modifications. Furthermore, the applied cross-link method gives large control over cross-linking points and excludes the risks of chain damage, which can result from cross-linking via γ-irradiation [120].

Particle stability greatly influences its applicability as carrier system. The design presented here liberates the particle system from concentration dependences such as its T_t or the critical micelle concentration, which can be an issue for *in vivo* applications of non-cross-linked particles, as reviewed in [317]. The applicability of carrier systems depending on a critical micelle concentration can suffer from premature decomposition upon administration, if their concentration drops below a critical value. Upon injection of the system, particle concentration is greatly reduced which can lead to the disruption of the equilibrium condition of the nanocarriers. Additionally, monomers can adsorb to plasma proteins which leads to a perturbation of equilibrium conditions that can result in the disruption of micellar assemblies [317].

A challenge lies in the establishment of a system that is stable and permeable at the same time [7]. Thereby, a triggered release mode is favorable, since it gives control over the administration. A main characteristic of the system presented here is the temperature-driven size transition. With an average volume change of (66 ± 9) % this carrier shows a drastic response upon a temperature stimulus.

Liposomes can be prepared with different sizes and differences in permeability at increased temperature [318]. Besides temperature-induced releases, volumetric particle changes have been achieved with pH-responsive carrier systems such as responsive nanocapsules [7]. Comparatively, a temperature-triggered drug release had been achieved with other systems, such as polymeric micelles based on PNIPAm [39, 40, 41] or liposomes [319, 318, 320]. The latter system was studied for applications in hyperthermia treatment in terms of a heat-mediated drug release in hyperthermia treatment [319, 321, 322]. These carrier systems differ in their chemical nature, which can have various effects on size, loading capacity, stability (as noted above this can be dependent on the critical micelle concentration) and biodegradability. These factors can influence the applicability of the carrier system and should thus be considered in drug carrier design. Regarding for example biocompatibility, systems based on synthetic polymers such as PNIPAm share the complication of toxicity and biodegradability issues [42].

An estimation of the biocompatibility of the carrier system can be realized by separate consideration of its building blocks. To these belong the ELP sequences (for which biocompatibility aspects have been treated in chapter 1.2.2), the PEG-linkers and the foldon domain. PEG molecules are widely used in the development of hydrogels due to their reported very low inflammatory effect [241] and are part of many therapeutic formulations [323]. In fact, PEG has become one of the most favored molecules in the design of polymer-based drug delivery [324, 325] and its use is advantageous for several reasons. Most prominently, the linkers are known for their high biocompatibility [241, 326, 327]. Protein surfaces modified with PEG-linkers have been shown to be less prone to protein adhesion [327] and PEG-modified liposomes were proven to have an increased circulation time [328, 329]. Thus, PEG molecules incorporated should not decrease the biocompatibility of the particles. The foldon domain has already found application in other designs: Deletion mutants of bacteriophage T4 lacking the tail have been developed as non-infectious nanoparticles [330] and it was shown that deletion mutants could consist of capsid only or capsid and whiskers [331]. Particles involving the foldon domain only are thus assumed to be biocompatible. Furthermore, the particle solution involves no harsh formulation conditions, with the particles suspended in low salt buffer and do not need organic solvents. The addition of linker sequences to the particle shell might further increase the stability of the particles in physiological salt conditions, as was suggested by Ghoorchian et al. [37].

An additional administration route might result from long-term degradation of the carrier. Elastin biocapsules with a size of 0.2 to 10 µm were shown to be degradable by enzyme digestion by elastase [332]. This interesting approach might be combined with ELP fusion nanoparticles: A combination with heat-triggered release, followed by elastase digestion might lead to a two-step release of active components.

Last but not least, a newly developed carrier system should feature a straightforward and cost-effective production route that renders its establishment on the market affordable and provides opportunity for large-scale production [18]. The system presented here does not imply laborious synthesis and purification routes and thus presents a very promising new drug carrier system for diverse applications in medicine, diagnostics or other areas involving controllable delivery.

5.3. Potential applications of thermoresponsive nanoparticles

Nanoparticles that show a temperature-induced size change can be interesting for applications in disease states that are associated with an increase in heat of the affected tissue or for treatment methods that involve the application of heat [312]. An approach of ELPs for hyperthermia treatment was proposed by Chilkoti and coworkers, which pointed at the potential of heat-induced ELP nanoparticle formation for hyperthermia treatment. Their studies reported the temperature-triggered assembly of ELPs which resulted in heat-induced accumulation of ELPs at the tumor-site [97, 98, 99]. The nanoparticle system developed here would differ in its responsiveness in that particles would be stable at both low and high temperature while showing a defined size change upon the application of heat, assumed to provoke a drug release from the carrier. The increased vascular permeability of tumor tissue upon hyperthermia treatment [333] could even increase efficacy of the administration route. Comparatively, the thermal triggering of liposomes in hyperthermia approaches have shown promising results [334], which hints at the great potential therapeutic benefit of such systems.

A second interesting application might be in the field of inflamed tissue. A knee can hold an increased temperature when inflamed, which can be around 36 °C in rheumatoid arthritis [335]. Comparatively, a different study approximated a value of 36.7 °C after increased stress of 1 h walking [336]. Compared to this, an unstressed knee holds a temperature of approximately 33 °C [335], which denotes a significant difference in temperature. ELPs have been proposed for application in cartilage tissue engineering in form of heat-induced aggregates [71, 337, 338]. Transglutaminase cross-linked ELP matrices were suggested for treatment of damaged articular cartilage [339] and intra-articular drug delivery from ELP depots was shown [340]. This study on intra-articular injection of ELP fusion proteins into knee joints exploited the heat-induced aggregation of ELPs, which was above body temperature for the applied construct. The study observed an increased half-life and prolonged release of the drug depots [340]. Other approaches employed functionalized nanoparticles for intra-articular administration [341, 342]. The first study analyzed the targeting of the cartilage extracellular matrix by small sized particles, in dependence of their particle surface coverage with matrix ligands that had been attached in order to prevent rapid clearing from their destination [341]. The second approach analyzed particle binding to synoviocytes via surface-attached ligands on the particle surface and observed an increased retention of these particle-associated therapeutic proteins in the rat stifle joint *in vivo* [342].

Responsive nanoparticles applied to the joint might show a heat-triggered release of loaded anti-inflammatory agents, which might reduce the risk of a stress-induced inflammation. In this context, the release of anti-inflammatory agents from 100-400 nm particles based on PNIPAm has been proposed for inter articular drug administration [343]. A different approach was conducted with PNIPAm-based nanoparticles embedded in a hydrogel matrix transmitting heat upon mechanical stress [344]. A thermoresponsive particle system based on ELPs with well-known biocompatibility [68, 69, 70] might thus be promising in this application field. Apart from the proposed application of ELP fusion proteins for prolonged release of protein-drugs in osteoarthritis treatment [345], the use of nanocarriers for rheumatoid arthritis treatment has been

mentioned before [346, 347]. The application of heat or cold to affected joints in rheumatoid arthritis has been an approach to treat patients, which has been reviewed in [348] with view to potential benefits, drawbacks and contraindications [348]. If treatments based on heat or cold application prove successful in the future, they may be combined with a drug administration via a thermally switchable carrier. The carrier may be loaded with anti-inflammatory agents, which may be released upon a defined temperature stimulus. It remains to be elucidated if such applications are feasible. Nonetheless, these examples hint at the great potential of a carrier system on the nanoscale that can be switched in size by a temperature trigger.

6. Abbreviations

A	alanine
AFM	atomic force microscope
amp	ampicillin
ANOVA	analysis of variance
ccc	critical coagulation concentration
Carboxy-Cryptophane-A	CrA-COOH
DCR	derived count rate
DLS	dynamic light scattering
DLVO	Derjaguin-Landau-Verwey-Overbeak
DMSO	dimethyl sulfoxide
DTT	dithiothreitol
ELP	elastin-like polypeptide
EPR	enhanced permeability and retention
E. coli	*Escherichia coli*
FITC	fluorescein isothiocyanate
FWHM	full width half maximum
G	glycine
h	hours
H_2O_{dd}	double distilled water
HOPG	highly oriented pyrolytic graphite
ITC	inverse transition cycling
ITT	inverse temperature transition
IPTG	Isopropyl-β-D-thiogalactopyranosid
kDa	kilo Dalton
LCST	lower critical solution temperature
MES	2-(N-morpholino)ethanesulfonic acid
Min	minutes
MW	molecular weight
MWCO	molecular weight cutoff
NMR	nuclear magnetic resonance

OD	optical density
o/n	overnight
P	proline
PBS	phosphate buffered saline
PCS	photon correlation spectroscopy
PI	polydispersity index
Peg	poly(ethylene glycol)
PNIPAm	poly(*N*-isopropylacrylamide)
P	proline
pI	isoelectric point
PSD	particle size distribution
QELS	quasielastic light scattering
rpm	rounds per minute
RT	room temperature
SDS	sodium dodecyl sulfate
SDS-PAGE	SDS polyacrylamide gel electrophoresis
s	seconds
SPM	scanning probe microscopy
T_t	transition temperature
V	valine
VdW	Van der Waals
v/v	volume per volume
WLC	worm-like chain
w/v	weight per volume

7. Appendix

7.1. Single-molecule measurements on ELPs

Tip functionalization and single molecule measurements on ELP trimers were carried out by Stefanie Krysiak at the Central Institute for Medical Engineering (IMETUM), TU Munich. The chapter is based on the single molecule measurement results shown in the Supplement of the publication of the author: Kracke et al. (2015) Macromolecules 48,5868-5877 [125].

The thermoresponsiveness of individual trimers was tested via single molecule force curves. Measurements were conducted in a fluid cell below T_t (25 °C) and above T_t (55 °C) and comprised extension-retraction cycles with a constant pulling velocity of 0.5 µm/s. Before retraction, the tip was stopped in proximity of the surface for a dwell time of one second. This was done to facilitate bond formation between the cysteines of the ELPs and the maleinimide groups on the substrate. Force-distance curves during retraction visualized worm-like chain (WLC) stretching of PEG chains and final rupture.

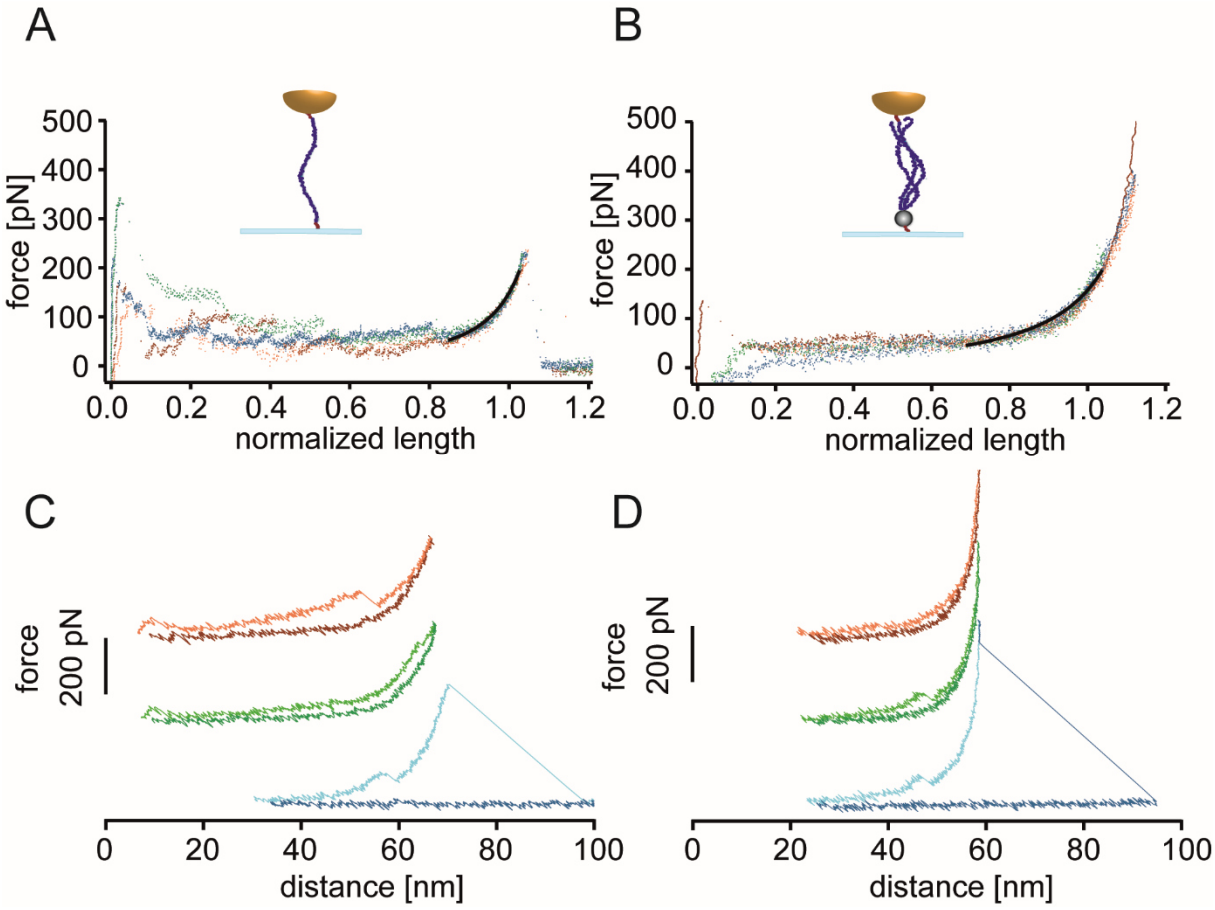

Figure Appendix 1: Single molecule measurements on ELPs **(a + b)** Normalized force-distance curves fitted with the WLC model, for **a)** ELP monomer MGHK(GVGVP)$_{80}$C and **(b)** ELP trimer MGH(GVGVP)$_{40}$-foldon. Each graph shows 5 curves in overlay and normalized to one at a force of 150 pN. **(c + d)** Successive extension-relaxation measurements of MGH(GVGVP)$_{40}$-foldon-C in water **(c)** below T_t and **(d)** above T_t did not show distinct hysteresis. **(a – d)** Reprinted with permission from B. Kracke et al., 2015, Macromolecules 48, 5868-5877, Copyright © 2015 American Chemical Society [125].

Hysteresis measurements were carried out at smaller force distances. In the case of an ELP stretching event between tip and surface, the starting point of the force distance was increased.

Extension relaxation cycles were repeated in this way until final rupture occurred. The results are presented in Figure Appendix 1. The image illustrates the stretching and rupture of ELPs in force-distance curves. The curves were fitted with the WLC model from which the persistence length was defined and compared to the persistence length of monomeric ELPs. This was done in order to prove that indeed trimers were stretched. The traces with the fits can be seen in Figure Appendix 1 a + b). The persistence length was defined to be 0.27 nm for the monomeric construct MGHK$(GVGVP)_{80}$C and 0.13 for the trimer MGH$(GVGVP)_{40}$-foldon-C which reveals that in the trimeric form, several sequences are stretched in parallel. Figure Appendix 1 c + d) show several stretch-relaxation events of the trimeric form before final rupture occurs. The absence of hysteresis both below and above T_t indicated that no ITT occurred for a single ELP.

Sample preparation

AFM force spectroscopy measurements were carried out with a MFP-3D SA (Asylum Research, Santa Barbara, CA, USA). Briefly, ELP-functionalized tips were incubated in close proximity to a maleinimide-modified surface to facilitate bond formation, followed by extension-retraction cycles.

The covalent linkage of ELP monomers and trimers to the AFM tip of silicon nitride cantilevers (MLCT, Bruker SPM Probes, Camarillo, CA, USA) was done by the following protocol. The cantilevers were activated in an oxygen plasma chamber at 20 W and 0.3 mbar for 15 min. They were rinsed with dry acetone (VWR, Germany) and incubated in a Vectabond solution (Axxora, Germany) for 10 min. The solution contained 50 µl Vectabond in 2.5 mL dry acetone. After they were rinsed in dry acetone and chloroform (VWR, Germany), they were incubated in bis-hydroxysuccinimide (Di-NHS-PEG) at a concentration of 2.5 mM, dissolved in dry chloroform. The solution was incubated for 60 min at RT, followed by rinsing with dry chloroform, ethanol and sodium-borate buffer (50 mM, pH 8.1). In the following, the ELP monomeric sequence MGHK$(GVGVP)_{80}$C and the trimeric construct MGH$(GVGVP)_{40}$-foldon-C were used at a concentration of 50 µM. The proteins were dissolved in sodium-borate buffer and cantilevers were incubated with the respective protein solution for 1 h at RT. The cantilevers were finally rinsed with ultrapure water (Biochrom, Germany).

The glass surface was functionalized with maleinimide groups as follows. Glass slides were sonicated for 30 min in a 2 % (v/v) Hellmanex solution (Hellma GmbH, Germany), followed by two sonication cycles in ultrapure water. Afterwards, the slides were cleaned with RCA solution at 75 °C for 15 min, dried in an oven and incubated in an oxygen plasma chamber at 100 W and 0.3 mbar for 30 min. The activated surfaces were silane-functionalized by incubation for 10 min in a Vectabond solution, consisting of 50 µL Vectabond in 2.5 mL dry acetone, followed by rinsing in dry acetone and dry chloroform. Next incubation was done in succinimidyl-4-(N-maleinimidomethyl)-cyclohexane-1-carboxylate (SMCC, Thermo-Fisher, Germany) at 3 mg/mL in dry chloroform, which produced a maleinimide layer on the surface. Finally, the slides were rinsed with ethanol and directly used in the AFM measurement.

7.2. Genetic sequencing of ELP fusion protein coding sequence

Sequencing was carried out by the Cleveland Clinic Genomics Core and by GATC Biotech AG (Konstanz, Germany). Plasmids were sent to two laboratories to support the sequencing results. The gene sequences were translated via the ExPASy Bioinformatics Resource Portal. The open reading frame is indicated in red. The pentapeptide containing the cysteine and foldon sequence are underlined.

Sequencing by GATC Biotech AG

Primers

T7	TAA-TAC-GAC-TCA-CTA-TAG-GG
pET-RP*	CTA-GTT-ATT-GCT-CAG-CGG
	pET-RP* equals the T7 terminator (slightly truncated)

Full sequencing data

TTTACTTTAGAAGGAGATATACATATGGGCCACGGCGTGGGTGTTCCCCGCGTAGGTGTCCCAGGTGTGGGC
GTACCGGGCGTTGGTGTTCCTGGTGTCGGCGTGCCGGGCGTGGGTGTTCCGGGCGTAGGTGTCCCAGGTGTG
GGCGTACCGGGCGTTGGTGTTCCTGGTGTCGGCGTGCCGGGCGTGGGTGTTCCGGGCGTAGGTGTCCCAGGT
GTGGGCGTACCGGGCGTTGGTGTTCCTGGTGTCGGCGTGCCGGGCGTGGGTGTTCCGGGCGTAGGTGTCCCA
GGTGTGGGCGTACCGGGCGTTGGTGTTCCTGGTGTCGGCGTGCCGGGCGTGGGTGTTCCGGGCGTAGGTGTC
CCAGGTGTGGGCGTACCGGGCGTTGGTGTTCCTGGTGTCGGCGTGCCGGGCGTGGGTGTTCCGGGCGTAGGT
GTCCCAGGTGTGGGCGTACCGGGCGTTGGTGTTCCTGGTGTCGGCGTGCCGGGCGTGGGTGTTCCGGGCGTA
GGTGTCCCAGGTGTGGGCGTACCGGGCGTTGGTGTTCCTGGTGTCGGCGTGCCGGGCGTGGGTGTTCCGGGT
TGTGGTGTACCAGGCGTGGGTGTGCCGGGCGTGGGTGTTCCGGGCGTAGGTGTCCCAGGTGTGGGCGTACC
GGGCGTTGGTGTTCCTGGTGTCGGCGTGCCGGGCGTGGGTGTTCCGGGCGTAGGTGTCCCAGGTGTGGGCGT
ACCGGGCGTTGGTGTTCCTGGTGTCGGCGTGCCGGGCGTGGGTGTTCCGGGCGTAGGTGTCCCAGGTGTGGG
CGTACCGGGCGTTGGTGTTCCTGGTGTCGGCGTGCCGGGCGTGGGTGTTCCGGGCGTAGGTGTCCCAGGTGT
GGGCGTACCGGGCGTTGGTGTTCCTGGTGTCGGCGTGCCGGGCGTGGGTTACATCCCGGAAGCTCCGCGTGA
CGGTCAGGCTTACGTTCGTAAAGACGGTGAATGGGTTCTGCTGTCTACCTTCCTGGGGCCGGGCTGGCCGTG
ATAATTCGAGCTCCGTCGACAAGCTTGCGGCCGCACTCGAGCACCACCACCACCACTGAGATCC

Protein sequence

F T L E G D I H **Met** G H G V G V P R V G V P G V G V P G V G V P G V G V P G V G V P G V G V P G V G
V P G V G V P G V G V P G V G V P G V G V P G V G V P G V G V P G V G V P G V G V P G V G V P G V G
V P G V G V P G V G V P G V G V P G V G V P G V G V P G V G V P G V G V P G V G V P G V G V P G V G
V P G V G V P G V G V P G V G V P G V G V P G V G V P G V G V P G V G V P G V G V P G V G V P G V G
V P G V G V P G V G V P G V G V P G V G V P G V G V P G V G V P G V G V P G V G V P G V G V P G V G
V P G V G V P G V G V P G V G V P G V G V P G V G V P G V G V P G V G V P G V G V P G V G V P G V G
V P G V G V P G V G V P G V G V P G V G V P G V G V P G V G V P G V G V P G V G V P G V G V P G V G
V P G V G Y I P E A P R D G Q A Y V R K D G E W V L L S T F L G P G W P **Stop Stop** F E L R R Q A C G R
T R A P P P P P L R S

Sequencing by Cleveland Clinic Genomics Core

Primers

T7 Universal-R1	TAA-TAC-GAC-TCA-CTA-TAG-G
T7 terminator	GCT-AGT-TAT-TGC-TCA-GCG-G

Forward sequencing

Gene sequence

ATAAGAAGTTCTCTAGAATATTTTGTTTACTTTAAGAAGGAGATATACATATGGGCCACGGCGTGGGTGTTCCG
GGCGTAGGTGTCCCAGGTGTGGGCGTACCGGGCGTTGGTGTTCCTGGTGTCGGCGTGCCGGGCGTGGGTGTT
CCGGGCGTAGGTGTCCCAGGTGTGGGCGTACCGGGCGTTGGTGTTCCTGGTGTCGGCGTGCCGGGCGTGGG
TGTTCCGGGCGTAGGTGTCCCAGGTGTGGGCGTACCGGGCGTTGGTGTTCCTGGTGTCGGCGTGCCGGGCGT
GGGTGTTCCGGGCGTAGGTGTCCCAGGTGTGGGCGTACCGGGCGTTGGTGTTCCTGGTGTCGGCGTGCCGGG
CGTGGGTGTTCCGGGCGTAGGTGTCCCAGGTGTGGGCGTACCGGGCGTTGGTGTTCCTGGTGTCGGCGTGCC
GGGCGTGGGTGTTCCGGGCGTAGGTGTCCCAGGTGTGGGCGTACCGGGCGTTGGTGTTCCTGGTGTCGGCGT
GCCGGGCGTGGGTGTTCCGGGCGTAGGTGTCCCAGGTGTGGGCGTACCGGGCGTTGGTGTTCCTGGTGTCGG
CGTGCCGGGCGTGGGTGTTCCGGGTTGTGGTGTACCAGGCGTGGGTGTGCCGGGCGTGGGTGTTCCGGGCG
TAGGTGTCCCAGGTGTGGGCGTACCGGGCGTTGGTGTTCCTGGTGTCGGCGTGCCGGGCGTGGGTGTTCCGG
GCGTAGGTGTCCCAGGTGTGGGCGTACCGGGCGTTGGTGTTCCTGGTGTCGGCGTGCCGGGCGTGGGTGTTC
CGGGCGTAGGTGTCCCAGGTGTGGGCGTACCGGGCGTTGGTGTTCCTGGTGTCGGCGTGCCGGGCGTGGGT
GTTCCGGGCGTAGGTGTCCCAGGTGTGGGCGTAACGGGCGTTGGTGTTCCTGGTGTCGGCGTGCCGGGCGTG
GGTTACATCCCGGAAGCTCCGCGTGACCGGTCAGGCTTACGTTCGTAAGACGGTGAATGGGTTCTGCTGTCTA
CCTTTCCTGGGGCCGGGCTGGGCCGTGATAATTCGAGCTCCGTCGACCAGCTTTGCGGCCGCACTTCGAGCA
CCATACTCATCCACCCACTGAGATCCGGGCTGCTTACCAAAGCCCGGAAAGGGAGCTGAGTTGGGCTGGCTG
CTACCGCTGGAGCCATACTAGCATAACCCCATTTGGGGGCCTCCTAACTGTGTCTTGACGGCGTTCTTGCCTG
ACAGAAGTACTATATTCGATGGCCGAATGGACGCTGTCTTGTACGACGCATAAGGCTCGCCGGAGTGTGCAG
TAACGGCCTAGACGTGAACTGCCTAAACAAGTGGCTAGGGGCTCTTTCAGAGGCACTAGACT

Protein Sequence

K K F S R I F C L L **Stop** E G D I H **Met** G H G V G V P G V G V P G V G V P G V G V P G V G V P
G V G V P G V G V P G V G V P G V G V P G V G V P G V G V P G V G V P G V G V P G V G V P G V G V P
G V G V P G V G V P G V G V P G V G V P G V G V P G V G V P G V G V P G V G V P G V G V P G V G V P
G V G V P G V G V P G V G V P G V G V P G V G V P G V G V P G V G V P G V G V P G V G V P G V G V P
G C G V P G V G V P G V G V P G V G V P G V G V P G V G V P G V G V P G V G V P G V G V P G V G V P
G V G V P G V G V P G V G V P G V G V P G V G V P G V G V P G V G V P G V G V P G V G V P G V G V T
G V G V P G V G V P G V G Y I P E A P R D R S G L R S **Stop** D G E W V L L S T F P G A G L G R D N S S S
V D Q L C G R T S S T I L I H P L R S G L L T K A R K G S **Stop** V G L A A T A G A I L A **Stop** P H L G A S
Stop L C L D G V L A **Stop** Q K Y Y I R W P N G R C L V R R I R L A G V C S N G L D V N C L N K W L G A
L S E A L D

Reverse Sequencing

Gene sequence

GAACACGCTCTTTCGGGCTTGTTAGCAGCCGGATCTCAGTGGTGGTGGTGGTGGTGCTCGAGTGCGGCCGCA
AGCTTGTCGACGGAGCTCGAATTATCACGGCCAGCCCGGCCCCAGGAAGGTAGACAGCAGAACCCATTCAC
CGTCTTTACGAACGTAAGCCTGACCGTCACGCGGAGCTTCCGGGATGTAACCCACGCCCGGCACGCCGACAC
CAGGAACACCAACGCCCGGTACGCCCACACCTGGGACACCTACGCCCGGAACACCCACGCCCGGCACGCCG
ACACCAGGAACACCAACGCCCGGTACGCCCACACCTGGGACACCTACGCCCGGAACACCCACGCCCGGCAC
GCCGACACCAGGAACACCAACGCCCGGTACGCCCACACCTGGGACACCTACGCCCGGAACACCCACGCCCG
GCACGCCGACACCAGGAACACCAACGCCCGGTACGCCCACACCTGGGACACCTACGCCCGGAACACCCACG
CCCGGCACACCCACGCCTGGTACACCACAACCCGGAACACCCACGCCCGGCACGCCGACACCAGGAACACC
AACGCCCGGTACGCCCACACCTGGGACACCTACGCCCGGAACACCCACGCCCGGCACGCCGACACCAGGAA
CACCAACGCCCGGTACGCCCACACCTGGGACACCTACGCCCGGAACACCCACGCCCGGCACGCCGACACCA
GGAACACCAACGCCCGGTACGCCCACACCTGGGACACCTACGCCCGGAACACCCACGCCCGGCACGCCGAC
ACCAGGAACACCAACGCCCGGTACGCCCACACCTGGGACACCTACGCCCGGAACACCCACGCCCGGCACGC
CGACACCAGGAACACCAACGCCCGGTACGCCCACACCTGGGACACCTACGCCCGGAACACCCACGCCCGGC
ACGCCGACACCAGGAACACCAACGCCCGGTACGCCCACACCTGGGACACCTACGCCCGGGAACACCCACGC
CCGGCACGCCGACACCAGGAACACCAACGCCCGGTACGCCCACACCTGGGACACCTACGCCCGGAACACCC
ACGCCGTGGACCCATATGTATATCTCCTTCTTAAAGTTAAACAAAATTATTTTCGTAGAAGGGAAACCGTTGTG
GTCCTCCCCTATAGTGAGTCGGTATTACTTTCGCCGGAATCGAGATCTCGGCCAGCGTTGGGTCTGGACTACG
GGTGGCGCATGAATCGTTGCTCCTGTCGATTGAGACCCGGCTAGGCTGGCGGAGGCTGACTTACTGGGTTAG
CAGATTGAATCACCGGAATTCCGCGGAGGAACGGTGAAAGCGTAGACTTGCATGCGTCAAAACGGTTCTGCG
ACCCTTGGTCGTACCAACAG

Protein Sequence

C W Y D Q G S Q N R F D A C K S T L S P F L R G I P V I Q S A N P V S Q P P P A **Stop** P G L N R Q E Q R
F **Met** R H P **Stop** S R P N A G R D L D S G E S N T D S L **Stop** G R T T T V S L L R K **Stop** F C L T L R R R
Y T Y G S T A W V F R A **Stop** V S Q V W A Y R A L V F L V S A C R A W V F P G V G V P G V G V P G V G
V P G V G V P G V G V P G V G V P G V G V P G V G V P G V G V P G V G V P G V G V P G V G V P G V G
V P G V G V P G V G V P G V G V P G V G V P G V G V P G V G V P G V G V P G V G V P G V G V P G V G
V P G V G V P G V G V P G V G V P G V G V P G V G V P G V G V P G V G V P G C G V P G V G V P G V G
V P G V G V P G V G V P G V G V P G V G V P G V G V P G V G V P G V G V P G V G V P G V G V P G V G
V P G V G V P G V G V P G V G V P G V G V P G V G V P G V G V P G V G V P G V G V P G V G V P G V G
Y I P E A P R D G Q A Y V R K D G E W V L L S T F L G P G W P **Stop** **Stop** F E L R R Q A C G R T R A P P P
P P L R S G C **Stop** Q A R K S V F

Remark: The open reading frame was incorrectly marked in the sequence from reverse sequencing. Results from forward and backward sequencing give full data set matching data from GATC Biotech AG sequencing.

7.3. DLS Correlation data

Shown below are typical correlation functions for samples before and after cross-link. Figure Appendix 2 a) shows correlation data corresponding to the sample before cross-link from Figure 11 and Figure Appendix 2 b) shows correlation data for the sample after cross-link in reaction buffer, from Figure 16 a).

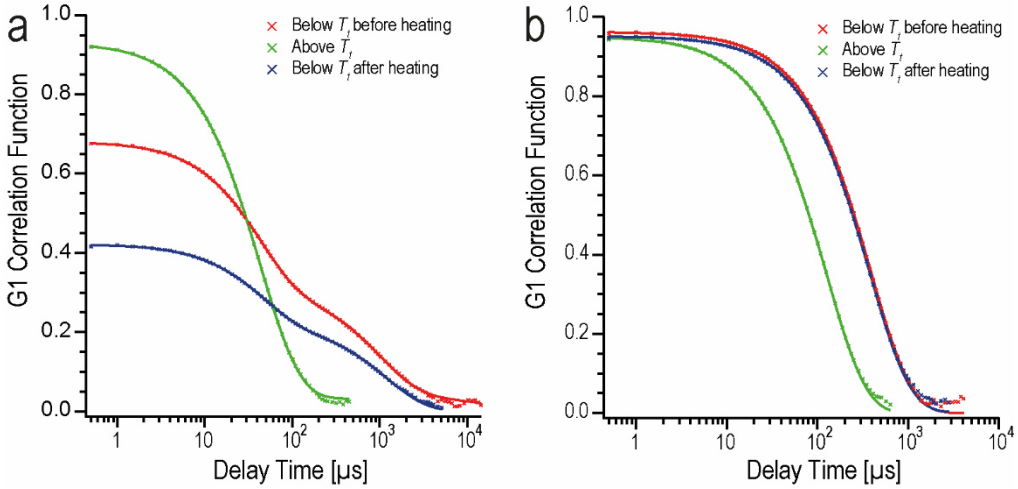

Figure Appendix 2: Correlation function from DLS heating cycle measurements on ELP samples with data points (crosses) and fit. Samples were measured below T_t before heating (red), above T_t (green) and below T_t after heating (blue). **(a)** Before cross-link and **(b)** after cross-link.

Samples before cross-link below T_t contained a second population, as can be seen from the second decay. Heating increased homogeneity of the solution, resulting in a correlation function with a single decay above T_t. Samples after cross-link show a similar form of the correlation function, shifted to longer delay times below T_t, representative for a population of larger size. The small fit deviation from measurement data at longer delay times is assumed to be caused by some minor fraction of larger populations in the sample.

Correlation data for the three representative samples in standard buffer after dialysis shown in Figure 17 a) can be seen in Figure Appendix 3 a - c). As above, the difference in correlation data upon heating is obvious. The small fit deviation from measurement data at longer delay times is assumed to be caused by some minor fraction of larger populations in the sample.

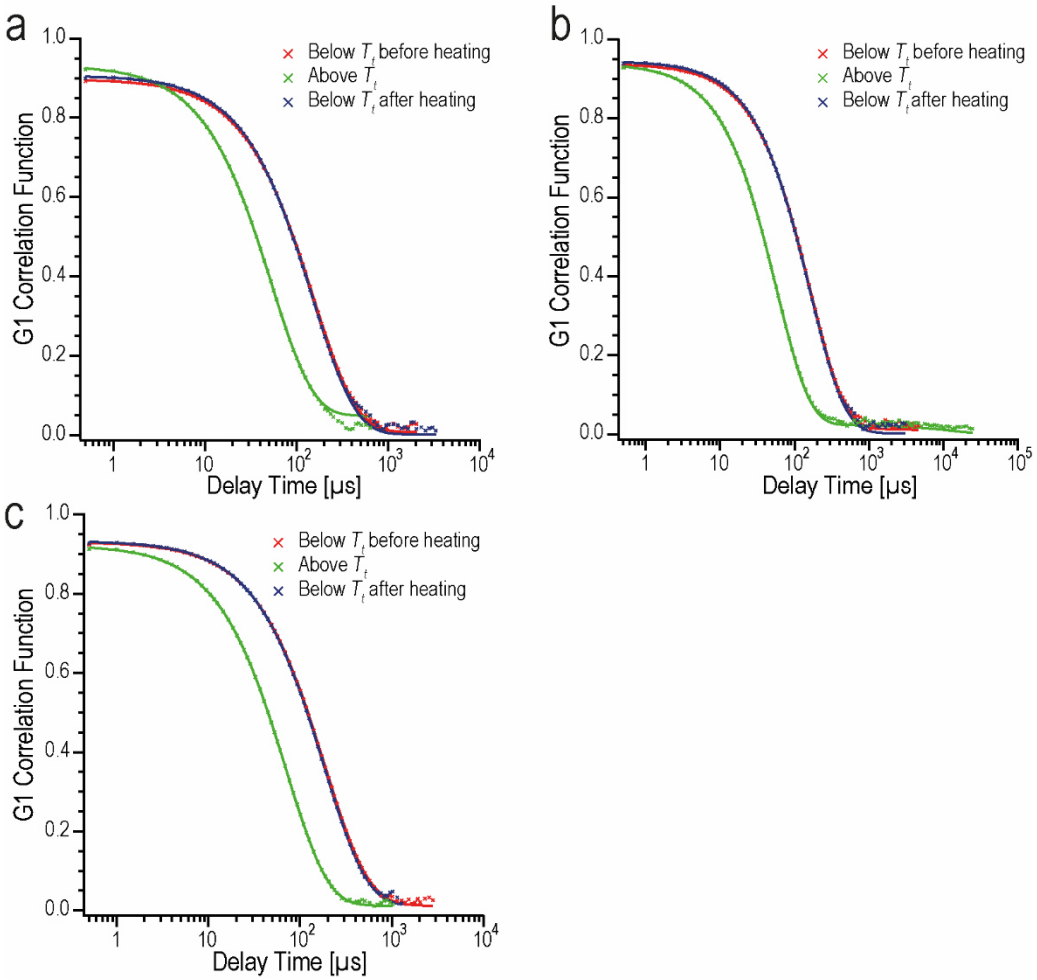

Figure Appendix 3: Correlation function from DLS heating cycle measurements on three ELP samples **(a-c)** with data points (crosses) and fit. Samples were measured below T_t before heating (red), above T_t (green) and below T_t after heating (blue).

The correlation data for ELP solutions spiked with FITC-labeled dextrans and NaCl can be seen in Figure Appendix 4. The NaCl containing sample shows several decays, which is indicative for a solution with several size populations.

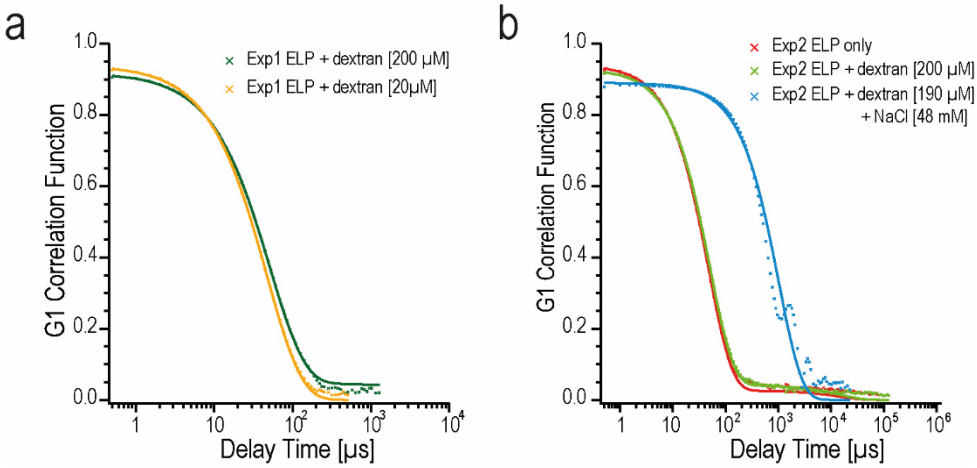

Figure Appendix 4: Correlation data for loading ELP nanoparticles before cross-link with **(a)** FITC-dextrans at different concentrations and **(b)** FITC-dextrans at different concentrations and one sample with additional NaCl at 48 mM. Graphs shows single data points (crosses) and fit line.

7.4. Nanoparticle synthesis – particle formation

Particle formation was tracked at three different protein concentrations, which was discussed in chapter 4.2.2 The temperature trend measurements were performed in temperature steps of 0.2 °C. The measurements were performed to track micelle assembly and the T_t was defined. This was done by tracking the transition of the main population of trimers below T_t and nanoparticles above T_t. It was observed that the main population was accompanied by the presence of larger aggregates. This is illustrated in Figure Appendix 5, where the transition is shown for samples with 4 - 5 µM, 20 µM and 60 µM protein concentration in a), b) and c) respectively.

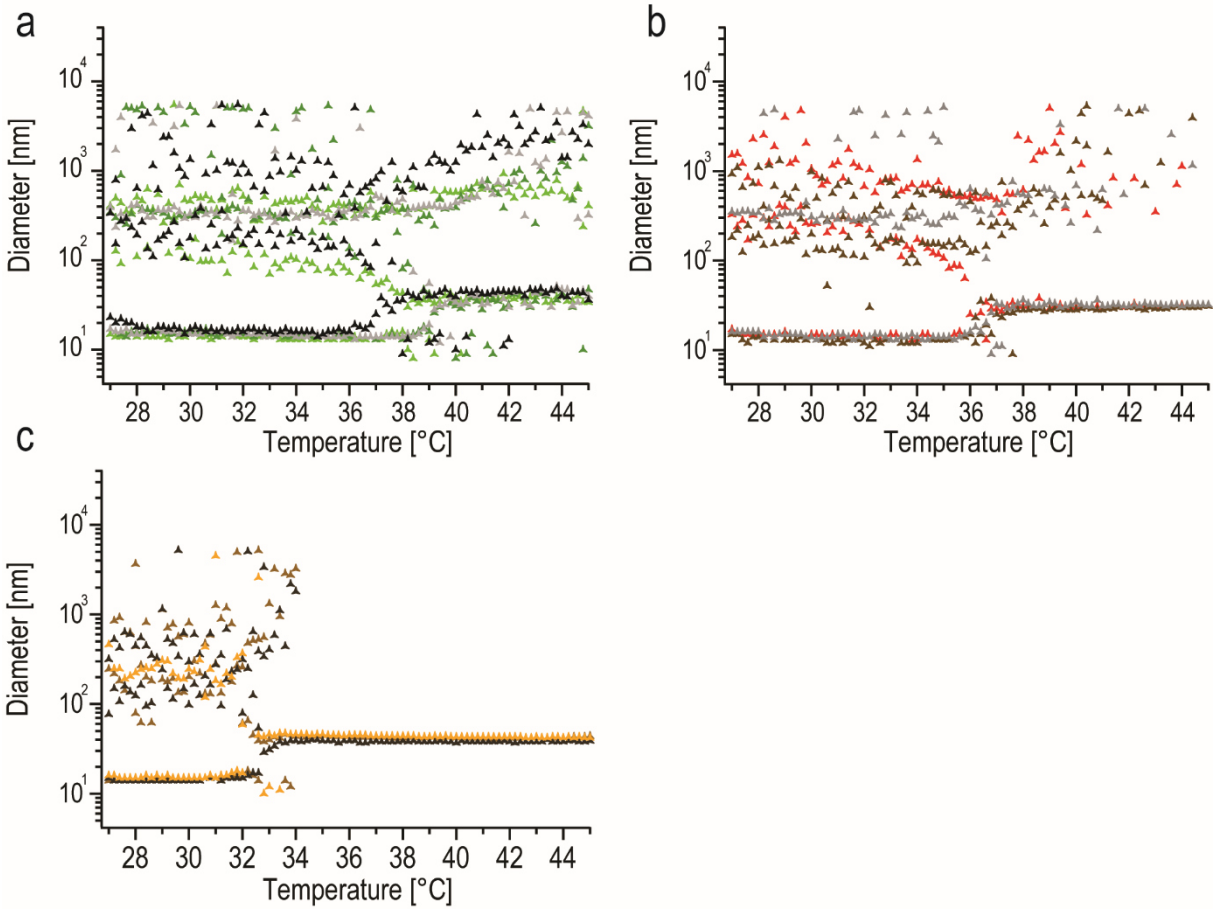

Figure Appendix 5: DLS-derived temperature trends from intensity-weighted size graphs for definition of T_t of micelle formation. Sizes were tracked in discrete temperature steps (0.2 °C) in the temperature range 27-45 °C. Protein concentrations were **(a)** 4-5 µM ELP fusion protein (0.1-0.3 mM phosphate buffer, pH 10-10.2), **(b)** 20 µM ELP fusion protein (0.4 mM phosphate buffer, pH 9.6-10.3) and **(c)** 60 µM ELP fusion protein (2-3 mM phosphate buffer, pH 10).

It was observed that the dominance of the side population decreased upon heating. This effect was more pronounced for samples with higher protein concentration. It remains to be elucidated why the temperature trend measurements showed a larger side population above T_t, especially samples with low protein concentration. This observance is in contrast to thermal cycling measurements which showed only the nanoparticle population when pH conditions were in a sufficiently basic pH range.

For clarity, the larger populations were excluded for further analysis in Figure Appendix 6, where only the population of interest is plotted against temperature.

The temperature trend measurements presented in chapter 4.2.2 did show the transition in the range 27 to 45 °C. In most cases the particle tracking was carried out up to 55°C where some deviations between different samples were observed in the upper temperature range.

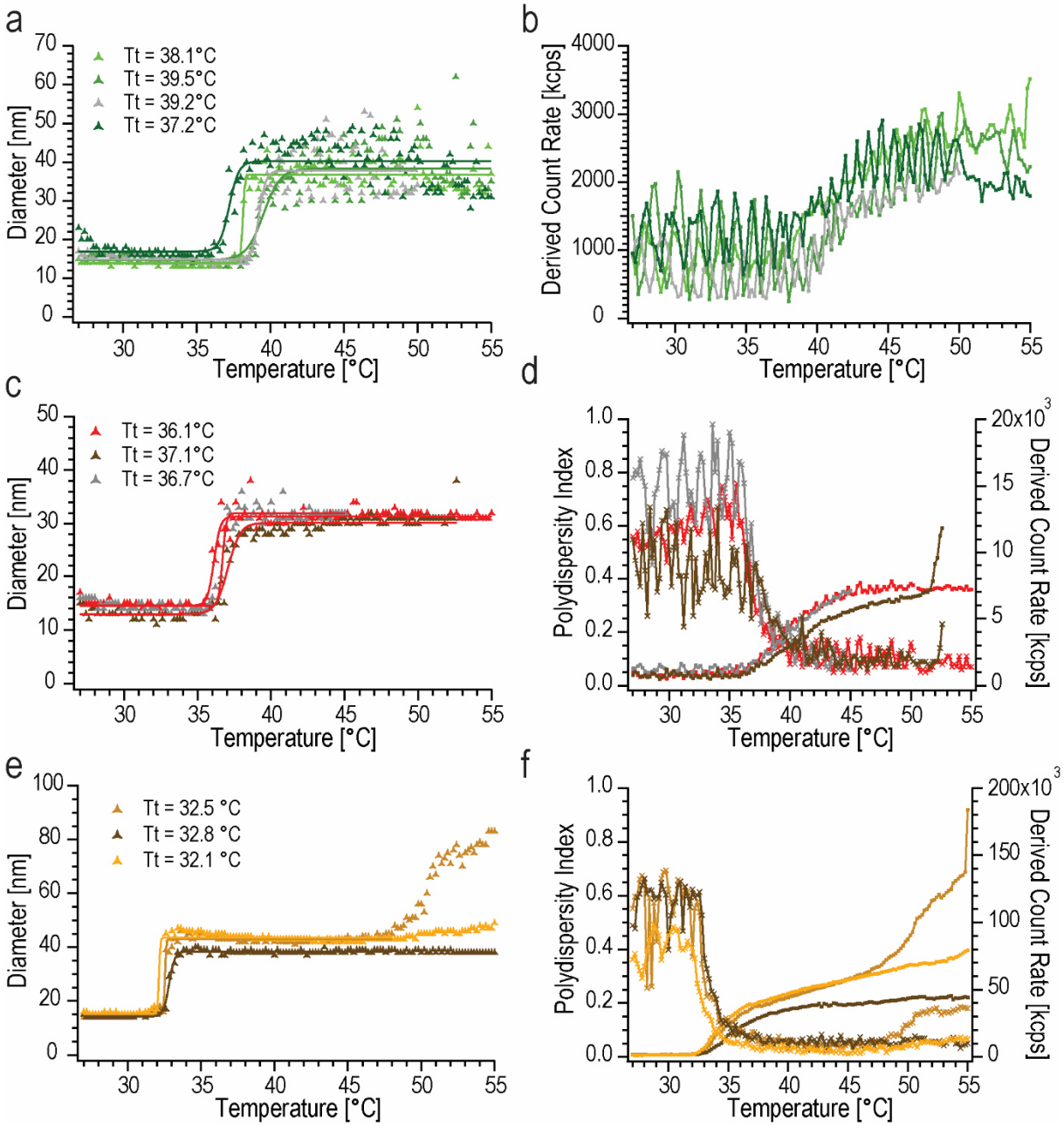

Figure Appendix 6: DLS temperature trends for definition of T_t of micelle formation. Sizes were tracked in discrete temperature steps (0.2 °C) in the temperature range 27-55 °C. Protein concentrations were **(a + b)** 4-5 µM ELP fusion protein (0.1-0.3 mM phosphate buffer, pH 10-10.2), **(c + d)** 20 µM ELP fusion protein (0.4 mM phosphate buffer, pH 9.6-10.3) and **(e + f)** 60 µM ELP fusion protein (2-3 mM phosphate buffer, pH 10). The left column **(a + c + e)** shows mean particle sizes of the population of interest, while the right column **(b + d + f)** shows the derived count rate for all samples of all concentrations and polydispersity index for 20 µM and 60 µM protein samples.

The second incline might have been caused by differences in water loss upon prolonged measurement. Figure Appendix 6 shows the transition for the three different concentrations (4-5 µM, 20 µM and 60 µM). Some of the presented samples of higher protein concentration show a second increase in the derived count rate. A second incline in particle size was observed for a sample of 60 µM and a sample with 20 µM protein concentration. This might have been caused

by an additional loss of water during the long heating time of approximately 24 h. Temperature trends for samples with 20 µM protein concentration were tracked up to a temperature of 55 °C, 52.6 °C and 45 °C.

It has been reported by other studies that ELP coacervates show an additional slow extrusion of water above 60 °C [174]. This resulted in a separated phase with increased protein concentration (68 % w/v) [174]. The effect observed here may be caused by a similar behavior.

7.5. Cross-link condition variations

Nanoparticle cross-linking was also achieved when the cross-linker was dissolved in MES buffer (10 mM MES, 100 mM NaCl, pH 6.9), followed by the 1:10 (v/v) dilution in H_2O_{dd}. In a similar manner, the use of diluted ELP stocks that had been brought into PBS after purification were also applicable. In these experiments it was observed that additional NaCl could lead to larger particle sizes and was thus left out of the reaction. Moreover, it has been reported elsewhere that nanoparticle formation is responsive to variations in salt concentration [286]. It was assumed that there is a cutoff NaCl concentration above which larger assemblies will result. Some additional preliminary experiments involved the dilution of cross-linker in H_2O_{dd} or standard buffer, where the results obtained were less reproducible and some particle solutions had a higher PI. It was followed that the buffering capacity of MES was needed for the cross-link reaction. The benefit of MES over phosphate buffer in this cross-linking approach may be a result of its minor charge.

Cross-linking of an ELP construct containing several lysines was tested, which in several cases resulted in turbid solutions after the addition of bis-NHS-PEG linkers (2kDa). Such larger aggregation forms might be a result of non-optimized buffering conditions during the cross-link reaction or interparticle cross-link events via lysines in the foldon headgroup. Comparatively, a different study reported that ELP cross-linking can be more difficult if the polymer features a high charge density, due to its higher sensitivity against salts [177]. This can be challenging when nanoparticles are to be cross-linked that can only form in the absence of charges in their interior, as is the case for the nanoparticles presented in this work. It was concluded that ELP constructs without additional charges facilitated more consistent results in cross-linking. It was assumed that, if potential charges in the ELP chain were neutralized by suitable pH conditions and salt conditions optimized, also cross-linking of other constructs may be possible.

7.6. Cross-linked nanoparticles on cartilage

Experiments on nanoparticle diffusion in cartilage were carried out together with Joanna Urban. Cartilage preparation was carried out by Joanna Urban.

A few preliminary studies were carried out to test whether the nanoparticle characteristics facilitated their diffusion into cartilage tissue. For this, cross-linked nanoparticles were labeled with Atto647N or DyLight™ 594 in separate experiments. Cartilage slices were prepared as described below, incubated in the nanoparticle solutions and subsequently visualized via confocal imaging.

The first study involved the application of Atto647N-labeled nanoparticles on slices of cartilage. Figure Appendix 7 shows the corresponding intensity-weighted DLS graph for nanoparticles for the cartilage experiment shown in Figure Appendix 8 b). The graphs prove thermal switching behavior in the usual size range before labeling.

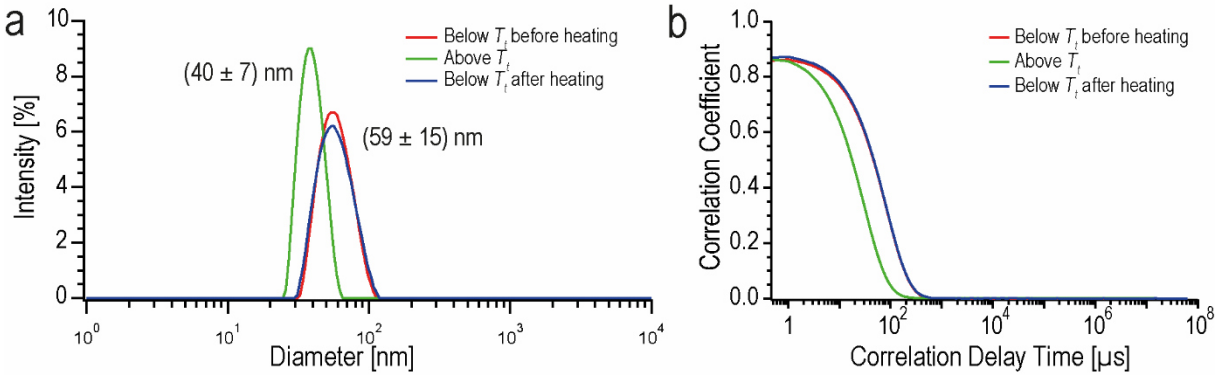

Figure Appendix 7: DLS-derived **(a)** diameters with **(b)** corresponding correlation functions of nanoparticles before labeling.

Cartilage slices were incubated for approximately 1h with the nanoparticle solution or incubated o/n. Images after nanoparticle incubation are shown in Figure Appendix 8 a + b) respectively. The images show the fluorescence channel where fluorescence detection was λ_{exc} = 633 nm, λ_{em} = 649-689 nm in Figure Appendix 8 a) and λ_{exc} = 633 nm, λ_{em} = 659-679 nm in Figure Appendix 8 b). It can be seen that in both cases, labeled nanoparticles diffused into the cartilage tissue and showed the tendency to adsorb in the cartilage lacunae, the areas of chondrocyte cells in the cartilage matrix [349].

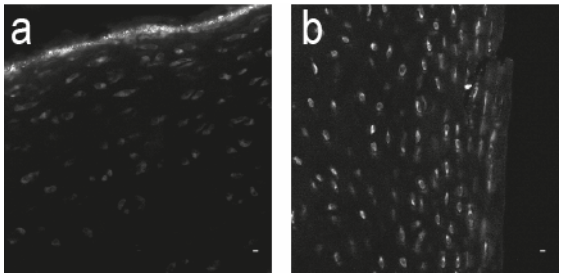

Figure Appendix 8: Confocal images showing fluorescence emission in the wavelength range corresponding to Atto647N fluorescence. Slice of articular cartilage after incubation with ELP-based nanoparticles labeled with Atto647N. **(a)** After incubation for 1:10 h with nanoparticles in phosphate buffer (10 mM, pH7.3). Fluorescence was observed via λ_{exc} = 633 nm, λ_{em} = 649-689 nm. **(b)** after o/n incubation with nanoparticles in standard buffer (pH8.2). Fluorescence was observed via λ_{exc} = 33 nm, λ_{em} = 659-679 nm.

The particle adsorption in the first image might be an effect of particle aggregation which was observed in this sample. The diminished solution homogeneity might have been caused by the slightly different buffer conditions with a pH of 7.3. It was assumed that the increased permeability for nanoparticles and their accumulation in the cartilage lacunae might be an effect of tissue damage upon storage at -20°C before use. To exclude such side effects, the experiment was repeated with cartilage that had not been stored at -20°C (see sample preparation 2). The nanoparticles in this experiment were labeled with DyLight^{TM} 594 and loaded with FITC-dextrans (4kDa) as described in the sample preparation 2 below. The result is shown in Figure Appendix 9 where FITC-dextran fluorescence detection is shown in a) and red fluorescence for particle detection is shown in b). The respective fluorescence channels for a control sample, originating from a different cartilage sample before nanoparticle application, is shown in c + d).

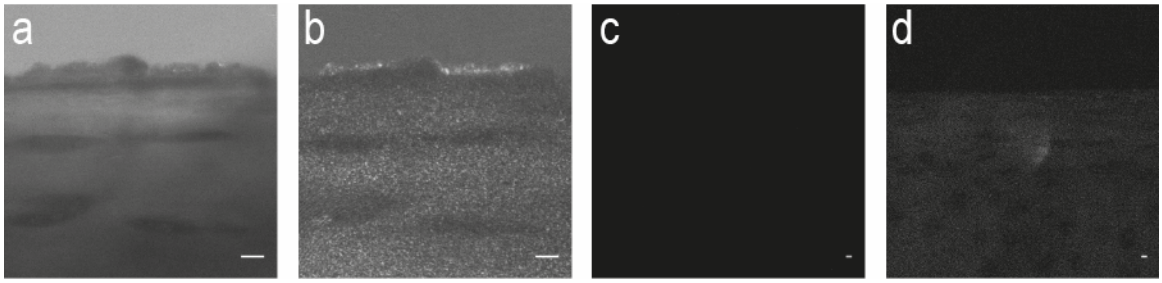

Figure Appendix 9: Confocal images showing fluorescence emission in the wavelength range corresponding to **(a + c)** FITC-dextran fluorescence (λ_{exc} = 488 nm, λ_{em} = 500-550 nm) and **(b + d)** DyLight^{TM} 594 fluorescence (λ_{exc} = 633 nm, λ_{em} = 653-695 nm). **(a + b)** Slice of articular cartilage after o/n incubation with ELP-based nanoparticles that carried DyLight^{TM} 594 label and were loaded with FITC-dextrans (4kDa). **(c + d)** Control measurement showing another cartilage sample before the addition of nanoparticles.

In fact, this experiment lacked any accumulation of particles in the cell structures. Instead, particles appeared to accumulate on the tissue surface. Aggregation effects that were observable in these cartilage studies might be salt-induced when particles got into contact with residual PBS buffer, which was used for cartilage incubation before nanoparticle incubation in order to provide physiological conditions. Some fluorescence from FITC-dextrans can be seen in the extracellular matrix (ECM). It remains to be elucidated whether FITC dextrans in the ECM originated from already unloaded molecules diffusing from solution into the tissue or whether they were carried by nanoparticle diffusion into the matrix (dialysis time after particle loading and cross-link should be increased). The control sample in Figure Appendix 9 c + d) reveals a low background signal in the red channel. This hinders a definite assignment of the ECM-associated red fluorescence in Figure Appendix 9 b) to the nanoparticles.

As this experiment was carried out one single time, a definite conclusion cannot be made. However, the results presented open a new highly interesting field of study: The adaption of surface characteristics, such as charge, or of particle size might lead to an increased diffusion of particles into the cartilage tissue. Future studies could elucidate where the particles tend to accumulate, which could vary with additional surface coatings. The experimental design might further be expanded to the study of heat-triggered release of loaded agents (smaller than FITC-dextrans with a MW of 4000 g/mol).

In context with literature:

Other studies [341, 346] have approached the difficulties in drug administration into cartilage tissue, which is of importance for osteoarthritis treatment. The ECM texture restricts applicable polymer sizes to below 60 nm due to the collagen network, further complicated by the presence of proteoglycans further restricting spaces in the ECM, and the absence of vascular tissue [341]. Both studies [341, 346] hinted at the potential of small carrier systems: An increased diffusion of small micelles (15 nm diameter) [346] and nanoparticles with a mean diameter of 38 nm [341] into cartilage tissue was shown. The increased diffusivity was explained by their small size while an increased association of the particles with the cartilage was achieved by modification of surface characteristics. The approach of exploiting the effects of surface charge for cartilage diffusion studies, as for example treated in Bajpayee et al. [350], might also be useful in the adaption of the presented particle system for cartilage applications.

Sample preparation for study1:

Cartilage preparation: The cartilage samples were harvested from the knee joint of the hind leg of 3-6 months old lambs. The joints with closed articular joint capsules were obtained from a local slaughterhouse a day after animal sacrifice and frozen at -20°C. Before sample preparation, the joints were defrosted o/n at 4°C. Osteochondral cylinders with a diameter of 8 mm were drilled out of the patellofemoral grove and rinsed in PBS buffer.

Nanoparticle labeling:

Experiment 1: Cross-linked nanoparticles were dialyzed against standard buffer, as described in 3.2.5 and subsequently labeled. Labeling with Atto647N-NHS was carried out as described in 3.2.8 (experiment 1). The DOL for the sample used in the cartilage study was defined to 5 %.

***Experiment* 2:** Cross-linked nanoparticles were dialyzed against standard buffer, as described in 3.2.5 and subsequently labeled. Labeling with Atto647N-NHS was carried out as described in 3.2.8 (experiment 4). Dialysis was carried out twice o/n at 43 °C, 70 rpm. The DOL was defined to 6 %.

Incubation of cartilage with nanoparticles: The cartilage samples were incubated in a solution of cross-linked nanoparticles at RT o/n. For imaging, the sample was extracted from the solution and excess fluid was gently soaked up while avoiding touching the sample surface. The cartilage was separated from the bone, cut perpendicularly to the articular surface and placed on a microscope slide with the freshly cut surface facing downwards. A drop of buffer was pipetted from the side of the articular surface to prevent the sample from drying out. The other sides were protected from drying by silicone rubber. The proceeding in sample preparation and final arrangement for measurement is depicted in Figure Appendix 10.

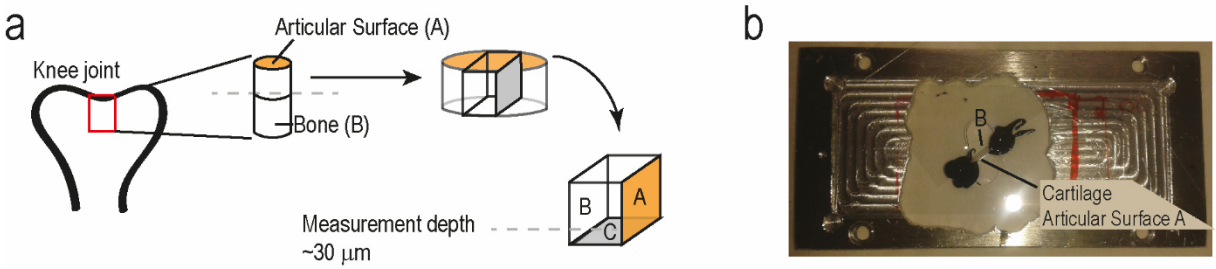

Figure Appendix 10: Preparation scheme of cartilage for confocal imaging. **(a)** Osteochondral cylinders with 8 mm diameter were drilled out from the patellofemoral grove and separated from the bone and a cut perpendicularly to the articular surface. The sample was placed on a microscope slide with the freshly cut surface facing downwards. **(b)** Final arrangement of cartilage sample on microscope slide. A drop of buffer was pipetted from the side of the articular surface to prevent drying. The sample was fixed with silicone rubber which protected the other sides from drying out.

Sample preparation for study2:

Cartilage preparation: The cartilage samples were harvested from the knee joint of the hind leg of 3-6 months old lambs. The joints with closed articular joint capsules were obtained from a local slaughterhouse a day after animal sacrifice.

Trimer labeling: Trimer labeling was carried out with the dye DyLight™ 594 (Thermo Fisher Scientific) which was freshly dissolved in DMSO before use. The dye solution was added to 35 µM protein in standard buffer, leading to a final dye concentration of 6.2 µM. The reaction mixture was incubated rotating at RT for 2 h. This was followed by dialysis o/n at RT against 1.5 L standard buffer with Pur-A-Lyzer Maxi dialysis devices (12 kDa MWCO, Sigma-Aldrich).

Nanoparticle loading: For micelle formation and cross-link, the labeled trimers were mixed with unlabeled trimers in a 1:7 (v/v) ratio. A stock solution of neutral FITC-labeled dextrans with a MW of 4 kDa (Sigma Aldrich) was prepared (2 mM in standard buffer). The stock was added to the protein solution, leading to a final dye concentration of 133 µM. Solutions were dialyzed against standard buffer at RT for around 7 h with Pur-A-Lyzer Maxi dialysis devices (12 kDa MWCO, Sigma-Aldrich) in order to remove excess FITC-labeled dextrans.

Incubation of cartilage with nanoparticles: The solution of cross-linked nanoparticles was applied on the sample and incubated at RT o/n. Further sample preparation was carried out as outlined above and illustrated in Figure Appendix 10.

7.7. Loading labeled ELP nanoparticles

Control sample of FITC dextrans only

The control sample of FITC-dextrans for the experimental set in chapter 4.6.3 is presented in Figure Appendix 11. The dialyzed sample proves the absence of nanoparticles.

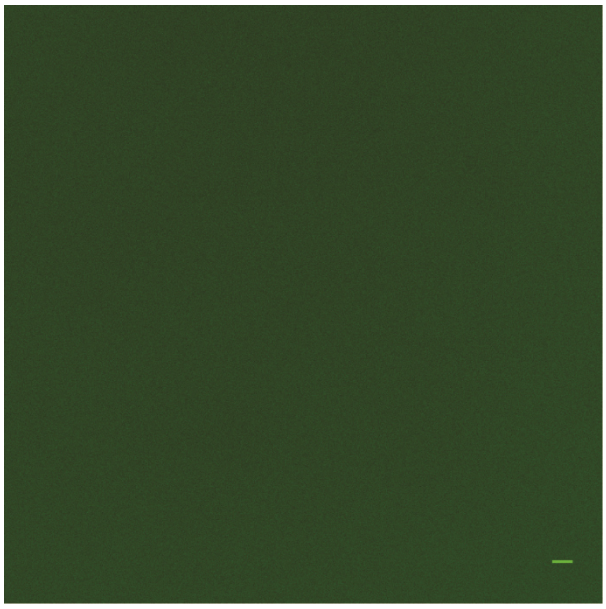

Figure Appendix 11: Control sample for colocalization studies, showing a solution of FITC-dextrans only, after dialysis. It serves as proof for the absence of particles and not for quantitative fluorescence definition. Reprinted with permission from B. Kracke et al., 2015, Macromolecules 48, 5868-5877, Copyright © 2015 American Chemical Society [125].

The control serves as proof for the absence of particles and not for a quantitative evaluation. An overall green signal might account for detector noise or residual FITC-dextrans due to incomplete dialysis.

Effect of temperature on loaded particles

In a succeeding study it was tested in one experiment whether the temperature during dialysis had an effect on FITC-dextran-loaded ELP nanoparticles. The particles were loaded with FITC-dextrans before cross-link and dialysis was carried out above and below T_t, with results shown in Figure Appendix 12 a-c) and d-f) respectively.

It can be seen that particles remain loaded with FITC-dextrans, irrespective of dialysis temperature. It may be concluded that the FITC-labeled dextrans used were of such high MW that the molecules did exceed particle 'pore size'. However, it cannot be excluded that some expulsion or diffusion-controlled release did occur above or below T_t. Furthermore, dialysis time in this preliminary study was relatively short (5 hours above T_t and 6 hours below T_t) and thus the experiment only serves as first insight into particle loading characteristics. Furthermore, it has to be noticed that dialysis devices used were different, which may influence dialysis efficiency. Experiment conditions may be optimized in terms of the MW and concentration of loaded molecules and dialysis conditions.

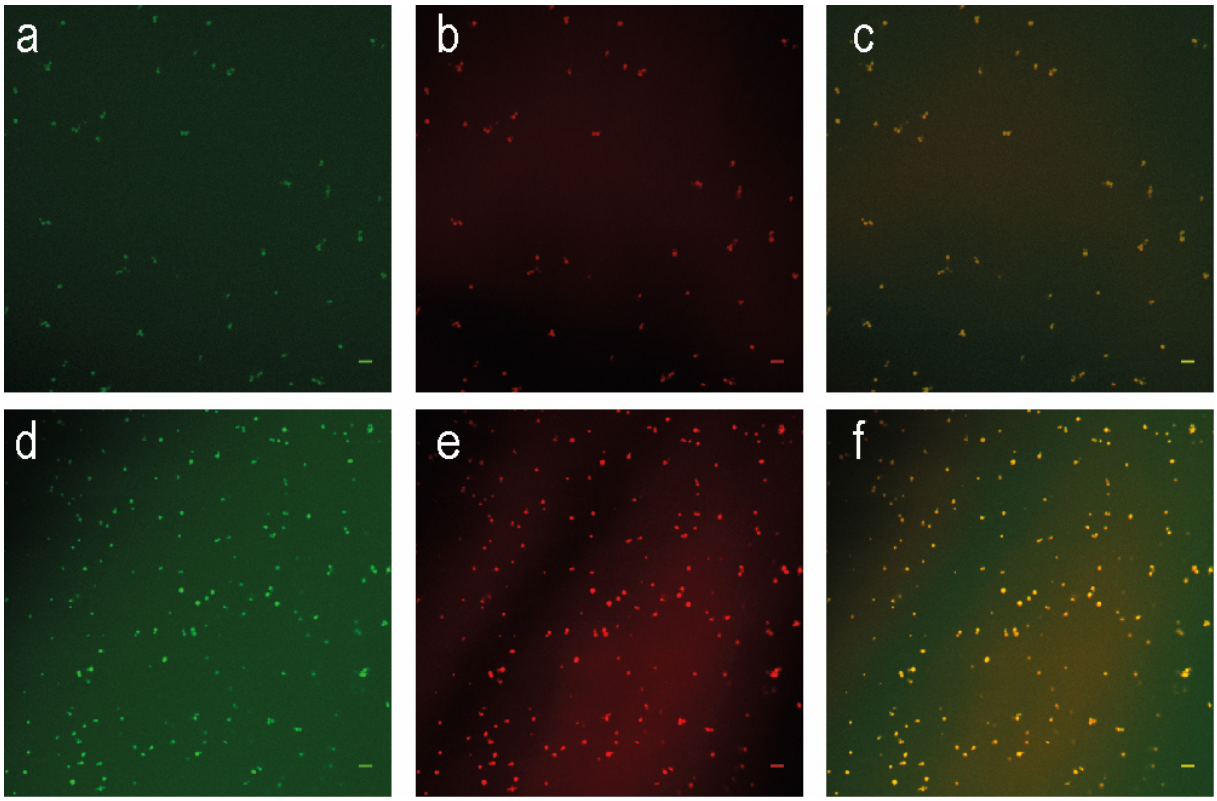

Figure Appendix 12: DL594-labeled ELP nanoparticles loaded with FITC-dextran (4kDa). Solutions were dialyzed **(a-c)** above T_t and **(d-f)** below T_t. **(a + d)** Fluorescence excitation of FITC-dextrans (λ_{ex} = 488 nm, λ_{em} = 500-550 nm) and **(b + e)** DL594 label (λ_{ex} = 633 nm, λ_{em} = 653-695 nm) with **(c + f)** overlay of both signals.

Sample preparation

A stock solution of ELP trimers was prepared (19 µM, pH 9.8) and micelle formation was proved via DLS. The solution was mixed with DL594-labeled trimers in a 7:1 (v/v) ratio. The solution was aliquoted and FITC-dextrans were added to the nanoparticle solution in a 1:9 (v/v) ratio. The solution was spiked with NaCl to give a final salt concentration of 32 mM. Samples were dialyzed below T_t (6h, RT, around 70 rpm) with Pur-A-Lyzer Maxi dialysis devices (12 kDa MWCO, Sigma-Aldrich) or above T_t (5 h, 43 °C, 70 rpm) with Slide-A-Lyzer MINI dialysis devices (Thermo Fisher Scientific) with a cutoff membrane of 20 kDa.

8. References

1. Ringsdorf, H. Structure and properties of pharmacologically active polymers. *Journal of polymer science: Polymer symposia* **51,** 135–153 (1975).
2. Torchilin, V. P. Micellar Nanocarriers: Pharmaceutical Perspectives. *Pharmaceutical Research* **24,** 1–16 (2007).
3. Maham, A., Tang, Z., Wu, H., Wang, J. & Lin, Y. Protein-based nanomedicine platforms for drug delivery. *Small* **5,** 1706–1721 (2009).
4. Jones, M.-C. & Leroux, J.-C. Polymeric micelles – a new generation of colloidal drug carriers. *European Journal of Pharmaceutics and Biopharmaceutics* **48,** 101–111 (1999).
5. Riess, G. Micellization of block copolymers. *Progress in Polymer Science* **28,** 1107–1170 (2003).
6. Zamboni, W. C. Liposomal, nanoparticle, and conjugated formulations of anticancer agents. *Clinical Cancer Research* **11,** 8230–8234 (2005).
7. Sauer, M. & Meier, W. Responsive nanocapsules. *Chemical Communications* **1,** 55–56 (2001).
8. Somiya, M. & Kuroda, S. Development of a virus-mimicking nanocarrier for drug delivery systems: The bio-nanocapsule. *Advanced Drug Delivery Reviews* **95,** 77–89 (2015).
9. Douglas, T. & Young, M. Host-guest encapsulation of materials by assembled virus protein cages. *Nature* **393,** 152–155 (1998).
10. Ren, Y., Wong, S. M. & Lim, L.-Y. Folic Acid-Conjugated Protein Cages of a Plant Virus. A Novel Delivery Platform for Doxorubicin. *Bioconjugate chemistry* **18,** 836–843 (2007).
11. Bromley, E. H. C., Channon, K., Moutevelis, E. & Woolfson, D. N. Peptide and Protein Building Blocks for Synthetic Biology: From Programming Biomolecules to Self-Organized Biomolecular Systems. ACS Chemical Biology. *ACS Chem. Biol.* **3,** 38–50 (2008).
12. Torchilin, V. P. & Trubetskoy, V. S. Which polymers can make nanoparticulate drug carriers long-circulating? *Advanced Drug Delivery Reviews* **16,** 141–155 (1995).
13. Albanese, A., Tang, P. S. & Chan, W. C. The Effect of Nanoparticle Size, Shape, and Surface Chemistry on Biological Systems. *Annual review of biomedical engineering* **14,** 1–16 (2012).
14. Luxenhofer, R. *et al.* Doubly amphiphilic poly(2-oxazoline)s as high-capacity delivery systems for hydrophobic drugs. *Biomaterials* **31,** 4972–4979 (2010).
15. Han, Y. *et al.* Synergistic combinations of multiple chemotherapeutic agents in high capacity poly(2-oxazoline) micelles. *Molecular pharmaceutics* **9,** 2302–2313 (2012).

16. Duncan, R. The dawning era of polymer therapeutics. *Nature reviews. Drug discovery* **2,** 347–360 (2003).

17. Desai, M. P., Labhasetwar, V., Amidon, G. L. & Levy, R. J. Gastrointestinal Uptake of Biodegradable Microparticles: Effect of Particle Size. *Pharmaceutical Research* **13,** 1838–1845 (1996).

18. Davis, M. E., Chen, Z. G. & Shin, D. M. Nanoparticle therapeutics: an emerging treatment modality for cancer. *Nature reviews. Drug discovery* **7,** 771–782 (2008).

19. Zhang, S., Li, J., Lykotrafitis, G., Bao, G. & Suresh, S. Size-Dependent Endocytosis of Nanoparticles. *Advanced Materials* **21,** 419–424 (2009).

20. Chithrani, B. D., Ghazani, A. A. & Chan, W. C. W. Determining the Size and Shape Dependence of Gold Nanoparticle Uptake into Mammalian Cells. *Nano Letters* **6,** 662–668 (2006).

21. Osaki, F., Kanamori, T., Sando, S., Sera, T. & Aoyama, Y. A Quantum Dot Conjugated Sugar Ball and Its Cellular Uptake. On the Size Effects of Endocytosis in the Subviral Region. *Journal of the American Chemical Society* **126,** 6520–6521 (2004).

22. Yuan, F. *et al.* Vascular Permeability in a Human Tumor Xenograft: Molecular Size Dependence and Cutoff Size. *Cancer Research* **55,** 3752–3756 (1995).

23. Hobbs, S. K. *et al.* Regulation of transport pathways in tumor vessels: Role of tumor type and microenvironment. *Proceedings of the National Academy of Sciences of the United States of America* **95,** 4607–4612 (1998).

24. Matsumura, Y. & Maeda, H. A New Concept for Macromolecular Therapeutics in Cancer Chemotherapy: Mechanism of Tumoritropic Accumulation of Proteins and the Antitumor Agent Smancs. *Cancer Research* **46,** 6387–6392 (1986).

25. Maeda, H., Wu, J., Sawa, T., Matsumura, Y. & Hori, K. Tumor vascular permeability and the EPR effect in macromolecular therapeutics: a review. *Journal of Controlled Release* **65,** 271–284 (2000).

26. Haag, R. & Kratz, F. Polymer Therapeutics: Concepts and Applications. *Angewandte Chemie International Edition* **45,** 1198–1215 (2006).

27. Strebhardt, K. & Ullrich, A. Paul Ehrlich's magic bullet concept. 100 years of progress. *Nature Reviews Cancer* **8,** 473–480 (2008).

28. Allen, T. M. Ligand-targeted therapeutics in anticancer therapy. *Nature Reviews Cancer* **2,** 750–763 (2002).

29. Ju, X.-J., Xie, R., Yang, L. & Chu, L.-Y. Biodegradable 'intelligent' materials in response to physical stimuli for biomedical applications. *Expert opinion on therapeutic patents* **19,** 493–507 (2009).

30. Mano, J. F. Stimuli-Responsive Polymeric Systems for Biomedical Applications. *Advanced Engineering Materials* **10,** 515–527 (2008).

31. Cabane, E., Zhang, X., Langowska, K., Palivan, C. G. & Meier, W. Stimuli-responsive polymers and their applications in nanomedicine. *Biointerphases* **7,** 1–27 (2012).

32. Stuart, M. A. C. *et al.* Emerging applications of stimuli-responsive polymer materials. *Nature materials* **9,** 101–113 (2010).

33. Ganta, S., Devalapally, H., Shahiwala, A. & Amiji, M. A review of stimuli-responsive nanocarriers for drug and gene delivery. *Journal of Controlled Release* **126,** 187–204 (2008).

34. Rapoport, N. Physical stimuli-responsive polymeric micelles for anti-cancer drug delivery. *Progress in Polymer Science* **32,** 962–990 (2007).

35. Rijcken, C. J. F., Soga, O., Hennink, W. E. & van Nostrum, C. F. Triggered destabilisation of polymeric micelles and vesicles by changing polymers polarity: an attractive tool for drug delivery. *Journal of Controlled Release* **120,** 131–148 (2007).

36. Hu, F.-Q., Ren, G.-F., Yuan, H., Du, Y.-Z. & Zeng, S. Shell cross-linked stearic acid grafted chitosan oligosaccharide self-aggregated micelles for controlled release of paclitaxel. *Colloids and surfaces. B, Biointerfaces* **50,** 97–103 (2006).

37. Ghoorchian, A., Cole, J. T. & Holland, N. B. Thermoreversible Micelle Formation Using a Three-Armed Star Elastin-like Polypeptide. *Macromolecules* **43,** 4340–4345 (2010).

38. Wike-Hooley, J. L., Haveman, J. & Reinhold, H. S. The relevance of tumour pH to the treatment of malignant disease. *Radiotherapy and Oncology* **2,** 343–366 (1984).

39. Okano, T., Bae, Y. H., Jacobs, H. & Kim, S. W. Thermally on-off switching polymers for drug permeation and release. *Journal of Controlled Release* **11,** 255–265 (1990).

40. Chen, W.-Q. *et al.* Fabrication of star-shaped, thermo-sensitive poly(N-isopropylacrylamide)–cholic acid–poly(ε-caprolactone) copolymers and their self-assembled micelles as drug carriers. *Polymer* **49,** 3965–3972 (2008).

41. Abulateefeh, S. R. *et al.* Facile synthesis of responsive nanoparticles with reversible, tunable and rapid thermal transitions from biocompatible constituents. *Chemical Communications,* 6068–6070 (2009).

42. Jeong, B., Bae, Y. H., Lee, D. S. & Kim, S. W. Biodegradable block copolymers as injectable drug-delivery systems. *Nature* **388,** 860–862 (1997).

43. Partridge, S. M. in *Advances in Protein Chemistry,* edited by C.B. Anfinsen, Kenneth Bailey, M.L. Anson and John T. Edsall (Academic Press1963), pp. 227–302.

44. Ross, R. & Bornstein, P. Elastic fibers in the body. *Scientific American* **224,** 44–52 (1971).

45. Rosenbloom, J., Abrams, W. R. & Mecham, R. Extracellular matrix 4: the elastic fiber. *The FASEB Journal* **7,** 1208–1218 (1993).

46. Chrzanowski, P., Keller, S., Cerreta, J., Mandl, I. & Turino, G. M. Elastin content of normal and emphysematous lung parenchyma. *The American Journal of Medicine* **69,** 351–359 (1980).

47. Gosline, J. M. The physical properties of elastic tissue. *International review of connective tissue research* **7,** 211–249 (1976).

48. Daamen, W. F., Veerkamp, J. H., van Hest, J C M & van Kuppevelt, T. H. Elastin as a biomaterial for tissue engineering. *Biomaterials* **28,** 4378–4398 (2007).

49. Urry, D. W., Long, M. M., Harris, R. D. & Prasad, K. U. Temperature-correlated force and structure development in elastomeric polypeptides: The Ile1 analog of the polypentapeptide of elastin. *Biopolymers* **25,** 1939–1953 (1986).

50. Sandberg, L. B., Soskel, N. T. & Leslie, J. G. Elastin structure, biosynthesis, and relation to disease states. *The New England journal of medicine* **304,** 566–579 (1981).

51. Martyn, C. & Greenwald, S. A Hypothesis About A Mechanism For The Programming Of Blood Pressure And Vascular Disease In Early Life. *Clinical and Experimental Pharmacology and Physiology* **28,** 948–951 (2001).

52. Smith, D. W., Weissman, N. & Carnes, W. H. Cardiovascular studies on copper deficient swine. XII. Partial purification of a soluble protein resembling elastin. *Biochemical and Biophysical Research Communications* **31,** 309–315 (1968).

53. Sandberg, L. B., Weissman, N. & Smith, D. W. The purification and partial characterization of a soluble elastin-like protein from copper-deficient porcine aorta. *Biochemistry* **8,** 2940–2945 (1969).

54. Smith, D. W., Brown, D. M. & Carnes, W. H. Preparation and Properties of Salt-soluble Elastin. *The Journal of biological chemistry* **247,** 2427–2432 (1972).

55. Foster, J. A., Bruenger, E., Gray, W. R. & Sandberg, L. B. Isolation and Amino Acid Sequences of Tropoelastin Peptides. *The Journal of biological chemistry* **248,** 2876–2879 (1973).

56. Urry, D. W. *et al.* Elastin: a representative ideal protein elastomer. *Philosophical transactions of the Royal Society of London. Series B, Biological sciences* **357,** 169–184 (2002).

57. Urry, D. W. Physical Chemistry of Biological Free Energy Transduction As Demonstrated by Elastic Protein-Based Polymers †. *The Journal of Physical Chemistry B* **101,** 11007–11028 (1997).

58. Ribeiro, A., Arias, F. J., Reguera, J., Alonso, M. & Rodríguez-Cabello, J. C. Influence of the amino-acid sequence on the inverse temperature transition of elastin-like polymers. *Biophysical journal* **97,** 312–320 (2009).

59. Urry, D. W. Free energy transduction in polypeptides and proteins based on inverse temperature transitions. *Progress in Biophysics and Molecular Biology* **57,** 23–57 (1992).

60. Rapaka, R. S., Okamoto, K. & Urry, D. W. Coacervation properties in sequential polypeptide models of elastin. *International Journal of Peptide and Protein Research* **12,** 81–92 (1978).

61. Urry, D. W. & Prasad, K. U. in *Biocompatibility of tissue analogs,* edited by D. F. Williams (CRC Press, Boca Raton, Fla., 1985), pp. 89–116.

62. Manno, M. *et al.* Interaction of processes on different length scales in a bioelastomer capable of performing energy conversion. *Biopolymers* **59,** 51–64 (2001).

63. Meyer, D. E. & Chilkoti, A. Genetically Encoded Synthesis of Protein-Based Polymers with Precisely Specified Molecular Weight and Sequence by Recursive Directional Ligation. Examples from the Elastin-like Polypeptide System. *Biomacromolecules* **3,** 357–367 (2002).

64. Huang, L. *et al.* Generation of Synthetic Elastin-Mimetic Small Diameter Fibers and Fiber Networks. *Macromolecules* **33,** 2989–2997 (2000).

65. Meyer, D. E. & Chilkoti, A. Purification of recombinant proteins by fusion with thermally-responsive polypeptides. *Nature biotechnology* **17,** 1112–1115 (1999).

66. McPherson, D. T., Xu, J. & Urry, D. W. Product purification by reversible phase transition following Escherichia coli expression of genes encoding up to 251 repeats of the elastomeric pentapeptide GVGVP. *Protein expression and purification* **7,** 51–57 (1996).

67. Lim, D. W., Trabbic-Carlson, K., Mackay, J. A. & Chilkoti, A. Improved non-chromatographic purification of a recombinant protein by cationic elastin-like polypeptides. *Biomacromolecules* **8,** 1417–1424 (2007).

68. Urry, D. W., Parker, T. M., Reid, M. C. & Gowda, D. C. Biocompatibility of the Bioelastic Materials, Poly(GVGVP) and Its -Irradiation Cross-Linked Matrix. Summary of Generic Biological Test Results. *Journal of Bioactive and Compatible Polymers* **6,** 263–282 (1991).

69. Sallach, R. E. *et al.* Long-term biostability of self-assembling protein polymers in the absence of covalent crosslinking. *Biomaterials* **31,** 779–791 (2010).

70. Rincón, A. C. *et al.* Biocompatibility of elastin-like polymer poly(VPAVG) microparticles: in vitro and in vivo studies. *Journal of Biomedical Materials Research Part A* **78A,** 343–351 (2006).

71. Nettles, D. L., Chilkoti, A. & Setton, L. A. Applications of elastin-like polypeptides in tissue engineering. *Advanced Drug Delivery Reviews* **62,** 1479–1485 (2010).

72. Shah, M. *et al.* Biodegradation of elastin-like polypeptide nanoparticles. *Protein science* **21,** 743–750 (2012).

73. Urry, D. W. Entropic elastic processes in protein mechanisms. I. Elastic structure due to an inverse temperature transition and elasticity due to internal chain dynamics. *Journal of Protein Chemistry* **7,** 1–34 (1988).

74. Patel, A., Fine, B., Sandig, M. & Mequanint, K. Elastin biosynthesis: The missing link in tissue-engineered blood vessels. *Cardiovascular research* **71,** 40–49 (2006).

75. Di Zio, K. & Tirrell, D. A. Mechanical Properties of Artificial Protein Matrices Engineered for Control of Cell and Tissue Behavior. *Macromolecules* **36,** 1553–1558 (2003).

76. Caves, J. M. *et al.* The use of microfiber composites of elastin-like protein matrix reinforced with synthetic collagen in the design of vascular grafts. *Biomaterials* **31,** 7175–7182 (2010).

77. Woodhouse, K. A. *et al.* Investigation of recombinant human elastin polypeptides as non-thrombogenic coatings. *Biomaterials* **25,** 4543–4553 (2004).

78. Jordan, S. W. *et al.* The effect of a recombinant elastin-mimetic coating of an ePTFE prosthesis on acute thrombogenicity in a baboon arteriovenous shunt. *Biomaterials* **28,** 1191–1197 (2007).

79. Urry, D. W. Elastic molecular machines in metabolism and soft-tissue restoration. *Trends in Biotechnology* **17,** 249–257 (1999).

80. Caves, J. M. *et al.* Elastin-like protein matrix reinforced with collagen microfibers for soft tissue repair. *Biomaterials* **32,** 5371–5379 (2011).

81. Urry, D. W. *et al.* Elastic protein-based polymers in soft tissue augmentation and generation. *Journal of Biomaterials Science, Polymer Edition* **9,** 1015–1048 (1998).

82. Nicol, A., Gowda, C. & Urry, D. W. Elastic protein-based polymers as cell attachment matrices. *Journal of Vascular Surgery* **13,** 746–748 (1991).

83. Nicol, A., Gowda, D. C. & Urry, D. W. Cell adhesion and growth on synthetic elastomeric matrices containing Arg-Gly-Asp-Ser-3. *Journal of biomedical materials research* **26,** 393–413 (1992).

84. Hoban, L. D. *et al.* Use of polypentapeptides of elastin to prevent postoperative adhesions: efficacy in a contaminated peritoneal model. *Journal of surgical research* **56,** 179–183 (1994).

85. Pierschbacher, M. D. & Ruoslahti, E. Cell attachment activity of fibronectin can be duplicated by small synthetic fragments of the molecule. *Nature* **309,** 30–33 (1984).

86. Ruoslahti, E. & Pierschbacher, M. D. New perspectives in cell adhesion. RGD and integrins. *Science* **238,** 491–497 (1987).

87. Liu, J. C. & Tirrell, D. A. Cell response to RGD density in cross-linked artificial extracellular matrix protein films. *Biomacromolecules* **9,** 2984–2988 (2008).

88. Ravi, S., Krishnamurthy, V. R., Caves, J. M., Haller, C. A. & Chaikof, E. L. Maleimide-thiol coupling of a bioactive peptide to an elastin-like protein polymer. *Acta Biomaterialia* **8,** 627–635 (2012).

89. Adams, S. B., Shamji, M. F., Nettles, D. L., Hwang, P. & Setton, L. A. Sustained release of antibiotics from injectable and thermally responsive polypeptide depots. *Journal of biomedical materials research* **90B,** 67–74 (2009).

90. Peppas, N. A. & Langer, R. New challenges in biomaterials. *Science* **263,** 1715–1720 (1994).

91. Langer, R. & Tirrell, D. A. Designing materials for biology and medicine. *Nature* **428,** 487–492 (2004).

92. Lutolf, M. P. & Hubbell, J. A. Synthetic biomaterials as instructive extracellular microenvironments for morphogenesis in tissue engineering. *Nature biotechnology* **23,** 47–55 (2005).

93. Na, K. *et al.* "Smart" biopolymer for a reversible stimuli-responsive platform in cell-based biochips. *Langmuir* **24,** 4917–4923 (2008).

94. Nath, N. & Chilkoti, A. Creating “Smart” Surfaces Using Stimuli Responsive Polymers. *Advanced Materials* **14,** 1243–1247 (2002).

95. Jung, Y., Bayley, H. & Movileanu, L. Temperature-responsive protein pores. *Journal of the American Chemical Society* **128,** 15332–15340 (2006).

96. Mackay, J. A. *et al.* Self-assembling chimeric polypeptide-doxorubicin conjugate nanoparticles that abolish tumours after a single injection. *Nature materials* **8,** 993–999 (2009).

97. Meyer, D. E., Kong, G. A., Dewhirst, M. W., Zalutsky, M. R. & Chilkoti, A. Targeting a Genetically Engineered Elastin-like Polypeptide to Solid Tumors by Local Hyperthermia. *Cancer Research* **61,** 1548–1554 (2001).

98. Raucher, D. & Chilkoti, A. Enhanced Uptake of a Thermally Responsive Polypeptide by Tumor Cells in Response to Its Hyperthermia-mediated Phase Transition. *Cancer Research* **61,** 7163–7170 (2001).

99. Chilkoti, A., Dreher, M. R. & Meyer, D. E. Design of thermally responsive, recombinant polypeptide carriers for targeted drug delivery. *Advanced Drug Delivery Reviews* **54,** 1093–1111 (2002).

100. Dreher, M. R. *et al.* Temperature triggered self-assembly of polypeptides into multivalent spherical micelles. *Journal of the American Chemical Society* **130,** 687–694 (2008).

101. Simnick, A. J., Valencia, C. A., Liu, R. & Chilkoti, A. Morphing Low-Affinity Ligands into High-Avidity Nanoparticles by Thermally Triggered Self-Assembly of a Genetically Encoded Polymer. *ACS Nano* **4,** 2217–2227 (2010).

102. Hassouneh, W. *et al.* Unexpected Multivalent Display of Proteins by Temperature Triggered Self-Assembly of Elastin-like Polypeptide Block Copolymers. *Biomacromolecules* **13,** 1598–1605 (2012).

103. McDaniel, J. R., Callahan, D. J. & Chilkoti, A. Drug delivery to solid tumors by elastin-like polypeptides. *Advanced Drug Delivery Reviews* **62,** 1456–1467 (2010).

104. Lee, T. A. T., Cooper, A., Apkarian, R. P. & Conticello, V. P. Thermo-Reversible Self-Assembly of Nanoparticles Derived from Elastin-Mimetic Polypeptides. *Advanced Materials* **12,** 1105–1110 (2000).

105. Fujita, Y., Mie, M. & Kobatake, E. Construction of nanoscale protein particle using temperature-sensitive elastin-like peptide and polyaspartic acid chain. *Biomaterials* **30,** 3450–3457 (2009).

106. Wright, E. R. & Conticello, V. P. Self-assembly of block copolymers derived from elastin-mimetic polypeptide sequences. *Advanced Drug Delivery Reviews* **54,** 1057–1073 (2002).

107. Sallach, R. E. *et al.* Micelle density regulated by a reversible switch of protein secondary structure. *Journal of the American Chemical Society* **128,** 12014–12019 (2006).

108. Bae, Y., Buresh, R. A., Williamson, T. P., Chen, T.-H. H. & Furgeson, D. Y. Intelligent biosynthetic nanobiomaterials for hyperthermic combination chemotherapy and thermal drug targeting of HSP90 inhibitor geldanamycin. *Journal of Controlled Release* **122,** 16–23 (2007).

109. Martín, L., Castro, E., Ribeiro, A., Alonso, M. & Rodríguez-Cabello, J. C. Temperature-Triggered Self-Assembly of Elastin-Like Block Co-Recombinamers. The Controlled Formation of Micelles and Vesicles in an Aqueous Medium. *Biomacromolecules* **13,** 293–298 (2012).

110. van Eldijk, M. B. *et al.* Designing Two Self-Assembly Mechanisms into One Viral Capsid Protein. *Journal of the American Chemical Society* **134,** 18506–18509 (2012).

111. Janib, S. M. *et al.* A quantitative recipe for engineering protein polymer nanoparticles. *Polymer Chemistry* **5,** 1614–1625 (2014).

112. van Eldijk, M. B. *et al.* Synthesis and Self-Assembly of Well-Defined Elastin-Like Polypeptide–Poly(ethylene glycol) Conjugates. *Biomacromolecules* **15,** 2751–2759 (2014).

113. Herrero-Vanrell, R. *et al.* Self-assembled particles of an elastin-like polymer as vehicles for controlled drug release. *Journal of Controlled Release* **102,** 113–122 (2005).

114. Bessa, P. C. *et al.* Thermoresponsive self-assembled elastin-based nanoparticles for delivery of BMPs. *Journal of Controlled Release* **142,** 312–318 (2010).

115. Dash, B. C. *et al.* Tunable elastin-like polypeptide hollow sphere as a high payload and controlled delivery gene depot. *Journal of Controlled Release* **152,** 382–392 (2011).

116. Shi, P. *et al.* Elastin-based protein polymer nanoparticles carrying drug at both corona and core suppress tumor growth in vivo. *Journal of Controlled Release* **171,** 330–338 (2013).

117. Na, K., Jung, J., Lee, J. & Hyun, J. Thermoresponsive pore structure of biopolymer microspheres for a smart drug carrier. *Langmuir* **26,** 11165–11169 (2010).

118. Fujimoto, M., Hara, M., Hayashi, T. & Furuta, M. Effect of heating process on the formation of nanoparticles of elastin model polypeptide, (GVGVP)251, by gamma-ray crosslinking. *Polymer Bulletin* **64,** 707–716 (2010).

119. Urry, D. W. *et al. in Tissue engineering and novel delivery systems,* edited by M. J. Yaszemski (Marcel Dekker, New York, NY, 2004), pp. 31–54.

120. McMillan, R. A. & Conticello, V. P. Synthesis and Characterization of Elastin-Mimetic Protein Gels Derived from a Well-Defined Polypeptide Precursor. *Macromolecules* **33,** 4809–4821 (2000).

121. Sun, G., Hsueh, P.-Y., Janib, S. M., Hamm-Alvarez, S. & Andrew MacKay, J. Design and cellular internalization of genetically engineered polypeptide nanoparticles displaying adenovirus knob domain. *Journal of Controlled Release* **155,** 218–226 (2011).

122. Kim, W., Thévenot, J., Ibarboure, E., Lecommandoux, S. & Chaikof, E. L. Self-assembly of thermally responsive amphiphilic diblock copolypeptides into spherical micellar nanoparticles. *Angewandte Chemie (International ed. in English)* **49,** 4257–4260 (2010).

123. Fujita, Y., Funabashi, H., Mie, M. & Kobatake, E. Design of a thermocontrollable protein complex. *Bioconjugate chemistry* **18,** 1619–1624 (2007).

124. Yamaoka, T. *et al.* Mechanism for the phase transition of a genetically engineered elastin model peptide (VPGIG)40 in aqueous solution. *Biomacromolecules* **4,** 1680–1685 (2003).

125. Kracke, B. *et al.* Thermoswitchable Nanoparticles Based on Elastin-like Polypeptides. *Macromolecules* **48,** 5868–5877 (2015).

126. Venkatachalam, C. M. & Urry, D. W. Development of a linear helical conformation from its cyclic correlate. β-Spiral model of the elastin poly(pentapeptide) (VPGVG)n. *Macromolecules* **14,** 1225–1229 (1981).

127. Güthe, S. *et al.* Very fast folding and association of a trimerization domain from bacteriophage T4 fibritin. *Journal of Molecular Biology* **337,** 905–915 (2004).

128. Tao, Y., Strelkov, S. V., Mesyanzhinov, V. V. & Rossmann, M. G. Structure of bacteriophage T4 fibritin. A segmented coiled coil and the role of the C-terminal domain. *Structure* **5,** 789–798 (1997).

129. Coombs, D. H. & Eiserling, F. A. Studies on the structure, protein composition and assembly of the neck of bacteriophage T4. *Journal of Molecular Biology* **116,** 375–405 (1977).

130. Wood, W. B. & Conley, M. P. Attachment of tail fibers in bacteriophage T4 assembly. Role of the phage whiskers. *Journal of Molecular Biology* **127,** 15–29 (1979).

131. Conley, M. P. & Wood, W. B. Bacteriophage T4 whiskers: a rudimentary environment-sensing device. *Proceedings of the National Academy of Sciences of the United States of America* **72,** 3701–3705 (1975).

132. Strelkov, S. V. *et al.* Preliminary crystallographic studies of bacteriophage T4 fibritin confirm a trimeric coiled-coil structure. *Virology* **219,** 190–194 (1996).

133. Letarov, A. V., Londer, Y. Y., Boudko, S. P. & Mesyanzhinov, V. V. The carboxy-terminal domain initiates trimerization of bacteriophage T4 fibritin. *Biochemistry (Moscow)* **64,** 817–823 (1999).

134. Yu, M. H. & King, J. Single amino acid substitutions influencing the folding pathway of the phage P22 tail spike endorhamnosidase. *Proceedings of the National Academy of Sciences of the United States of America* **81,** 6584–6588 (1984).

135. Boudko, S. P. *et al.* Domain organization, folding and stability of bacteriophage T4 fibritin, a segmented coiled-coil protein. *European Journal of Biochemistry* **269,** 833–841 (2002).

136. Efimov, V. P. *et al.* Fibritin Encoded by Bacteriophage T4 Gene wac has a Parallel Triple-stranded α-Helical Coiled-coil Structure. *Journal of Molecular Biology* **242,** 470–486 (1994).

137. Frank, S. *et al.* Stabilization of short collagen-like triple helices by protein engineering. *Journal of Molecular Biology* **308,** 1081–1089 (2001).

138. Stetefeld, J. *et al.* Collagen Stabilization at Atomic Level: Crystal structure of designed (GlyProPro)10foldon. *Structure* **11,** 339–346 (2003).

139. Du, C. *et al.* Improvement of thermostability of recombinant collagen-like protein by incorporating a foldon sequence. *Applied Microbiology and Biotechnology* **79,** 195–202.

140. Bhardwaj, A., Walker-Kopp, N., Wilkens, S. & Cingolani, G. Foldon-guided self-assembly of ultra-stable protein fibers. *Protein science* **17,** 1475–1485 (2008).

141. Yang, X. *et al.* Highly Stable Trimers Formed by Human Immunodeficiency Virus Type 1 Envelope Glycoproteins Fused with the Trimeric Motif of T4 Bacteriophage Fibritin. *Journal of Virology* **76,** 4634–4642 (2002).

142. Papanikolopoulou, K., Forge, V., Goeltz, P. & Mitraki, A. Formation of highly stable chimeric trimers by fusion of an adenovirus fiber shaft fragment with the foldon domain of bacteriophage T4 fibritin. *The Journal of biological chemistry* **279,** 8991–8998 (2004).

143. Papanikolopoulou, K. *et al.* Adenovirus fibre shaft sequences fold into the native triple beta-spiral fold when N-terminally fused to the bacteriophage T4 fibritin foldon trimerisation motif. *Journal of Molecular Biology* **342,** 219–227 (2004).

144. Sissoëff, L., Mousli, M., England, P. & Tuffereau, C. Stable trimerization of recombinant rabies virus glycoprotein ectodomain is required for interaction with the p75NTR receptor. *Journal of general virology* **86,** 2543–2552 (2005).

145. Strelkov, S. V., Tao, Y., Shneider, M. M., Mesyanzhinov, V. V. & Rossmann, M. G. Structure of Bacteriophage T4 Fibritin M: A Troublesome Packing Arrangement. *Acta Crystallographica Section D Biological Crystallography* **54,** 805–816 (1998).

146. Meier, S., Güthe, S., Kiefhaber, T. & Grzesiek, S. Foldon, the natural trimerization domain of T4 fibritin, dissociates into a monomeric A-state form containing a stable beta-hairpin: atomic details of trimer dissociation and local beta-hairpin stability from residual dipolar couplings. *Journal of Molecular Biology* **344,** 1051–1069 (2004).

147. Berg, J. M., Tymoczko, J. L. & Stryer, L. *Biochemie.* 6th ed. (Elsevier Spektrum Akad. Verl., München, 2007).

148. Heskins, M. & Guillet, J. E. Solution Properties of Poly(N-isopropylacrylamide). *Journal of Macromolecular Science: Part A - Chemistry* **2,** 1441–1455 (1968).

149. Gil, E. S. & Hudson, S. M. Stimuli-reponsive polymers and their bioconjugates. *Progress in Polymer Science* **29,** 1173–1222 (2004).

150. Luan, C. H., Harris, R. D., Prasad, K. U. & Urry, D. W. Differential scanning calorimetry studies of the inverse temperature transition of the polypentapeptide of elastin and its analogues. *Biopolymers* **29,** 1699–1706 (1990).

151. Urry, D. W., Khaled, M. A., Rapaka, R. S. & Okamoto, K. Nuclear overhauser enhancement evidence for inverse temperature dependence of hydrophobic side chain proximity in the polytetrapeptide of tropoelastin. *Biochemical and Biophysical Research Communications* **79,** 700–706 (1977).

152. Urry, D. W. *et al.* Temperature of polypeptide inverse temperature transition depends on mean residue hydrophobicity. *Journal of the American Chemical Society* **113,** 4346–4348 (1991).

153. Edsall, J. T. Apparent Molal Heat Capacities of Amino Acids and Other Organic Compounds. *Journal of the American Chemical Society* **57,** 1506–1507 (1935).

154. Butler, J. A. V. The energy and entropy of hydration of organic compounds. *Transactions of the Faraday Society* **33,** 229–236 (1937).

155. Frank, H. S. & Evans, M. W. Free Volume and Entropy in Condensed Systems III. Entropy in Binary Liquid Mixtures; Partial Molal Entropy in Dilute Solutions; Structure and Thermodynamics in Aqueous Electrolytes. *The Journal of Chemical Physics* **13,** 507–532 (1945).

156. KAUZMANN, W. Some factors in the interpretation of protein denaturation. *Advances in protein chemistry* **14,** 1–63 (1959).

157. Stackelberg, M. v. & Müller, H. R. Zur Struktur der Gashydrate. *Naturwissenschaften* **38,** 456 (1951).

158. Müller, H. R. & Stackelberg, M. v. Zur Struktur der Gashydrate. *Naturwissenschaften* **39,** 20–21 (1952).

159. Teeter, M. M. Water structure of a hydrophobic protein at atomic resolution: Pentagon rings of water molecules in crystals of crambin. *Proceedings of the National Academy of Sciences of the United States of America* **81,** 6014–6018 (1984).

160. Tanford, C. *The hydrophobic effect. Formation of micelles and biological membranes.* 2nd ed. (Wiley, New York, 1980).

161. Lee, J., Macosko, C. W. & Urry, D. W. Mechanical Properties of Cross-Linked Synthetic Elastomeric Polypentapeptides. *Macromolecules* **34,** 5968–5974 (2001).

162. Glaser, R. *Biophysik.* 4th ed. (Fischer, Jena, 1996).

163. Urry, D. W., Trapane, T. L. & Khaled, M. A. Temperature dependence of rotational correlation times for an inverse temperature transition. A fundamental characterization. *Journal of the American Chemical Society* **100,** 7744–7746 (1978).

164. Pace, C. N., Shirley, B. A., McNutt, M. & Gajiwala, K. Forces contributing to the conformational stability of proteins. *The FASEB Journal* **10,** 75–83 (1996).

165. Makhatadze, G. I. & Privalov, P. L. Energetics of protein structure. *Advances in protein chemistry* **47,** 307–425 (1995).

166. Israelachvili, J. N. *Intermolecular and surface forces.* 3rd ed. (Elsevier Academic Press, Amsterdam, 2011).

167. Roy, C. S. The Elastic Properties of the Arterial Wall. *The Journal of Physiology* **3,** 125–159 (1881).

168. Urry, D. W. Protein elasticity based on conformations of sequential polypeptides: The biological elastic fiber. *Journal of Protein Chemistry* **3,** 403–436 (1984).

169. Urry, D. W. *et al.* Hydrophobicity scale for proteins based on inverse temperature transitions. *Biopolymers* **32,** 1243–1250 (1992).

170. Urry, D. W. Five axioms for the functional design of peptide-based polymers as molecular machines and materials: Principle for macromolecular assemblies. *Biopolymers* **47,** 167–178 (1998).

171. Rodríguez-Cabello, J. *et al.* Endothermic and exothermic components of an inverse temperature transition for hydrophobic association by TMDSC. *Chemical Physics Letters* **388,** 127–131 (2004).

172. Urry, D. W., Peng, S. Q., Xu, J. & McPherson, D. T. Characterization of Waters of Hydrophobic Hydration by Microwave Dielectric Relaxation. *Journal of the American Chemical Society* **119,** 1161–1162 (1997).

173. Bellingham, C. M., Woodhouse, K. A., Robson, P., Rothstein, S. J. & Keeley, F. W. Self-aggregation characteristics of recombinantly expressed human elastin polypeptides. *Biochimica et Biophysica Acta (BBA) - Protein Structure and Molecular Enzymology* **1550,** 6–19 (2001).

174. Urry, D. W., Trapane, T. L. & Prasad, K. U. Phase-structure transitions of the elastin polypentapeptide-water system within the framework of composition-temperature studies. *Biopolymers* **24,** 2345–2356 (1985).

175. Urry, D. W. Molekulare Maschinen: Wie Bewegung und andere Funktionen lebender Organismen aus reversiblen chemischen Änderungen entstehen. *Angewandte Chemie* **105,** 859–883 (1993).

176. Urry, D. W. Molecular Machines: How Motion and Other Functions of Living Organisms Can Result from Reversible Chemical Changes. *Angewandte Chemie International Edition in English* **32,** 819–841 (1993).

177. Trabbic-Carlson, K., Setton, L. A. & Chilkoti, A. Swelling and mechanical behaviors of chemically cross-linked hydrogels of elastin-like polypeptides. *Biomacromolecules* **4,** 572–580 (2003).

178. Li, B., Alonso, D. O. V. & Daggett, V. The molecular basis for the inverse temperature transition of elastin. *Journal of Molecular Biology* **305,** 581–592 (2001).

179. Li, B., Alonso, D. O. V., Bennion, B. J. & Daggett, V. Hydrophobic Hydration Is an Important Source of Elasticity in Elastin-Based Biopolymers. *Journal of the American Chemical Society* **123,** 11991–11998 (2001).

180. Gross, P. C., Possart, W. & Zeppezauer, M. An alternative structure model for the polypentapeptide in elastin. *Zeitschrift für Naturforschung* **58 C,** 873–878 (2003).

181. Cook, W. J., Einspahr, H., Trapane, T. L., Urry, D. W. & Bugg, C. E. Crystal structure and conformation of the cyclic trimer of a repeat pentapeptide of elastin, cyclo-(L-valyl-L-prolylglycyl-L-valylglycyl)3. *Journal of the American Chemical Society* **102,** 5502–5505 (1980).

182. Venkatachalam, C. M., Khaled, M. A., Sugano, H. & Urry, D. W. Nuclear magnetic resonance and conformational energy calculations of repeat peptides of elastin. Conformational characterization of cyclopentadecapeptide cyclo-(L-Val-L-Pro-Gly-L-Val-Gly)3. *Journal of the American Chemical Society* **103,** 2372–2379 (1981).

183. Urry, D. W., Cunningham, W. D. & Ohnishi, T. Studies on the conformation and interactions of elastin. Proton magnetic resonance of the repeating pentapeptide. *Biochemistry* **13,** 609–616 (1974).

184. Urry, D. W. in *Extracellular matrix,* edited by L. W. Cunningham (Acad. Press, New York, NY, 1982), pp. 673–716.

185. Urry, D. W., Trapane, T. L., Sugano, H. & Prasad, K. U. Sequential polypeptides of elastin. Cyclic conformational correlates of the linear polypentapeptide. *J. Am. Chem. Soc.* **103,** 2080–2089 (1981).

186. Urry, D. W., Mitchell, L. W., Ohnishi, T. & Long, M. M. Proton and carbon magnetic resonance studies of the synthetic polypentapeptide of elastin. *Journal of Molecular Biology* **96,** 101–117 (1975).

187. Urry, D. W., Long, M. M. & Gross, E. Conformations of the Repeat Peptides of Elastin in Solution: An Application of Proton and Carbon-13 Magnetic Resonance to the Determination of Polypeptide Secondary Structure. *Critical Reviews in Biochemistry and Molecular Biology* **4,** 1–45 (1976).

188. Urry, D. W. A Molecular Theory of Ion-Conducting Channels: A Field-Dependent Transition Between Conducting and Nonconducting Conformations. *Proceedings of the National Academy of Sciences of the United States of America* **69,** 1610–1614 (1972).

189. Chou, P. Y. & Fasman, G. D. β-turns in proteins. *Journal of Molecular Biology* **115,** 135–175 (1977).

190. Maeda, I. *et al.* Structural requirements essential for elastin coacervation: favorable spatial arrangements of valine ridges on the three-dimensional structure of elastin-derived polypeptide (VPGVG)n. *Journal of peptide science* **17,** 735–743 (2011).

191. Urry, D. W. *et al.* Two-dimensional proton NMR studies on poly(VPGVG) and its cyclic conformational correlate, cyclo(VPGVG)3. *Biopolymers* **28,** 819–833 (1989).

192. Urry, D. W. What Is Elastin; What Is Not. *Ultrastructural Pathology* **4,** 227–251 (1983).

193. San Biagio, P. L., Madonia, F., Trapane, T. L. & Urry, D. W. The overlap of elastomeric polypeptide coils in solution required for single-phase initiation of elastogenesis. *Chemical Physics Letters* **145,** 571–574 (1988).

194. Volpin, D., Urry, D. W., Pasquali-Ronchetti, I. & Gotte, L. Studies by electron microscopy on the structure of coacervates of synthetic polypeptides of tropoelastin. *Micron (1969)* **7,** 193–198 (1976).

195. Gotte, L., Giro, M. G., Volpin, D. & Horne, R. W. The ultrastructural organization of elastin. *Journal of Ultrastructure Research* **46,** 23–33 (1974).

196. Gotte, L., Volpin, D., Horne, R. W. & Mammi, M. Electron microscopy and optical diffraction of elastin. *Micron (1969)* **7,** 95–102 (1976).

197. Cleary, E. G. & Cliff, W. J. The substructure of elastin. *Experimental and Molecular Pathology* **28,** 227–246 (1978).

198. Cox, B. A., Starcher, B. C. & Urry, D. W. Coacervation of α-elastin results in fiber formation. *Biochimica et Biophysica Acta (BBA) - Protein Structure* **317,** 209–213 (1973).

199. Cox, B. A., Starcher, B. C. & Urry, D. W. Coacervation of Tropoelastin Results in Fiber Formation. *The Journal of biological chemistry* **249,** 997–998 (1974).

200. Urry, D. W. The change in Gibbs free energy for hydrophobic association. Derivation and evaluation by means of inverse temperature transitions. *Chemical Physics Letters* **399,** 177–183 (2004).

201. Meyer, D. E. & Chilkoti, A. Quantification of the effects of chain length and concentration on the thermal behavior of elastin-like polypeptides. *Biomacromolecules* **5,** 846–851 (2004).

202. Urry, D. W., Harris, R. D. & Prasad, K. U. Chemical potential driven contraction and relaxation by ionic strength modulation of an inverse temperature transition. *Journal of the American Chemical Society* **110,** 3303–3305 (1988).

203. Luan, C. H., Parker, T. M., Prasad, K. U. & Urry, D. W. Differential scanning calorimetry studies of NaCl effect on the inverse temperature transition of some elastin-based polytetra-, polypenta-, and polynonapeptides. *Biopolymers* **31,** 465–475 (1991).

204. Reguera, J., Urry, D. W., Parker, T. M., McPherson, D. T. & Rodríguez-Cabello, J. C. Effect of NaCl on the exothermic and endothermic components of the inverse temperature transition of a model elastin-like polymer. *Biomacromolecules* **8,** 354–358 (2007).

205. Kunz, W., Henle, J. & Ninham, B. W. 'Zur Lehre von der Wirkung der Salze' (about the science of the effect of salts). Franz Hofmeister's historical papers. *Current Opinion in Colloid & Interface Science* **9,** 19–37 (2004).

206. Hippel, P. H. von & Wong, K.-Y. On the Conformational Stability of Globular Proteins: The effects of various electrolytes and nonelectrolytes on the thermal ribonuclease transition. *The Journal of biological chemistry* **240,** 3909–3923 (1965).

207. Cho, Y. *et al.* Effects of Hofmeister anions on the phase transition temperature of elastin-like polypeptides. *The journal of physical chemistry. B* **112,** 13765–13771 (2008).

208. Pattanaik, A., Channe Gowda, D. & Urry, D. W. Phosphorylation and dephosphorylation modulation of an inverse temperature transition. *Biochemical and Biophysical Research Communications* **178,** 539–545 (1991).

209. Nuhn, H. & Klok, H.-A. Secondary structure formation and LCST behavior of short elastin-like peptides. *Biomacromolecules* **9,** 2755–2763 (2008).

210. Ghoorchian, A. & Holland, N. B. Molecular architecture influences the thermally induced aggregation behavior of elastin-like polypeptides. *Biomacromolecules* **12,** 4022–4029 (2011).

211. Urry, D. W., Hayes, L. C., Channe Gowda, D. & Parker, T. M. Pressure effect on inverse temperature transitions: Biological implications. *Chemical Physics Letters* **182,** 101–106 (1991).

212. Urry, D. W., Hayes, L. C., Parker, T. M. & Dean Harris, R. Baromechanical transduction in a model protein by the ΔTt mechanism. *Chemical Physics Letters* **201,** 336–340 (1993).

213. Strzegowski, L. A., Bueno Martinez, M., Channe Gowda, D., Urry, D. W. & Tirrell, D. A. Photomodulation of the inverse temperature transition of a modified elastin poly(pentapeptide). *Journal of the American Chemical Society* **116,** 813–814 (1994).

214. Urry, D. W., Haynes, B., Zhang, H., Harris, R. D. & Prasad, K. U. Mechanochemical coupling in synthetic polypeptides by modulation of an inverse temperature transition. *Proceedings of the National Academy of Sciences of the United States of America* **85,** 3407–3411 (1988).

215. Urry, D. W. Free energy (chemomechanical) transduction in elastomeric polypeptides by chemical potential modulation of an inverse temperature transition. *International Journal of Quantum Chemistry* **34,** 235–245 (1988).

216. Urry, D. W., Peng, S. Q., Hayes, L., Jaggard, J. & Dean Harris, R. A new mechanism of mechanochemical coupling: stretch-induced increase in carboxyl pKa as a diagnostic. *Biopolymers* **30,** 215–218 (1990).

217. Urry, D. W. & Peng, S. Q. Nonlinear Mechanical Force Induced pKa Shifts: Implications for Efficiency of Conversion to Chemical Energy. *Journal of the American Chemical Society* **117,** 8478–8479 (1995).

218. Urry, D. W., Hayes, L. C., Channe Gowda, D., Harris, C. M. & Dean Harris, R. Reduction-driven polypeptide folding by the ΔTt mechanism. *Biochemical and Biophysical Research Communications* **188,** 611–617 (1992).

219. Urry, D. W., Chang, D.-K., Zhang, H. & Prasad, K. U. pK Shift of functional group in mechanochemical coupling due to hydrophobic effect: Evidence for an apolar-polar repulsion free energy in water. *Biochemical and Biophysical Research Communications* **153,** 832–839 (1988).

220. Urry, D. W. Entropic elastic processes in protein mechanisms. II. Simple (passive) and coupled (active) development of elastic forces. *Journal of Protein Chemistry* **7,** 81–114 (1988).

221. Tanford, C. The hydrophobic effect and the organization of living matter. *Science* **200,** 1012–1018 (1978).

222. Israelachvili, J. N., John Mitchell, D. & Ninham, B. W. Theory of self-assembly of lipid bilayers and vesicles. *Biochimica et Biophysica Acta (BBA) - Biomembranes* **470,** 185–201 (1977).

223. Israelachvili, J. N., John Mitchell, D. & Ninham, B. W. Theory of self-assembly of hydrocarbon amphiphiles into micelles and bilayers. *Journal of the Chemical Society, Faraday Transactions 2* **72,** 1525–1568 (1976).

224. Takeo, M. *Disperse systems* (Wiley-VCH, Weinheim, New York, Chichester, Brisbane, Singapore, Toronto, 1999).

225. Whitesides, G. M., Mathias, J. P. & Seto, C. T. Molecular self-assembly and nanochemistry: A chemical strategy for the synthesis of nanostructures. *Science* **254,** 1312–1319 (1991).

226. Verkleij, A. J., Kruyff, B. de, Ververgaert, P., Tocanne, J. F. & van Deenen, L. L. M. The influence of pH, Ca2+ and protein on the thermotropic behaviour of the negatively charged phospholipid, phosphatidylglycerol. *Biochimica et Biophysica Acta (BBA) - Biomembranes* **339,** 432–437 (1974).

227. Hotze, E. M., Phenrat, T. & Lowry, G. V. Nanoparticle aggregation: challenges to understanding transport and reactivity in the environment. *Journal of environmental quality* **39,** 1909–1924 (2010).

228. Leckband, D. & Israelachvili, J. Intermolecular forces in biology. *Quarterly reviews of biophysics* **34,** 105–267 (2001).

229. Israelachvili, J. Differences between non-specific and bio-specific, and between equilibrium and non-equilibrium, interactions in biological systems. *Quarterly reviews of biophysics* **38,** 331–337 (2005).

230. Hermanson, G. T. *Bioconjugate techniques.* 2nd ed. (Elsevier Academic Press, Amsterdam, 2008).

231. Derjaguin, B. & Landau, L. Theory of the stability of strongly charged lyophobic sols and of the adhesion of strongly charged particles in solution of electrolytes. *Acta Physicochimica URSS,* 633–662 (1941).

232. Verwey, E. J. W. & Overbeek, J. T. G. *Theory of the stability of lyophobic colloids* (Elsevier, Amsterdam, New York, 1948).

233. Min, Y., Akbulut, M., Kristiansen, K., Golan, Y. & Israelachvili, J. The role of interparticle and external forces in nanoparticle assembly. *Nature materials* **7,** 527–538 (2008).

234. Chen, K. L. & Elimelech, M. Influence of humic acid on the aggregation kinetics of fullerene (C60) nanoparticles in monovalent and divalent electrolyte solutions. *Journal of Colloid and Interface Science* **309,** 126–134 (2007).

235. Saleh, N. *et al.* Ionic Strength and Composition Affect the Mobility of Surface-Modified Fe0 Nanoparticles in Water-Saturated Sand Columns. *Environmental Science & Technology* **42,** 3349–3355 (2008).

236. Thomas He, Y., Wan, J. & Tokunaga, T. Kinetic stability of hematite nanoparticles: the effect of particle sizes. *Journal of Nanoparticle Research* **10,** 321–332 (2008).

237. Hahn, M. W., Abadzic, D. & O'Melia, C. R. Aquasols: On the Role of Secondary Minima. *Environmental Science & Technology* **38,** 5915–5924 (2004).

238. Vold, M. J. Van der Waals' attraction between anisometric particles. *Journal of Colloid Science* **9,** 451–459 (1954).

239. Gill, S. C. & Hippel, P. H. von. Calculation of protein extinction coefficients from amino acid sequence data. *Analytical Biochemistry* **182,** 319–326 (1989).

240. F. Lottspeich & J. W. Engels (eds.). *Bioanalytik* (Spektrum Akad. Verl., München, 2006).

241. Phelps, E. A. *et al.* Maleimide cross-linked bioactive PEG hydrogel exhibits improved reaction kinetics and cross-linking for cell encapsulation and in situ delivery. *Advanced Materials* **24,** 64-70, 2 (2012).

242. Smyth, D. G., Blumenfeld, O. O. & Konigsberg, W. Reactions of N -ethylmaleimide with peptides and amino acids. *Biochemical Journal* **91,** 589–595 (1964).

243. Gorin, G., Martic, P. A. & Doughty, G. Kinetics of the reaction of N-ethylmaleimide with cysteine and some congeners. *Archives of Biochemistry and Biophysics* **115,** 593–597 (1966).

244. Wong, S. S. & Jameson, D. M. *Chemistry of protein and nucleic acid cross-linking and conjugation.* 2nd ed. (CRC Press, Boca Raton, 2012).

245. Bednar, R. A. Reactivity and pH dependence of thiol conjugation to N-ethylmaleimide. Detection of a conformational change in chalcone isomerase. *Biochemistry* **29,** 3684–3690 (1990).

246. R. Pecora (ed.). *Dynamic light scattering. Applications of photon correlation spectroscopy* (Plenum Press, New York, 1985).

247. Pecora, R. Dynamic Light Scattering Measurement of Nanometer Particles in Liquids. *Journal of Nanoparticle Research* **2,** 123–131 (2000).

248. Thomas, J. C. The determination of log normal particle size distributions by dynamic light scattering. *Journal of Colloid and Interface Science* **117,** 187–192 (1987).

249. Winter, R., Noll, F. & Czeslik, C. *Methoden der biophysikalischen Chemie.* 2nd ed. (Vieweg + Teubner, Wiesbaden, 2011).

250. Koppel, D. E. Analysis of Macromolecular Polydispersity in Intensity Correlation Spectroscopy. The Method of Cumulants. *The Journal of Chemical Physics* **57,** 4814 (1972).

251. Grabowski, E. F. & Morrison, I. D. in *Measurement of suspended particles by quasi-elastic light scattering,* edited by B. E. Dahneke (Wiley, New York, 1983), pp. 199–236.

252. International Organization for Standardization. *Particle size analysis - Dynamic light scattering (DLS) , ,* https://www.iso.org/obp/ui/#iso:std:iso:22412:ed-1:v1:en (04.04.2016).

253. Kapanidis, A. N. *et al.* Alternating-Laser Excitation of Single Molecules. *Accounts of Chemical Research* **38,** 523–533 (2005).

254. Kudryavtsev, V. *et al.* Combining MFD and PIE for Accurate Single-Pair Förster Resonance Energy Transfer Measurements. *ChemPhysChem* **13,** 1060–1078 (2012).

255. Müller, B. K., Zaychikov, E., Bräuchle, C. & Lamb, D. C. Pulsed Interleaved Excitation. *Biophysical journal* **89,** 3508–3522 (2005).

256. Aragón, S. R. & Pecora, R. Fluorescence correlation spectroscopy as a probe of molecular dynamics. *The Journal of Chemical Physics* **64,** 1791–1803 (1976).

257. Schwille, P., Bieschke, J. & Oehlenschläger, F. Kinetic investigations by fluorescence correlation spectroscopy. The analytical and diagnostic potential of diffusion studies. *Biophysical Chemistry* **66,** 211–228 (1997).

258. Widengren, J., Rigler, R. & Mets, U. Triplet-state monitoring by fluorescence correlation spectroscopy. *Journal of fluorescence* **4,** 255–258 (1994).

259. Ratzke, C., Hellenkamp, B. & Hugel, T. Four-colour FRET reveals directionality in the Hsp90 multicomponent machinery. *Nature communications* **5,** 4192 (2014).

260. Binnig, G., Quate, C. F. & Gerber, C. Atomic Force Microscope. *Physical review letters* **56,** 930–933 (1986).

261. Meyer, G. & Amer, N. M. Erratum: Novel optical approach to atomic force microscopy. *Applied Physics Letters* **53,** 2400–2402 (1988).

262. Alexander, S. *et al.* An atomic-resolution atomic-force microscope implemented using an optical lever. *Journal of Applied Physics* **65,** 164–167 (1989).

263. Jandt, K. D. Atomic force microscopy of biomaterials surfaces and interfaces. *Surface Science* **491,** 303–332 (2001).

264. Zhong, Q., Inniss, D., Kjoller, K. & Elings, V. B. Fractured polymer/silica fiber surface studied by tapping mode atomic force microscopy. *Surface Science* **290,** L688-L692 (1993).

265. Hansma, P. K. *et al.* Tapping mode atomic force microscopy in liquids. *Applied Physics Letters* **64,** 1738–1740 (1994).

266. Putman, C. A. J., Van der Werf, Kees O., Grooth, B. G. de, van Hulst, N. F. & Greve, J. Tapping mode atomic force microscopy in liquid. *Applied Physics Letters* **64,** 2454–2456 (1994).

267. Magonov, S. N., Elings, V. & Whangbo, M.-H. Phase imaging and stiffness in tapping-mode atomic force microscopy. *Surface Science* **375,** L385-L391 (1997).

268. Martínez, N. F. & García, R. Measuring phase shifts and energy dissipation with amplitude modulation atomic force microscopy. *Nanotechnology* **17,** S167-S172 (2006).

269. Cleveland, J. P., Anczykowski, B., Schmid, A. E. & Elings, V. B. Energy dissipation in tapping-mode atomic force microscopy. *Applied Physics Letters* **72,** 2613–2615 (1998).

270. Berquand, A., Mazeran, P.-E. & Laval, J.-M. Influence of volume and surface properties on phase contrast in tapping mode atomic force microscopy. *Surface Science* **523,** 125–130 (2003).

271. Canet-Ferrer, J., Coronado, E., Forment-Aliaga, A. & Pinilla-Cienfuegos, E. Correction of the tip convolution effects in the imaging of nanostructures studied through scanning force microscopy. *Nanotechnology* **25,** 395703 (2014).

272. ATTO-TEC. Recommended Procedures For Labeling. Available at https://www.atto-tec.com/fileadmin/user_upload/Katalog_Flyer_Support/Procedures.pdf (22.07.2016).

273. Gabard, J. & Collet, A. Synthesis of a (D3)-bis(cyclotriveratrylenyl) macrocage by stereospecific replication of a (C3)-subunit. *Journal of the Chemical Society, Chemical Communications,* 1137–1139 (1981).

274. Bartik, K., Luhmer, M., Dutasta, J.-P., Collet, A. & Reisse, J. 129Xe and 1H NMR Study of the Reversible Trapping of Xenon by Cryptophane-A in Organic Solution. *Journal of the American Chemical Society* **120,** 784–791 (1998).

275. Huber, G. *et al.* Water Soluble Cryptophanes Showing Unprecedented Affinity for Xenon: Candidates as NMR-Based Biosensors. *Journal of the American Chemical Society* **128,** 6239–6246 (2006).

276. Swanson, S. D., Rosen, M. S., Coulter, K. P., Welsh, R. C. & Chupp, T. E. Distribution and dynamics of laser-polarized 129Xe magnetization in vivo. *Magnetic Resonance in Medicine* **42,** 1137–1145 (1999).

277. Berthault, P., Huber, G. & Desvaux, H. Biosensing using laser-polarized xenon NMR/MRI. *Progress in Nuclear Magnetic Resonance Spectroscopy* **55,** 35–60 (2009).

278. Glöggler, S. *et al.* Online Monitoring of Intelligent Polymers for Drug Release with Hyperpolarized Xenon. *ChemPhysChem* **13,** 4120–4123 (2012).

279. Schröder, L., Lowery, T. J., Hilty, C., Wemmer, D. E. & Pines, A. Molecular Imaging Using a Targeted Magnetic Resonance Hyperpolarized Biosensor. *Science* **314,** 446–449 (2006).

280. Sloniec, J. *et al.* Biomembrane Interactions of Functionalized Cryptophane-A: Combined Fluorescence and 129Xe NMR Studies of a Bimodal Contrast Agent. *Chemistry – A European Journal* **19,** 3110–3118 (2013).

281. Rubinstein, M. & Colby, R. H. *Polymer physics* (Oxford Univ. Press, Oxford, 2003).

282. Creighton, T. E. *Proteins. Structures and molecular properties.* 2nd ed. (Freeman, New York, 1993).

283. Oesterhelt, F., Rief, M. & Gaub, H. E. Single molecule force spectroscopy by AFM indicates helical structure of poly(ethylene-glycol) in water. *New Journal of Physics* **1,** 6 (1999).

284. Oelmeier, S. A., Dismer, F. & Hubbuch, J. Molecular dynamics simulations on aqueous two-phase systems - Single PEG-molecules in solution. *BMC biophysics* **5,** 14 (2012).

285. Gotte, L., Mammi, M. & Pezzin, G. in *Symposium on fibrous proteins,* edited by W. G. Crewther (Butterworth, Australia, 1968), pp. 236–245.

286. Ghoorchian, A. *et al.* Size and shape characterization of thermoreversible micelles of three-armed star elastin-like polypeptides. *The journal of physical chemistry. B* **117,** 8865–8874 (2013).

287. Michel, N., Fabiano, A.-S., Polidori, A., Jack, R. & Pucci, B. Determination of phase transition temperatures of lipids by light scattering. *Chemistry and physics of lipids* **139,** 11–19 (2006).

288. García-Arévalo, C. *et al.* Immunomodulatory Nanoparticles from Elastin-Like Recombinamers. Single-Molecules for Tuberculosis Vaccine Development. *Mol. Pharmaceutics* **10,** 586–597 (2013).

289. Ayres, L., Koch, K., Adams, P. Hans H. M. & van Hest, Jan C. M. Stimulus Responsive Behavior of Elastin-Based Side Chain Polymers. *Macromolecules* **38,** 1699–1704 (2005).

290. Cirulis, J. T. & Keeley, F. W. Kinetics and Morphology of Self-Assembly of an Elastin-like Polypeptide Based on the Alternating Domain Arrangement of Human Tropoelastin. *Biochemistry* **49,** 5726–5733 (2010).

291. van Wachem, P. B. *et al.* Biocompatibility and tissue regenerating capacity of crosslinked dermal sheep collagen. *Journal of biomedical materials research* **28,** 353–363 (1994).

292. Smyth, D. G., Nagamatsu, A. & Fruton, J. S. Some Reactions of N-Ethylmaleimide. *Journal of the American Chemical Society* **82,** 4600–4604 (1960).

293. Brewer, C. F. & Riehm, J. P. Evidence for possible nonspecific reactions between N-ethylmaleimide and proteins. *Analytical Biochemistry* **18,** 248–255 (1967).

294. Heitz, J. R., Anderson, C. D. & Anderson, B. M. Inactivation of yeast alcohol dehydrogenase by N-alkylmaleimides. *Archives of Biochemistry and Biophysics* **127,** 627–636 (1968).

295. Gregory, J. D. The Stability of N-Ethylmaleimide and its Reaction with Sulfhydryl Groups. *Journal of the American Chemical Society* **77,** 3922–3923 (1955).

296. Matsui, S. & Aida, H. Hydrolysis of some N-alkylmaleimides. *J. Chem. Soc., Perkin Trans. 2,* 1277 (1978).

297. Fontaine, S. D., Reid, R., Robinson, L., Ashley, G. W. & Santi, D. V. Long-term stabilization of maleimide-thiol conjugates. *Bioconjugate chemistry* **26,** 145–152 (2015).

298. Shen, B.-Q. *et al.* Conjugation site modulates the in vivo stability and therapeutic activity of antibody-drug conjugates. *Nature biotechnology* **30,** 184–189 (2012).

299. Tumey, L. N. *et al.* Mild method for succinimide hydrolysis on ADCs: impact on ADC potency, stability, exposure, and efficacy. *Bioconjugate chemistry* **25,** 1871–1880 (2014).

300. Lyon, R. P. *et al.* Self-hydrolyzing maleimides improve the stability and pharmacological properties of antibody-drug conjugates. *Nature biotechnology* **32,** 1059–1062 (2014).

301. Alley, S. C. *et al.* Contribution of linker stability to the activities of anticancer immunoconjugates. *Bioconjugate chemistry* **19,** 759–765 (2008).

302. Lee, J., Macosko, C. W. & Urry, D. W. Swelling Behavior of γ-Irradiation Cross-Linked Elastomeric Polypentapeptide-Based Hydrogels. *Macromolecules* **34,** 4114–4123 (2001).

303. Lee, J., Macosko, C. W. & Urry, D. W. Elastomeric Polypentapeptides Cross-Linked into Matrixes and Fibers. *Biomacromolecules* **2,** 170–179 (2001).

304. Mechler, á. *et al.* Anomalies in nanostructure size measurements by AFM. *Physical Review B* **72,** 125407 (2005).

305. Carlo, S. de & Harris, J. R. Negative staining and cryo-negative staining of macromolecules and viruses for TEM. *Micron* **42,** 117–131 (2011).

306. Partridge, S. M. in *Chemistry and Molecular Biology of the Intercellular Matrix,* edited by E. A. Balazs (Academic Press, London, New York, 1970), pp. 593–616.

307. Osborne, J. L., Farmer, R. & Woodhouse, K. A. Self-assembled elastin-like polypeptide particles. *Acta Biomaterialia* **4,** 49–57 (2008).

308. Arakawa, T. & Timasheff, S. N. Mechanism of poly(ethylene glycol) interaction with proteins. *Biochemistry* **24,** 6756–6762 (1985).

309. Ingham, K. C. Polyethylene glycol in aqueous solution. Solvent perturbation and gel filtration studies. *Archives of Biochemistry and Biophysics* **184,** 59–68 (1977).

310. Scherer, J. R. The partial molar volume of water in biological membranes. *Proceedings of the National Academy of Sciences of the United States of America* **84,** 7938–7942 (1987).

311. Rief, M., Oesterhelt, F., Heymann, B. & Gaub, H. E. Single Molecule Force Spectroscopy on Polysaccharides by Atomic Force Microscopy. *Science* **275,** 1295–1297 (1997).

312. Hoffman, A. S. Applications of thermally reversible polymers and hydrogels in therapeutics and diagnostics. *Journal of Controlled Release* **6,** 297–305 (1987).

313. Nucci, M. L., Shorr, R. & Abuchowski, A. The therapeutic value of poly(ethylene glycol)-modified proteins. *Advanced Drug Delivery Reviews* **6,** 133–151 (1991).

314. Bromberg, L. E. & Ron, E. S. Temperature-responsive gels and thermogelling polymer matrices for protein and peptide delivery. *Advanced Drug Delivery Reviews* **31,** 197–221 (1998).

315. Palasis, M. & Gehrke, S. H. Permeability of responsive poly (N-isopropylacrylamide) gel to solutes. *Journal of Controlled Release* **18,** 1–11 (1992).

316. Engel, J. & Kammerer, R. A. What are oligomerization domains good for? *Matrix Biology* **19,** 283–288 (2000).

317. Torchilin, V. P. Structure and design of polymeric surfactant-based drug delivery systems. *Journal of Controlled Release* **73,** 137–172 (2001).

318. Magin, R. L. & Niesman, M. R. Temperature-dependent permeability of large unilamellar liposomes. *Chemistry and physics of lipids* **34,** 245–256 (1984).

319. Yatvin, M. B., Weinstein, J. N., Dennis, W. H. & Blumenthal, R. Design of liposomes for enhanced local release of drugs by hyperthermia. *Science* **202,** 1290–1293 (1978).

320. Anyarambhatla, G. R. & Needham, D. Enhancement of the Phase Transition Permeability of DPPC Liposomes by Incorporation of MPPC: A New Temperature-

Sensitive Liposome for use with Mild Hyperthermia. *Journal of Liposome Research* **9,** 491–506 (1999).

321. Kong, G. *et al.* Efficacy of Liposomes and Hyperthermia in a Human Tumor Xenograft Model: Importance of Triggered Drug Release. *Cancer Research* **60,** 6950–6957 (2000).

322. Ponce, A. M., Vujaskovic, Z., Yuan, F., Needham, D. & Dewhirst, M. W. Hyperthermia mediated liposomal drug delivery. *International journal of hyperthermia* **22,** 205–213 (2006).

323. Roberts, M. J., Bentley, M. D. & Harris, J. M. Chemistry for peptide and protein PEGylation. *Advanced Drug Delivery Reviews* **54,** 459–476 (2002).

324. Banerjee, S. S., Aher, N., Patil, R. & Khandare, J. Poly(ethylene glycol)-Prodrug Conjugates: Concept, Design, and Applications. *Journal of drug delivery* **2012,** 103973 (2012).

325. Knop, K., Hoogenboom, R., Fischer, D. & Schubert, U. S. Poly(ethylene glycol) in drug delivery: pros and cons as well as potential alternatives. *Angewandte Chemie (International ed. in English)* **49,** 6288–6308 (2010).

326. Zalipsky, S. Functionalized Poly(ethylene glycol) for Preparation of Biologically Relevant Conjugates. *Bioconjugate Chem.* **6,** 150–165 (1995).

327. Alcantar, N. A., Aydil, E. S. & Israelachvili, J. N. Polyethylene glycol-coated biocompatible surfaces. *Journal of biomedical materials research* **51,** 343–351 (2000).

328. Klibanov, A. L., Maruyama, K., Torchilin, V. P. & Huang, L. Amphipathic polyethyleneglycols effectively prolong the circulation time of liposomes. *FEBS Letters* **268,** 235–237 (1990).

329. Blume, G. *et al.* Specific targeting with poly(ethylene glycol)-modified liposomes: Coupling of homing devices to the ends of the polymeric chains combines effective target binding with long circulation times. *Biochimica et Biophysica Acta (BBA) - Biomembranes* **1149,** 180–184 (1993).

330. Robertson, K. L., Soto, C. M., Archer, M. J., Odoemene, O. & Liu, J. L. Engineered T4 Viral Nanoparticles for Cellular Imaging and Flow Cytometry. *Bioconjugate chemistry* **22,** 595–604 (2011).

331. Archer, M. J. & Liu, J. L. Bacteriophage T4 Nanoparticles as Materials in Sensor Applications. Variables That Influence Their Organization and Assembly on Surfaces. *Sensors* **9,** 6298–6311 (2009).

332. Daamen, W. F. *et al.* "Lyophilisomes": A New Type of (Bio)capsule. *Advanced Materials* **19,** 673–677 (2007).

333. Kong, G., Braun, R. D. & Dewhirst, M. W. Hyperthermia Enables Tumor-specific Nanoparticle Delivery: Effect of Particle Size. *Cancer Research* **60,** 4440–4445 (2000).

334. Manzoor, A. A. *et al.* Overcoming Limitations in Nanoparticle Drug Delivery: Triggered, Intravascular Release to Improve Drug Penetration into Tumors. *Cancer Research* **72,** 5566–5575 (2012).

335. Harris, E. D. & McCroskery, P. A. The Influence of Temperature and Fibril Stability on Degradation of Cartilage Collagen by Rheumatoid Synovial Collagenase. *The New England journal of medicine* **290,** 1–6 (1974).

336. Abdel-Sayed, P., Moghadam, M. N., Salomir, R., Tchernin, D. & Pioletti, D. P. Intrinsic viscoelasticity increases temperature in knee cartilage under physiological loading. *Journal of the Mechanical Behavior of Biomedical Materials* **30,** 123–130 (2014).

337. Betre, H., Setton, L. A., Meyer, D. E. & Chilkoti, A. Characterization of a Genetically Engineered Elastin-like Polypeptide for Cartilaginous Tissue Repair. *Biomacromolecules* **3,** 910–916 (2002).

338. Betre, H. *et al.* Chondrocytic differentiation of human adipose-derived adult stem cells in elastin-like polypeptide. *Biomaterials* **27,** 91–99 (2006).

339. McHale, M. K., Setton, L. A. & Chilkoti, A. Synthesis and in Vitro Evaluation of Enzymatically Cross-Linked Elastin-Like Polypeptide Gels for Cartilaginous Tissue Repair. *Tissue Engineering* **11,** 1768–1779 (2005).

340. Betre, H. *et al.* A thermally responsive biopolymer for intra-articular drug delivery. *Journal of Controlled Release* **115,** 175–182 (2006).

341. Rothenfluh, D. A., Bermudez, H., O'Neil, C. P. & Hubbell, J. A. Biofunctional polymer nanoparticles for intra-articular targeting and retention in cartilage. *Nature materials* **7,** 248–254 (2008).

342. Whitmire, R. E. *et al.* Self-assembling nanoparticles for intra-articular delivery of anti-inflammatory proteins. *Biomaterials* **33,** 7665–7675 (2012).

343. Bartlett II, R. L., Sharma, S. & Panitch, A. Cell-penetrating peptides released from thermosensitive nanoparticles suppress proinflammatory cytokine response by specifically targeting inflamed cartilage explants. *Nanomedicine* **9,** 419–427 (2013).

344. Moghadam, M. N., Kolesov, V., Vogel, A., Klok, H.-A. & Pioletti, D. P. Controlled release from a mechanically-stimulated thermosensitive self-heating composite hydrogel. *Biomaterials* **35,** 450–455 (2014).

345. Chilkoti, A., Christensen, T. & Mackay, J. A. Stimulus responsive elastin biopolymers: Applications in medicine and biotechnology. *Current Opinion in Chemical Biology* **10,** 652–657 (2006).

346. Elsaid, K. A. *et al.* Pharmaceutical nanocarrier association with chondrocytes and cartilage explants: Influence of surface modification and extracellular matrix depletion. *Osteoarthritis and Cartilage* **21,** 377–384 (2013).

347. van den Hoven, Jolanda M. *et al.* Liposomal Drug Formulations in the Treatment of Rheumatoid Arthritis. *Molecular pharmaceutics* **8,** 1002–1015 (2011).

348. Hayes, K. W. Heat and cold in the management of rheumatoid arthritis. *Arthritis & Rheumatology* **6,** 156–166 (1993).

349. Jee, W. S. S. in *Histology: Cell and tissue biology,* edited by L. Weiss (The MacMillan Press, New York, 1983), Vol. 5, pp. 200–255.

350. Bajpayee, A. G., Wong, C. R., Bawendi, M. G., Frank, E. H. & Grodzinsky, A. J. Avidin as a model for charge driven transport into cartilage and drug delivery for treating early stage post-traumatic osteoarthritis. *Biomaterials* **35,** 538–549 (2014).

Danksagung

Als Erstes möchte ich meinem Doktorvater Prof. Dr. Thorsten Hugel danken, der mir die Arbeit zu diesem Thema in seiner Arbeitsgruppe ermöglichte. Ich danke hierbei für die hilfreichen wissenschaftlichen Diskussionen, in denen neue Ideen entwickelt werden konnten und gleichzeitig für den wissenschaftlichen Freiraum, in dem ich neue Ideen umsetzen konnte. Ich danke ebenfalls meiner Zweitgutachterin Frau Prof. Dr. Christine Papadakis. Außerdem danke ich der Graduiertenschule IGSSE „International Graduate School of Science and Engineering" für die Unterstützung.

Als nächstes möchte ich Dr. Tobias Pirzer danken, der mir das Forschungsgebiet zu ELPs vorstellte und mir deren spezielle Eigenschaften lehrte. Ein weiterer Dank gilt unserem Kooperationspartner Prof. Dr. Nolan B. Holland an der Cleveland State University (Ohio) für die gute Zusammenarbeit und im Speziellen für hilfreiche Diskussionen bezüglich theoretischer Betrachtungen der Partikel. Ich danke Ali Ghoorchian, Ph.D. und James T. Cole, Ph.D. für kompetenten Rat bei Fragen rund um die Eigenschaften von ELPs und die große Hilfe bei der Herstellung der ELPs.

Ferner danke ich Prof. Dr. Leif Schröder am Leibniz-Institut für molekulare Pharmakologie (FMP) Berlin für die Ermöglichung erster NMR-Untersuchungen der Partikellösungen. Hierbei möchte ich auch Dr. Franz Schilling danken für die engagierte Mitarbeit und Dr. Matthias Schnurr für die Durchführung einiger Messungen. Ich möchte mich bei Prof. Dr. Erkki Ruoslahti für die Ermöglichung des dreimonatigen Forschungsaufenthaltes in seinem Labor bedanken. Ein weiterer Dank gilt hierbei Gary Braun, Ph.D. für die gute Zusammenarbeit.

Ferner danke ich Dr. Stefanie Krysiak für die Einzelpolymermessungen mit ELPs und Joanna Urban für die Mitarbeit an den Knorpelmessungen. Ich danke Dr. Björn Hellenkamp für die FCS-Messungen und Dr. Christoph Kaiser für die TEM-Messungen der Partikellösungen. Katrin Böttcher danke ich für die Hilfe bei der statistischen Analyse. Für die Unterstützung bei der Erstellung der 3D-Graphikdesigns danke ich Dr. Harry Braun und Dr. Sandra Kienle. Ich danke allen meinen Bürokollegen Dr. Tobias Pirzer, Dr. Sandra Kienle, Dr. Stefanie Krysiak, Dr. Frank Stetter, Dr. Bizan Balzer und Joanna Urban für die angenehme Arbeitsatmosphäre.

Mein großer Dank gilt meinen Eltern, die mir diesen Weg ermöglichten und mich immer unterstützen. Ich danke ebenfalls meinen Geschwistern Julia und Holger, sowie meinen Freunden für all die guten Erlebnisse. Mein letzter ganz besonderer Dank gilt meinem Freund Boris.